KAUNAS UNIVERSITY OF TECHNOLOGY

AUŠRINĖ JURKEVIČIŪTĖ

LASER PATTERNING OF NANOCOMPOSITE DIAMOND-LIKE CARBON THIN FILMS WITH METAL NANOPARTICLES AND INVESTIGATION OF THEIR OPTICAL AND STRUCTURAL PROPERTIES

Doctoral dissertation
Technological Sciences, Materials Engineering (T 008)

2020, Kaunas

This doctoral dissertation was prepared at Kaunas University of Technology, Institute of Materials Science during the period of 2015-2019. The studies were supported by Research Council of Lithuania and European Social Fund.

Scientific Supervisor:

Prof. Dr. Tomas TAMULEVIČIUS (Kaunas University of Technology, Technological Sciences, Materials Engineering – T 008)

Doctoral dissertation has been published in:
https://ktu.edu

Editor:

Armandas Rumšas (Publishing Office "Technologija")

KAUNO TECHNOLOGIJOS UNIVERSITETAS

AUŠRINĖ JURKEVIČIŪTĖ

NANOKOMPOZITINIŲ DEIMANTO TIPO ANGLIES PLONŲ DANGŲ SU METALO NANODALELĖMIS LAZERINIS STRUKTŪRIZAVIMAS IR JŲ OPTINIŲ BEI STRUKTŪRINIŲ SAVYBIŲ TYRIMAS

Daktaro disertacija
Technologijos mokslai, Medžiagų inžinerija (T 008)

2020, Kaunas

Disertacija rengta 2015-2019 metais Kauno technologijos universiteto Medžiagų mokslo institute. Mokslinius tyrimus rėmė Lietuvos mokslo taryba ir Europos socialinis fondas.

Mokslinis vadovas:

Prof. Dr. Tomas TAMULEVIČIUS (Kauno technologijos universitetas, technologijos mokslai, medžiagų inžinerija – T 008)

Interneto svetainės, kurioje skelbiama disertacija, adresas:
https://ktu.edu

Redagavo:

Armandas Rumšas (leidykla „Technologija“)

SANTRAUKA

Metalų (pavyzdžiui, vario ir sidabro) nanodalelės, pasižyminčios plazmoninėmis savybėmis, pritraukia daug dėmesio dėl pritaikymo optiniuose (pavyzdžiui, lūžio rodiklio) jutikliuose. Nanodalelių optinis atsakas priklauso nuo jų dydžio ir formos. Aplinka taip pat turi įtakos dalelėms: ore esantys elementai gali reaguoti su metalais ir pakeisti jų savybes. Todėl būtina daleles apsaugoti nuo nepageidaujamo aplinkos poveikio, bet tuo pačiu išlaikyti jų pageidautinas plazmonines savybes. Tam nanodalelės gali būti įterpiamos į kitos medžiagos matricą. Papildomai optinės savybės gali būti keičiamos ir jutiklių jautrumas padidinamas medžiagoje suformuojant periodines struktūras.

Šioje disertacijoje pateikiamas vario ir sidabro nanodalelių ir deimanto tipo anglies matricos nanokompozitų sisteminis tyrimas. Skirtingų metalo koncentracijų nanokompozitai buvo nusodinti nesubalansuoto reaktyviojo magnetroninio dulkinimo metodu. Pralaidumo elektronų mikroskopu buvo ištirtas dangų sluoksniavimasis. Skenuojantis elektronų ir helio jonų mikroskopai buvo naudojami nustatyti nanodalelių dydžius nanokompozituose. Ramano spektroskopija buvo panaudota tiriant deimanto tipo anglies matricos savybes ir paviršiuje stiprinamos Ramano sklaidos efektą. Rentgeno spindulių atspindžio metodu buvo nustatytas dangų tankis. Spektroskopinės elipsometrijos metodu buvo nustatytos dangų optinės savybės. Tiek Rentgeno spindulių atspindžio, tiek spektroskopinės elipsometrijos modeliai, naudojami teorinių kreivių sutapdinimui su eksperimentinėmis, atskleidžia sluoksniuotą nanokompozitinių dangų struktūrą.

Ištyrus nanokompozitines dangas, deimanto tipo anglyje su sidabro nanodalelėmis dangose buvo suformuotos vienmatės periodinės struktūros. Lazerinio interferencinio struktūrizavimo galimybės buvo išbandytos modeliuojant ir realizuojant struktūras nuolatinės veikos lazeriu holografinės litografijos metodu fotorezisto sluoksnyje. Struktūra nanokompozite buvo suformuota femtosekundiniu lazeriu tiesioginio lazerinio interferencinio struktūrizavimo metodu. Nanokompozitams su sidabro nanodalelėmis buvo nustatytas struktūrizavimo slenkstis (mažiausias reikalingas lazerio įtėkis struktūrai suformuoti), kuris buvo palygintas su atskirų deimanto tipo anglies ir sidabro dangų struktūrizavimo slenksčiais. Pritaikant dvimates greitąsias Furjė transformacijas skenuojančio elektronų ir helio jonų mikroskopų mikrofotografijoms buvo gauti suformuotų struktūrų difrakcijos vaizdai.

Buvo ištirta nanodalelių dydžių matricoje keitimo galimybė daleles apšviečiant lazeriu. Kai nanokompozito nanodalelės pasižymi bimodaliniu (turi du vyraujančius skersmenis) skirstiniu, jį galima pakeisti į unimodalinį prie tam tikrų lazerinės apšvitos parametrų. Femtosekundinio lazerio poveikis deimanto tipo angliai su sidabro nanodalelėmis buvo vizualizuojamas spektroskopinės elipsometrijos žemėlapiu, kuris buvo palygintas su optinio mikroskopo mikrofotografija. Skirtumai tarp lazeriu paveiktų ir nepaveiktų zonų nanokompozituose buvo matomi ir tamsaus lauko mikroskopijos, ir dvifotonės liuminescencijos metodais.

TABLE OF CONTENTS

LIST OF FIGURES

LIST OF TABLES

ABBREVIATIONS AND SYMBOLS

1D, 2D	–	one-, two-dimensional
A	–	absorbance; area
a	–	ablation rate
α	–	absorption coefficient
B	–	magnetic field
C	–	concentration; ellipsometric parameter
C_i	–	centre of i^{th} particle
CCD	–	charge-coupled device
Δ	–	ellipsometric parameter
D	–	diameter of laser affected spot
d	–	thickness
DL	–	detection limit of the sensor
DLC	–	diamond-like carbon
DLC:Ag	–	diamond-like carbon matrix with embedded silver nanoparticles
DLC:Cu	–	diamond-like carbon matrix with embedded copper nanoparticles
DLIP	–	direct laser interference patterning
DOE	–	diffractive optical element
ε_1	–	real part of dielectric permittivity
ε_2	–	imaginary part of dielectric permittivity
E	–	electric field
$\tilde{E}(r)$	–	resonance mode
EDS	–	energy dispersive X-ray spectroscopy
EF	–	enhancement factor
EMA	–	effective medium approximation
Φ	–	fluence
φ	–	phase
Φ_{th}	–	threshold fluence
FFT	–	fast Fourier transform
FOM	–	figure of merit
fs-laser	–	femtosecond laser
FWHM	–	full width at half maximum
HIM	–	helium ion microscopy
HL	–	holographic lithography
I	–	intensity

k – extinction coefficient
Λ – pitch of periodic structure
λ – wavelength
$L(\omega)$ – frequency dependant local field factor
LIPSS – laser induced periodic surface structures
LSPR – localized surface plasmon resonance
μ – mean of lognormal distribution
N – number of pulses; ellipsometric parameter
n – refractive index
NIR – near infrared
ω – logarithm of standard deviation; frequency
Ψ – ellipsometric parameter
Q – quality factor
ρ – density; the ratio of Fresnel reflection coefficients
R – reflectance
R^2 – determination coefficient
R_{res} – sensor resolution
RMSE – root mean square error
σ – standard deviation of lognormal distribution
S – ellipsometric parameter
S_λ – sensitivity
SE – secondary electrons; spectroscopic ellipsometry
SEM – scanning electron microscopy
SERS – surface enhanced Raman scattering
SPP – surface plasmon polariton
T – transmittance
θ – angle of incidence
TEM – transmission electron microscopy
TPA – transpolyacetylene
TPL – two-photon luminescence
UV – ultraviolet
Vis – visible
W – width of laser irradiated line
w – laser spot size on sample surface
x_c – centre coordinate of lognormal distribution
x_i, x_j – centres of i^{th} and j^{th} laser irradiated lines
XRR – X-ray reflectivity
y_0 – offset of the fitting function

1. INTRODUCTION

The recent developments in nanotechnology established the necessity of the methods for the manipulation of light at the nanometre scale. At such a scale, devices based on the traditional (geometric) optics reach the fundamental diffraction limit and no longer work, thus a new generation of optical devices must be developed. The miniaturisation trend in photonics not only reduces the size of devices but also provides possibility to obtain improved functionality compared to bulk optical elements.

Metal nanoparticles have been attracting a lot of attention due to the plasmonic effects, especially because of localized surface plasmon resonance (LSPR). Gold is a traditional choice in plasmonics, however, other metals, such as silver, copper, aluminium, palladium, platinum, nickel, tin, yttrium, etc., are also being heavily investigated. LSPR of metal nanoparticles is highly sensitive to the medium where they are situated. When a metal is chemically active and thus susceptible to the environment, experiments are directed towards finding a passivating material which would not suppress the desired properties of the metal. These are the driving forces for the intense research in the field of plasmonic (nano)composites.

Most commonly, metal nanoparticles are embedded in polymer or glass matrices. An alternative is amorphous (diamond-like) carbon which in itself is denoted by a number of advantages and applications. It shares some of the properties with diamond and can prevent metal from oxidation while still maintaining the plasmonic properties.

The structure of nanocomposites is mostly limited by deposition processes. However, it is possible to alter the structure of the deposited film by post processing of ultrashort pulse laser irradiation. Advanced patterning methods, such as holographic lithography and direct laser interference patterning, are capable to create one-, two-, and even three-dimensional periodic structures in the film or in the bulk of nearly any material. Ultrashort pulse irradiation can melt and change the structure of the material and the linear dimensions of nanoparticles. However, laser parameters have to be chosen for the specific materials because the material is affected only when the laser parameters are at or above the characteristic threshold value. In order to investigate the morphology of the imposed periodic structures, scanning electron microscopy might not be good enough due to the charging effects. In such cases, it is preferable to use other types of advanced microscopy techniques, e.g., helium ion microscopy. Periodic structures of sub-micrometre critical dimensions have many possible applications: from optical diffractive elements and fluid dynamics devices to optical sensors and plasmonic crystals.

Optical applications rely on the optical properties of the materials. In the case of nanocomposites, at least two phases are present with their own optical properties. Therefore, nanocomposite optical properties depend on the metal content in the matrix and the size and shape of the nanoparticles, etc. In order to determine the optical properties of a plasmonic nanocomposite, advanced optical measurement techniques are required. Spectroscopic ellipsometry is an elaborate optical measurement method primarily used for the determination of thicknesses and optical

constants of thin films. It can also be employed to resolve volume fractions of materials in the compound, which is very important for understanding the optical properties of metal nanocomposites.

Research objective

To investigate the optical properties of various metal filler amorphous diamond-like carbon matrix nanocomposites deposited under different conditions and to explore their micro- and nanopatterning possibilities by employing advanced laser techniques.

Research tasks

1) To select the deposition conditions and synthesize various copper and silver fractions containing amorphous diamond-like carbon nanocomposite films which would preserve the plasmonic properties of the metals;
2) To investigate the elemental and structural composition of the films as well as the optical properties, metal volume fractions, nanoparticle size distributions and film thicknesses by employing advanced analytical methods;
3) To establish laser beam interference based patterning methods and fabricate one- and two-dimensional sub-micrometre pitch patterns in nanocomposite films;
4) To determine the laser patterning threshold of nanocomposite films and compare it to the threshold of nanocomposite constituents;
5) To explore the feasibility and limits of the nanoparticle size distribution modification via ultrashort pulse laser irradiation.

Scientific novelty

1) Ultrashort pulse laser patterning threshold for diamond-like carbon nanocomposite films with embedded silver nanoparticles has been determined for the direct laser interference patterning method;
2) Copper and silver fractions as well as dielectric functions of nanocomposite films have been determined via spectroscopic ellipsometry, and the main findings have been compared with the results of alternative analytical methods;
3) The dependence of the silver nanoparticle size distribution in amorphous diamond-like carbon nanocomposite films on the irradiation parameters of ultrashort pulse laser irradiation has been determined.

Key statements of the doctoral dissertation

1) Combination of transmission electron microscopy, energy dispersive X-ray spectroscopy, X-ray reflectivity, and spectroscopic ellipsometry reveal the multilayered nature of nanocomposite films and yield information about the properties of each layer;
2) Interference-based two-beam laser patterning techniques (holographic lithography and direct laser interference patterning) are capable to produce

one- and two-dimensional periodic patterns of various geometries and symmetries in materials covering large areas. Fourier transformations of the corresponding images of laser affected areas give primal information about the structure;

3) Due to the localized surface plasmon resonance of the filler, the patterning of nanocomposites requires lower energy density than the patterning of its components separately;
4) The diameters of metal nanoparticles in the nanocomposites can be altered by changing either the laser fluence or the number of applied pulses. The bimodal size distribution of nanoparticles can be changed into unimodal distribution by applying laser irradiation at a specific energy density.

Dissertation structure

The dissertation consists of 5 main chapters: Introduction, Literature Review, Work Methodology, Results and Discussion, and Conclusions. It also contains a list of references, acknowledgements, the curriculum vitae of the author, and lists of publications and abstracts of the attended conferences. The volume of the dissertation is 136 pages. It features 71 figures, 12 tables, 54 numbered equations, and 201 references.

Contribution of the dissertation author

The work presented in the dissertation was carried out at the Institute of Materials Science of Kaunas University of Technology and during ERASMUS+ internship at Mads Clausen Institute of University of Southern Denmark as part of the European Doctorate programme "Physics and Chemistry of Advanced Materials" (PCAM).

The author planned all the experiments (requirements for deposition of nanocomposite films and periodic patterns in them) and performed holographic lithography, morphological (scanning electron and optical microscopies of periodic patterns), spectroscopic (Raman scattering, UV-Vis-NIR), and ellipsometric (regular and mapping) measurements of the samples as well as the analysis of the obtained data (measurement of the pitches of periodic patterns and the widths of the laser affected lines, nanoparticle size distributions, threshold determination, fitting of the data, ellipsometry modelling). Holographic lithography was performed by the author together with MSc student Nerijus Armakavičius and PhD student Dainius Virganavičius. N. Armakavičius also wrote software to calculate interference patterns. According to the provided experiment plan and under the request of the author, the deposition of nanocomposites was performed by dr. Andrius Vasiliauskas, direct laser interference patterning was performed by BSc student Linas Šimatonis and PhD student Mindaugas Juodėnas. X-ray reflectivity measurements and their analysis was performed by dr. Algirdas Lazauskas. Helium ion microscopy imaging and two-photon luminescence was performed by Vadzim Adashkevich and PhD student Paweł Piotr Cielecki from Mads Clausen Institute, with the author being present. Transmission electron microscopy was performed by dr. Algirdas Selskis and dr. Martynas Skapas from the Center for Physical Sciences

and Technology and also by dr. Arno Meingast from *NanoPort Europe* in collaboration with JSC *Vildoma*. Some of the nanoparticles in micrographs and ellipsometric analysis was carried out by BSc students Gerda Klimaitė, Alvita Žabaitė and Justas Deveikis during the mentoring process.

The scientific results presented in the dissertation have been published in 4 research papers in journals indexed in *Clarivate Analytics Web of Science* with the impact factor and delivered in 16 conference presentations, 11 of which have been presented by the dissertation author herself. The full list of publications and conference abstracts is given at the end of the dissertation. About half of the two initial publications related to the dissertation and all of the last one have been prepared by the author of the dissertation. The co-authors contributed with the experiments and analysis, writing of the paper, ideas, and consultations. In the third publication, the dissertation author did microscopy imaging and analysis, the remaining work was done by the co-authors. If the data presented in Results and Discussion chapter has been published in a paper or presented at the conference, it is indicated by [A] or [B], respectively, followed by the number which coincides with the number in The List of Publications and Conferences Related to the Dissertation.

2. LITERATURE REVIEW

2.1. Plasmonic materials

The field of plasmonics merges optics and nanoelectronics by confining the light down to the nanometre scale. Plasmonic materials feature negative real dielectric permittivity and plenty of free electrons which create oscillations with the applied electromagnetic field [1].

Gold is arguably the most popular plasmonic material due to its high stability and strong plasmonic response in the visible light range [2]. However, the absorption coefficient of gold is relatively high, which is undesirable for certain applications [3]. Many other materials have been investigated for their plasmonic properties in order to find an alternative to gold: silver [4], palladium [5], niobium [6], copper, platinum, nickel, tin, yttrium, aluminium [2], cobalt, chromium, iron, molybdenum, manganese, rhodium, tantalum, titanium, titanium and zirconium nitrides, tungsten [7], indium tin and aluminium-doped zinc oxides [8], etc. In theory, spherical palladium nanoparticles are more LSPR sensitive than gold, but their fabrication is fairly problematic [5]. Magnesium can cover the entire visible range by changing the diameter of nanodisks and can be applied for hydrogen storage [9]. By depositing a single graphene layer on gold, it is possible to enhance the electric field more than 4 times. However, multilayered graphene does not provide any enhancement [10].

At the interface of the metal film and the dielectric material, a freely propagating surface charge density wave can be induced. This phenomenon is called *surface plasmon polaritons* (SPP, Fig. 2.1a), or *surface plasmon resonance*, and it generates an evanescent field. However, SPPs cannot be excited directly, but rather with a help of a prism coupler, diffraction grating, or a waveguide [11].

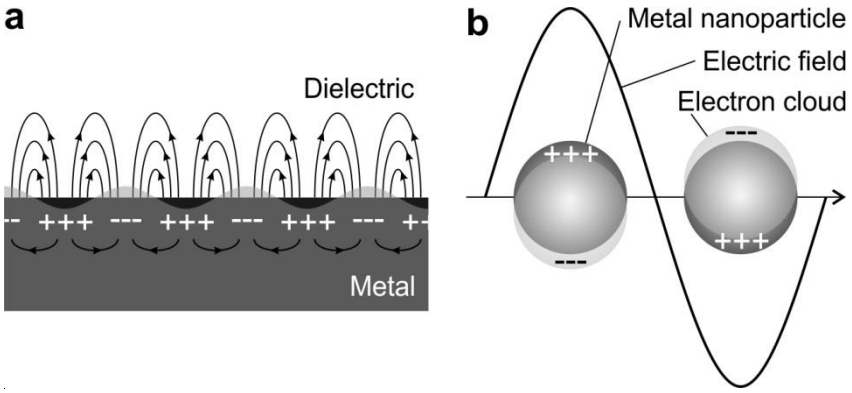

Fig. 2.1. Schematic illustrations of the surface plasmon polariton at the interface of a metal and a dielectric (a) and a localized surface plasmon in a metal nanoparticle with the applied electric field (b). Adapted from [11, 12].

Metal nanoparticles have attracted a lot of attention due to the localized surface plasmon resonance (LSPR) effect [2]. LSPR is resonant collective oscillations of electrons in a nanoparticle (Fig. 2.1b), which is excited by irradiating

metal nanoparticles with light. At the resonance wavelength, strong absorption or scattering of light from metal nanoparticles is observed. At the surface of a nanoparticle, the electric charge is separated, and a strongly enhanced electric field is generated. Contrary to SPP, LSPR can be excited directly [11]. LSPR depends on the particle size and occurs only when the size of the nanoparticle is lower than the wavelength of the incident light [13].

LSPR can create the photo-thermal effect (conversion of light energy into heat) through optical excitation and non-radiative relaxation [14]. The stability of plasmonic materials is a very important subject due to their applications in various environments [15]: the photo-thermal effect of plasmonic materials is applied in cancer therapy, optofluidic control, nano-welding, optical data storage, imaging, sensing, etc. [14].

Optical processes can be significantly enhanced by strong electromagnetic fields resulting from the coupling of light with surface plasmons. Field enhancement in the surroundings of metal nanostructures is described as the frequency-dependent local-field factor [16]:

$$L(\omega) = \frac{\left|\vec{E}_l(\omega)\right|}{\left|\vec{E}_0(\omega)\right|}, \tag{2.1}$$

where ω is the frequency of the electric field (Hz), E_l is the local electric field associated with plasmonic excitations (V/m), E_0 is the incident electric field (V/m). The local-field factor for surface enhanced Raman scattering can be as high as 100 [16]. When the material is placed in a system, its performance is described by the quality factor [1]:

$$Q = \frac{(Enhanced\ local\ field)}{(Incident\ field)}. \tag{2.2}$$

LSPR highly depends on the shape of nanoparticles and so does the quality factor. For spherical and spheroid particles, the quality factors are, respectively [1]:

$$Q(\omega) = \frac{-\varepsilon_1(\omega)}{\varepsilon_2(\omega)}, \tag{2.3}$$

$$Q(\omega) = \frac{\varepsilon_1(\omega)^2}{\varepsilon_2(\omega)}, \tag{2.4}$$

where ε_1 and ε_2 are the real and imaginary parts of dielectric permittivity, respectively. From these equations, it is clear that, for a high quality factor, the material should possess high negative ε_1 and low ε_2 [1]. Example dielectric functions of silver and copper are depicted in Fig. 2.2.

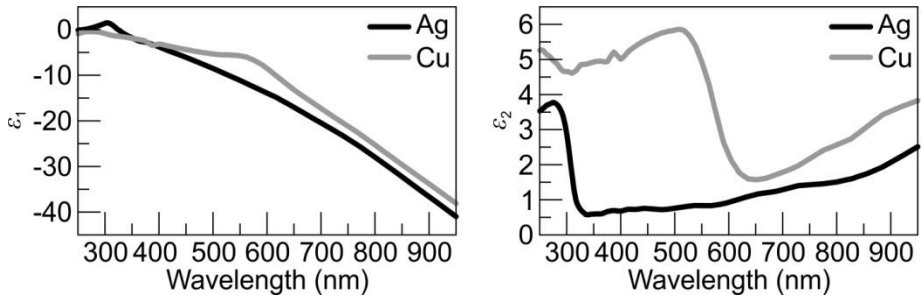

Fig. 2.2. Real (ε_1) and imaginary (ε_2) parts of the dielectric function of silver (black) and copper (grey) as available in the *Spectroscopic Ellipsometry Analyzer* software database.

Plasmonic nanostructured materials can be deposited by physical vapour deposition, liquid chemical methods, wet chemical synthesis, laser-embossing, annealing of thin films, thermal evaporation, high temperature sputtering, low temperature molecular beam epitaxy, etc. Additionally, they can be patterned by electron beam lithography, laser interference (holographic) lithography, focused ion beam milling [1, 17, 18], etc.

2.1.1. *Plasmonic nanoparticles*

Plasmonic nanoparticles have plenty of applications in materials and environmental sciences, biomedicine and other fields, including solutions for optical waveguides and switches, biosensors, cancer therapy, catalysis, seawater desalination [9, 19–23], etc.

Metal nanoparticles are widely used to enhance the Raman scattering signal by the so-called surface enhanced Raman scattering (SERS) effect: the electromagnetic field increases due to laser LSPR excitation in nanoparticles. In such a case, frequency-dependent local-field factors are expressed as [16]:

$$L(\omega_{\mathrm{L}}) = \frac{\left|\vec{E}_{\mathrm{l}}(\omega_{\mathrm{L}})\right|}{\left|\vec{E}_{0}(\omega_{\mathrm{L}})\right|}, \tag{2.5}$$

$$L(\omega_{\mathrm{S}}) = \frac{\left|\vec{E}_{\mathrm{l}}(\omega_{\mathrm{S}})\right|}{\left|\vec{E}_{0}(\omega_{\mathrm{S}})\right|}, \tag{2.6}$$

where ω_{L} and ω_{S} are laser and scattering frequencies (Hz), respectively. From here, the enhancement factor *EF* of SERS is [16]:

$$EF = L^2(\omega_{\mathrm{L}})L^2(\omega_{\mathrm{S}}) \approx \frac{\left|\vec{E}(\omega_{\mathrm{L}})\right|^4}{\left|\vec{E}_{0}(\omega_{\mathrm{S}})\right|^4}. \tag{2.7}$$

In a simplified case, when the studied concentrations and numbers of excited molecules are the same in the regular Raman and SERS, the enhancement factor can be easily calculated from the experimental spectra [24]:

$$EF = \frac{I_{\mathrm{SERS}}}{I_{\mathrm{Raman}}}, \tag{2.8}$$

where I_{SERS} and I_{Raman} are the intensities of the selected peak in the SERS and Raman scattering spectra, respectively (arbitrary units). The SERS enhancement factor of

close-packed nanoparticles could be as high as 10^{10}, which enables single molecule detection [16].

2.1.1.1. *Copper nanoparticles*

The LSPR of copper is in a similar range as in the case of gold (both close to 600 nm, depending on the size of nanoparticles) [25–27]. However, copper has advantages over gold: it is cheaper and is compatible with semiconductor technology [28]. The disadvantage of copper is its environmental instability (surface oxidation), but it could be overcome by incorporating copper nanoparticles into a matrix of other materials [29]. Copper demonstrates not only expressed plasmonic properties but is also advantageous for tribological, mechanical and antibacterial applications [30, 31]. Copper, in combination with other materials, can provide interesting properties, such as giant piezoresistivity [32] or saturable absorption [33].

2.1.1.2. *Silver nanoparticles*

There are several methods for the deposition of silver nanoparticles. Thermal evaporation can be used to deposit very thin layers (several nanometres thickness) of silver on a substrate and then annealing it in high temperature to form islands or nanoparticles [4, 17]. Silver salts can be patterned by using ultraviolet (UV) light to create clusters of silver nanoparticles by photoreduction [34]. Nanoparticles can also be produced from colloidal synthesis, but, in this case, their size distribution is very broad [35], however, monodisperse distribution is possible by the polyol method [36]. When nanoparticles are distributed in an orderly fashion, the pitch does not have a high impact on LSPR. The impact is greater with the change in the size of nanoparticles and the distance between them [37]. However, arrays of nanoparticles generate a collective plasmonic response and have distinct plasmonic surface lattice resonance which depends on the parameters of the array [38].

The main disadvantage of silver as a plasmonic material is its instability in air, i.e., silver gets oxidised or sulfurized and loses the desirable properties [4, 39]. It was reported that very pure silver nanoparticles with the perfect crystalline structure have a 5 times longer lifetime than the conventional Ag nanoparticles [40]. It is possible to increase the lifetime of silver nanoparticles as an LSPR material 8 times by synthesizing bimetal nanoparticles, e.g., silver and cobalt alloy [15]. Other solutions of instability problems require embedding nanoparticles into the matrix [41].

2.2. Nanocomposite films

Nanocomposite is a combination of at least two different materials and at least one dimension is in the nanometres order [42]. Thus metal nanoparticles can be embedded in a matrix [4] or covered with a thin film of a passivating material [3] in order to create a nanocomposite. These materials have to be chosen so that they would not weaken the plasmonic properties of nanoparticles [4]. A nanocomposite can even be useful to overcome fabrication difficulties of pure materials, such as poor adhesion of a film, surface roughness, spontaneous alloying [43, 44], etc. However, some of the ultimate advantageous properties can be gained at the expense

of other, not advantageous, properties, e.g., by increasing the copper content in amorphous carbon up to 28 at.%, Young's modulus decreases 1.5 times, nanohardness decreases 2 times, friction increases 4 times, but adhesion and fracture toughness become better, and the residual stress is lower [45]. Hence, all the constituents of the nanocomposite contribute their best properties so that to create a new material with exceptional properties which would provide new possibilities for applications of nanocomposite materials.

3.12 at.% silver nanoparticles with diameters of 23.7 nm in diamond-like carbon deposited on textile and covered with cellulose work as an antibacterial bandage and can kill 99.9% of bacteria in 320 minutes [46]. Covering medical body implants with 2 at.% silver in diamond-like carbon provides antibacterial properties, prevents post-implantation infections, while also maintaining the cell viability [47]. A composite consisting of silver and indium tin oxide covered with pyrrole and chitosan can detect cadmium, lead, and mercury ions in contaminated water [48]. A randomly distributed gold cluster in a silicon dioxide matrix can serve as a broadband anti-reflective coating for silicon reducing silicon reflectivity to 0.1% in the visible spectrum [49]. The multi-layered structure of diamond-like carbon and its nanocomposites with copper and tungsten on stainless steel substrates have a very smooth surface, high hardness of 35 GPa, and low friction of 0.14 [30]. Inserting less than 0.05 wt.% of silver in the epoxy resin and irradiating it with light allows the curing of resin (polymerisation) without the need for external heating [20].

Some nanocomposite fabrication methods are not desirable for certain applications, e.g., wet chemical synthesis in the semiconductor industry, thus alternatives should be considered. Reactive magnetron sputtering or other physical vapour deposition methods are a better approach in such cases [50]. Other possible fabrication methods involve ion implantation, chemical reduction, etc. [40]. In some cases, carbon tends to crystallise and form alloys in contact with metals (iron, copper, nickel, cobalt, platinum, palladium, etc.), which results in phase separation in nanocomposite thin films [51]. Polymer:metal nanocomposites are widespread and thoroughly investigated [52]. Another widely used matrix for nanoparticles is diamond-like carbon [53].

2.3. Diamond-like carbon

Diamond-like carbon (DLC) is a broad term used to describe hydrogenated and hydrogen-free amorphous carbon [54]. It features sp^2 and sp^3 phase bonds between carbon atoms, and their ratio determines the specific DLC type (Fig. 2.3): amorphous (a-C), amorphous hydrogenated (a-C:H), tetrahedral amorphous (ta-C), or tetrahedral hydrogenated amorphous (ta-C:H) [55]. DLC has low electron affinity, is chemically inert, highly mechanically stable and thermally conductive [56]. Its chemical inertness makes DLC a very good option as a matrix material for nanocomposites [44]. High internal stresses in DLC films are introduced due to sp^3 bonding, whereas poor adhesion to some substrates is due to the differences in thermal expansion coefficients [57]. Some of DLC disadvantages can be overcome by introducing nitrogen, boron, silicon, oxygen, fluorine or metals into thin films

[56]. For example, by introducing 2.8 at.% of titanium in DLC, the adhesion strength, electrical resistivity, and electrochemical activity of the film improve [58].

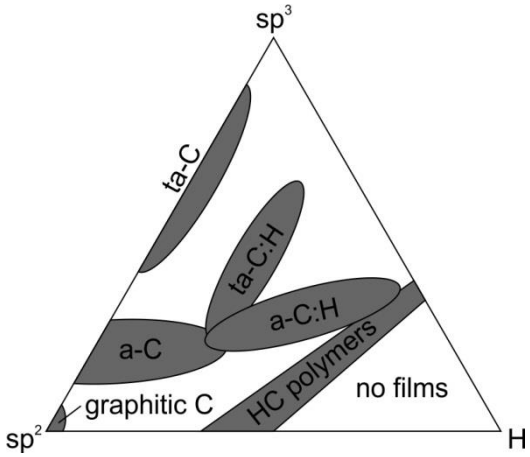

Fig. 2.3. Phase diagram of carbon containing thin films depending on sp^2, sp^3, and hydrogen content. Adapted from [59].

DLC can be deposited by various methods: chemical vapour deposition [60], ion implantation [61], magnetron sputtering [62], etc. The selected deposition process and its parameters determine the properties of DLC [61]. DLC finds applications in many different fields ranging from electronics to medicine [63].

2.4. Optical properties of nanocomposites and their application for optical sensors

The optical response of nanoparticles depends on the type of materials used for nanoparticles, their size and spatial distribution, the surroundings or the matrix [4], etc. The shape of nanoparticles also plays an important role: resonance is different for spherical, oblong, triangular, or cubic particles [64]. The LSPR peak broadens, and its position red-shifts with increased size of nanoparticles [4]. The red-shift stems from nucleation and crystal growth, which leads to an increased distance between the valence bands. The opposite is true for the blue-shift: reducing the size of nanoparticles leads to a reduced distance between the valence bands [65]. Also, when, for example, copper nanoparticles are exposed to oxygen, the LSPR peak blue-shifts due to the increased number of vacancies and the carrier density [66]. It was reported that the absorption peaks are more sensitive to the optical constants of matrix materials than to the diameter of the embedded nanoparticles [67]. Furthermore, absorption spectra can have additional peaks related to dipolar, quadrupolar or higher plasmonic modes intrinsic for cubic nanoparticles [38].

One of the possible fields of the applications of plasmonic materials is optical sensors which require very specific optical properties [3]. A sensor is a device manufactured to detect specific compounds, parameters, or changes in the environment and convert them into a readable signal [68]. Optical sensors are more favourable than electronic sensors in harsh environments because they can detect the signal without contact, and there is no probability of electrical sparks. The materials

have to be chosen depending on the desired final properties of the sensor, such as the frequency of plasmonic resonance, the catalytic activity, and the magnetic properties. The sensitivity of the sensor can be increased by fabrication of nanoparticles from the alloys of plasmonic materials, e.g., palladium and gold [2]. Another possibility is exotic geometries. An example could be aluminium, copper or silver nanorings with magnesium fluoride, aluminium or silicon oxides as dielectric materials [69].

Usually, plasmonic optical sensors require a white light source and a spectrometer in order to detect the changes in the LSPR peak. However, with careful design of materials, shapes and sizes, the optical element could work with a light emitting diode and a photodiode [2]. Thus, the fabrication of nanocomposites possessing the proper properties is a very important step in the creation of a functional sensor.

Some of the reported sensors based on plasmonic materials are: an array of palladium-gold alloy nanoparticles operating as a hydrogen sensor [2], 30 nm diameter silver nanoparticles with 1 nm aluminium oxide shells as a glucose solution sensor [4], a metallic mirror with a dielectric layer and nanorings array as a refractive index sensor [69], three-layer graphene oxide on the gold substrate as a biomolecular sensor [70], bimetallic gold and aluminium nanoarrays as a whisky sensor [71], etc.

Sensitivity is a describing parameter of the plasmonic refractive index sensor. The complex-frequency shift $\Delta\tilde{\omega}$ on the local permittivity change $\Delta\varepsilon(r,\tilde{\omega})$ is derived from Maxwell's equations [64]:

$$\Delta\tilde{\omega} = -\tilde{\omega} \iiint_{V_\mathrm{p}} \Delta\vec{\varepsilon}(\vec{r},\tilde{\omega})\vec{\tilde{\mathrm{E}}}_{\mathrm{app}}(\vec{r})\vec{\tilde{\mathrm{E}}}(\vec{r})\mathrm{d}^3\vec{r}, \tag{2.9}$$

where $\tilde{E}(r)$ is the resonance mode of a bare metallic nanoparticle, $\tilde{E}_{\mathrm{app}}(r)$ is a modified version of $\tilde{E}(r)$ taking into account the local field corrections, V_p is the perturbation volume. Then, the sensitivity S_λ (nm/RIU) of the plasmon resonance based refractive index sensor depends on the shift of the plasmon resonance wavelength $\Delta\lambda_{\mathrm{res}}$ (nm) per unit change of the refractive index Δn (RIU) [72]:

$$S_\lambda = \frac{\Delta\lambda_{\mathrm{res}}}{\Delta n}. \tag{2.10}$$

The theoretical sensitivity of a sensor is usually higher compared with the experimentally measured one due to the particles immobilization on the substrate [5]. The permittivity and refractive index of the material and the whole system can be obtained by spectroscopic ellipsometry. When knowing the sensitivity and resolution R_{res} (nm), the detection limit DL (RIU) of a device can be obtained [73]:

$$DL = \frac{R_{\mathrm{res}}}{S_\lambda}, \tag{2.11}$$

which corresponds to the smallest refractive index change accurately measurable by the device.

Plasmonic sensors can also be described by the figure of merit (FOM, RIU^{-1}) [43]:

$$\mathrm{FOM} = \frac{S_\lambda}{\mathrm{FWHM}}, \tag{2.12}$$

where FWHM stands for the full width of the half maximum of the dip in the transmission spectra (nm). Additionally, a very important property of the sensor is its stability: the response of the sensor should not be affected by degradation of its composing materials [72].

LSPR can be used to enhance the efficiency of solar cells by control of the electrical properties in the active layer: electrons can either be injected or trapped due to free charge carrier generation after interaction with photons of a certain energy level [50].

Plasmonic nanocomposites can also be applied as broad-band anti-reflective coatings [49]. Metallic nanostructures offer a possibility of light concentration independent from the diffraction limit due to surface plasmon resonances [16]. The spatial modulation of the refractive index and, consequently, the diffraction efficiency are modified by arranging nanoparticles in diffraction gratings [25]. Sub-wavelength pitch periodic structures are required in refractive index sensors [74]. Nanoparticles arranged in diffraction grating-like structures change the refractive index and diffraction efficiency, which is related to the performance of the sensor [25, 75]. In order to create such geometries, advanced patterning methods are required.

2.5. Advanced patterning methods

All fabrication methods are divided into two categories: top-down and bottom-up. In terms of patterning, the top-down methods are various lithography techniques, while the bottom-up methods are self-assembly methods [16]. For example, plasmonic magnesium nanodisks capped with palladium can be fabricated by colloidal hole-mask lithography and electron-beam evaporation [9]. Previously, DLC was etched by pure oxygen plasma reactive ion etching through a silicon containing thermoplastic resist hard mask to create patterns with 500 nm depth and high precision vertical sidewalls [76]. Periodic structures in DLC:Ag nanocomposites can be obtained by plasma chemical etching through photoresist or an aluminium mask with the subsequent argon ion sputtering for complete removal of silver nanoparticles [77]. Sometimes, intricate designs require a combination of several methods. Fast, scalable, low-cost, and tuneable patterning methods are preferred and highly desirable [17, 25]. Among these are *holographic lithography* (HL, sometimes referred to as *laser interference lithography*), and *direct laser interference patterning* (DLIP). The drawback of interference techniques is that they can only produce periodic patterns.

A variety of complicated periodic structures (rotational symmetries) can be obtained by employing various laser interference setups: 4-fold with 2 beams and 2 exposures [78], 5-fold and 8-fold with 5 and 8 beams [79], 8-fold with 2 beams and 4 exposures [80], 10-fold with 2 beams and 5 exposures [81], 12-fold with 3 beams and 2 exposures [82], 18-fold with 2 beams and 9 exposures [83], etc. By introducing the phase difference in the interfering beams, a larger variation of periodic patterns becomes feasible, e.g., arrays of *X* shapes [84]. With the use of the

scanning sample surface with interfering beams, periodic structures with inner periodic features can be created [85]. However, for most applications, simple geometries are sufficient.

In both HL and DLIP, a single exposure with two interfering beams yields a one-dimensional (1D) pattern (periodicity in a single direction). Application of multiple exposures of two beams with rotation between them, or interference of 3 and more beams will result in two-dimensional (2D) patterns. 3D patterns are also possible in HL when using the appropriate photosensitive materials [86].

The main difference between HL and DLIP is the material affected by the laser [87]. In the HL case, the sample must be coated with a photosensitive material (a positive or negative photoresist, a photopolymer [88]). After developing, the structure is in the photoresist layer, and, in order to transfer it to the substrate, an additional step is required, e.g., reactive ion etching [89]. DLIP, as the term suggests, is a direct approach: the material is patterned during the DLIP process without the need for additional films or etching steps.

Both of these light interference based techniques do not require any masks as the conventional lithography techniques do [90, 91]. Commonly, HL employs continuous-wave lasers with a long coherence length [90], while DLIP uses pulsed lasers with high energy density [92]. DLIP is advantageous over HL due to the possibility to work in any lighting conditions, i.e., there is no need for a dark room to avoid the unwanted exposure of the photoresist. Moreover, it is less sensitive for the sample stability as exposures are imposed over ultra-short time scales. There are several possible interferometer geometries: Mach-Zehnder, Lloyd's mirror, Schwarzschild optics, 4f lens system [93], etc. Pulsed lasers feature a shorter coherence length than continuous-wave lasers due to their broad bandwidth [94]. Thus, only symmetrical interference geometries (e.g., 4f lens systems) can be used with pulsed lasers.

Femtosecond laser (fs-laser) micromachining is capable to cause permanent changes to virtually any material. It is even possible to obtain periodic structures without the laser interference pattern: this phenomenon is called laser induced periodic surface structures (LIPSS). LIPSS occur on the surface of solid materials after irradiation with linearly polarised multiple laser pulses [95]. However, it appears that the lines in LIPSS patterns are not always predictable or straight – they exhibit a wavy pattern [96]. Nonetheless, LIPSS are still being employed for patterning of plasmonic materials [92, 97, 98].

The nanoparticles size distribution in nanocomposites is typically determined during the deposition by applying various technological parameters [99], but, in order to alter the size distribution in already deposited films, ultrashort (e.g., femtosecond-range) pulse lasers can be applied [63]. The imposed features depend on the laser wavelength, the pulse energy, the energy density, the repetition rate, the pulse duration, etc. [100]. Commonly, fs-laser effects on the material are classified into ablation and damage [100]. Ablation is the removal of a material from the sample surface [101]. For ablation, shorter laser pulses (e.g., femtosecond-range) are preferred due to superior accuracy, the reduced heated zone, and the absence of plasma shielding [95].

Femtosecond lasers do not cause thermal effects during material processing, however, at high repetition rates, these effects are still possible. In general, laser micromachining produces a complicated pattern on the sample surface by scanning the beam over the surface. Another method is laser micromachining using the interference field, which allows for more complicated, repetitive patterns without a need for scanning [100].

Carbon containing thin films can be ablated, delaminated or graphitized under laser irradiation [63]. It is reported that, for DLC (specifically, tetrahedral amorphous carbon), surface graphitization starts at 1000 K temperature, while ablation occurs at the sublimation temperature of 4000 K [102]. For metal nanoparticles, laser irradiation can induce melting, coalescence or fragmentation [103]. Some materials, such as polycarbonate, undergo swelling after laser irradiation [104].

Further, some examples of laser affected materials are presented. Mousavi *et al*. patterned tetrahedral amorphous carbon to use it as a protective, lubricant-free film on tools. Friction was reduced by 20%, and wear was reduced by 10% [105]. Ooms *et al*. used a continuous wave CO_2 laser (λ = 10 μm) to pattern magnetron sputtered non-continuous gold films of various thicknesses into nanoparticles. By changing the laser scan rate which determined the applied fluence and energy flux to the sample, they were able to obtain different-sized particles resulting in different colours on the sample surface. The method proved to be cheap and accessible, but diffraction limited [17]. Vogel *et al*. applied nanosecond pulsed laser irradiation to change the shape of colloidal gold nanoparticles. The idea was based on the excitation of LSPR. Initial rod-like, triangular, pentagonal, and hexagonal shapes were successfully converted to spherical shapes by irradiating with the laser wavelength thus matching the LSPR of every shape [35]. Zillohu *et al*. tested selective embedding of silver into a polyvinylidene fluoride film by using the same laser which is commonly used in Raman spectroscopy (λ = 532 nm). The resulting nanocomposite had a blue shift in plasmonic resonance compared with pure silver nanoparticles because the polymer disrupted the plasmonic coupling of nanoparticles [52]. Palermo *et al*. worked on the method in order to create submicrometre stripes of gold nanoparticles in a polyvinyl alcohol matrix doped with $HAuCl_4$ by two-photon direct laser writing. They successfully obtained stripes with a periodicity of 2, 10, and 100 μm; however, an attempt to fabricate the 0.5 μm pitch resulted in a dense area of gold nanoparticles without any apparent periodicity [14]. Peláez *et al*. reported the fabrication of periodic structures of silver/gold alloy nanoparticles by the phase mask nanosecond laser interference technique. The technique proved to be versatile in creating many different periodic patterns, including lines, squares, rhombuses, triangles, and oblong shapes [25].

2.5.1. *Ablation threshold*

Upon laser irradiation, materials absorb energy in the form of heat, which increases the temperature. In transparent materials, absorption happens in the volume shaped as a cylinder with a two-dimensional temperature gradient. Ablation appears on the surface of the material when its melting temperature has been

reached. In absorbing (metallic) materials, laser radiation penetrates a small distance into the material. This distance is called *skin depth* and depends on the electrical conductivity of the material. Free carriers absorb radiation, and the temperature increases, which causes the stress and distortion of the surface. Ablation appears due to the mechanical failure, the melting of the surface, or a combination of these [106]. High refractive index materials usually feature lower threshold values compared to the low refractive index materials when material damage is related to nonlinear ionization [107].

The intensity of light I in the interference pattern at a given point on the sample is described as:

$$I(\vec{r}) = I_1(\vec{r}) + I_2(\vec{r}) + 2\sqrt{I_1(\vec{r})I_2(\vec{r})}\cos\left(\varphi_1(\vec{r}) - \varphi_2(\vec{r})\right), \qquad (2.13)$$

where φ is the phase of the light wave. A schematic representation of light intensity in the interference pattern of two beams is presented in Fig. 2.4.

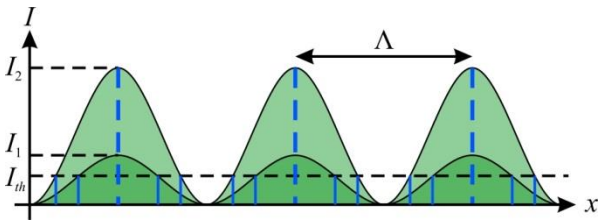

Fig. 2.4. Schematic representation of laser intensity distribution in the interference field when irradiated at two different laser intensity levels ($I_1 < I_2$), which both are above ablation threshold intensity I_{th}. Λ is the distance between two interference maxima, which results in the pitch of the fabricated periodic pattern.

The ablation threshold is the smallest laser energy value which is capable to remove the material [100]. Material ablation rate a (cm per pulse) depends on the applied laser fluence Φ (mJ/cm^2) as [108]:

$$a = \frac{1}{\alpha}\ln\frac{\Phi}{\Phi_{\text{th}}}, \qquad (2.14)$$

where α is the absorption coefficient (cm^{-1}), and Φ_{th} is the threshold fluence (mJ/cm^2). The ablation threshold value depends on the material and the laser chosen for the fabrication [109]. Furthermore, the ablation threshold of nanocomposite materials is different from ablation thresholds of its separate components [110]. The threshold value can also be reduced by the so-called incubation effect, i.e., by applying multiple laser pulses. The incubation effect is explained as the ability of the material to store energy [111]. Storing of energy creates damage accumulation, which weakens the molecular bonds and changes the surface chemistry or topography [112].

Surface modification is possible even below the ablation threshold. In such cases, the material is not removed, but its properties are changed. These modifications are referred to as *gentle ablation* [95], a precursor to the surface damage [113], melting threshold [114], surface cleaning boundary [115], visible damage threshold [116], etc. Similarly, the lowest laser fluence required to induce the pattern on the sample surface can be termed as *patterning threshold*.

3. WORK METHODOLOGY

3.1. Fabrication of nanocomposite thin films

3.1.1. *Magnetron sputtering*

Nanocomposites consisting of hydrogenated amorphous diamond-like carbon and copper (DLC:Cu) or silver (DLC:Ag) nanoparticles, as well as pure DLC thin films, were deposited by the reactive unbalanced magnetron sputtering method in a custom-built system. The principal scheme of the method is depicted in Fig. 3.1. Carrier gas ions are incident on the target, and, with enough energy, the target atoms are sputtered. The application of the magnetic field increases the sputtering rate [117]. In the unbalanced magnetron sputtering mode, the magnetic field in the poles is strengthened, and field lines are directed towards the surface of a substrate. A bias power can be applied to the substrate in order to change the plasma distribution and to accelerate the ions towards the substrate surface [110]. There are two main modes in unbalanced magnetron sputtering: direct current and pulsed current. The direct current mode applies constant power, while the pulsed mode additionally applies high power pulses [118].

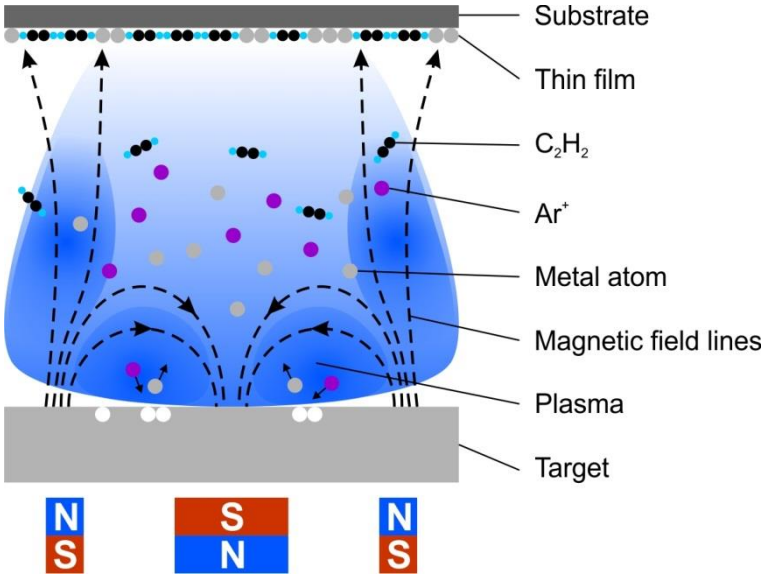

Fig. 3.1. Schematic principle of reactive magnetron sputtering from argon and acetylene gases with a metal target. Adapted from [110].

DLC and DLC:Ag samples were deposited in the direct current mode, while DLC:Cu samples were deposited in the pulsed mode. The pulse time was 100 μs, the duty cycle was 1%, and the frequency was 100 Hz. The mixture of argon and acetylene gas was used, and nanoparticles were incorporated into the film during deposition when using a copper (99.99% purity, *Kurt J. Lesker Company*) or silver (99.99% purity, *Kurt J. Lesker Company*) target. During the deposition of a pure DLC film (without metal nanoparticles), a carbon (graphite) target (99.999% purity,

Kurt J. Lesker Company) was used. Acetylene (99.6% purity) was used as a reactive gas, while argon (99.99% purity) was a carrier gas. The distance between the target and the substrate was 8–10 cm. The base pressure was up to $9.0 \cdot 10^{-4}$ Pa, and the work pressure was up to 0.89 Pa. Thin films were deposited on two different substrates: 0.5 mm thick, (100) orientation, n-type crystalline silicon (*Siltronix*), and 1 mm thick fused quartz (*University Wafer*), which were grounded, except for samples DLC:Ag-2, DLC:Ag-2', DLC:Ag-6, where the sample bias was -100 V, -150 V, -50 V, respectively. The duration of deposition was chosen in one of two ways: constant film mass (DLC:Cu) or constant thickness (DLC, DLC:Ag, 60 nm). Deposition conditions (Table 3.1) were chosen to deliver a variety of nanoparticle sizes as it was similarly reported in [119].

Table 3.1. Sample notations and magnetron sputtering conditions for DLC, DLC:Ag and DLC:Cu samples.

Sample	Gas flow (sccm)		Supply power		Pulse current (A)	Duration of deposition (s)	Target
	Ar	C_2H_2	Voltage (V)	Current (A)			
DLC-0	70	11.7	432-450	0.09-0.11	DC	784	C
DLC-0'	70	11.7	430	0.09-0.12	DC	1597	C
DLC:Ag-2	80	7.8	405-413	0.12-0.15	DC	321	Ag
DLC:Ag-2'	80	7.8	396	0.1	DC	205	Ag
DLC:Ag-6	80	7.8	387-392	0.1	DC	223	Ag
DLC:Ag-7	70	11.7	387-392	0.1-0.12	DC	300	Ag
DLC:Ag-8	70	11.7	369-379	0.09-0.1	DC	276	Ag
DLC:Ag-14	80	5.4	404	0.09-0.13	DC	171	Ag
DLC:Ag-14'	80	7.8	395	0.08-0.09	DC	295	Ag
DLC:Ag-15	80	5.4	420	0.1	DC	178	Ag
DLC:Cu-14	63	60.3	590	0.04	8	464	Cu
DLC:Cu-27	63	30.5	595	0.02	4.4	450	Cu
DLC:Cu-33	63	7.8	580	0.02	2.4	458	Cu
DLC:Cu-44	63	3.9	580	0.02	2.4	425	Cu
DLC:Cu-49	63	14.9	730	0.16	30	60	Cu

3.1.2. *Electron beam evaporation*

Pure silver thin films (sample Ag-100) were deposited by employing the e-beam evaporation technique in a *CUBIVAP* system. The basic principle of the technique is illustrated in Fig. 3.2. A magnetically steered electric beam vaporises the target whose species are then used to physically deposit the film [120]. The pressure in the sample chamber was less than 0.13 Pa. The purity of the silver target in a tungsten crucible was 99.99%. The deposition rate was approximately 1.3 Å/s. The target thickness of thin Ag films was 60 nm.

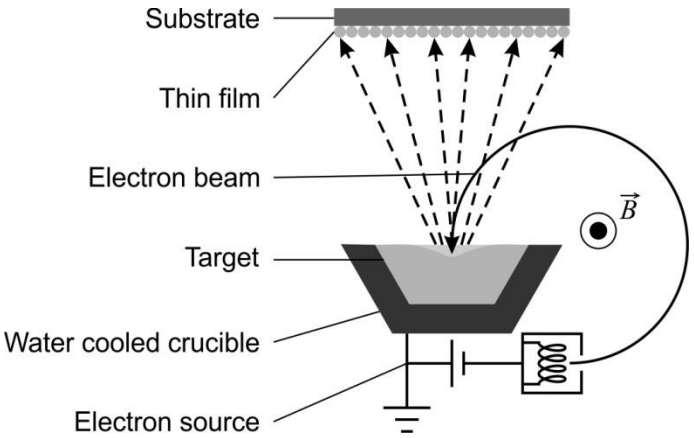

Fig. 3.2. Schematic principle of electron beam evaporation. Here, *B* stands for the magnetic field. Adapted from [121].

3.1.3. *Holographic lithography and direct laser interference patterning*

The common element of holographic lithography (HL) and direct laser interference patterning (DLIP) is the imposition of periodic structures in material by employing the laser interference field. The principal scheme of HL is illustrated in Fig. 3.3, while the DLIP scheme is illustrated in Fig. 3.4.

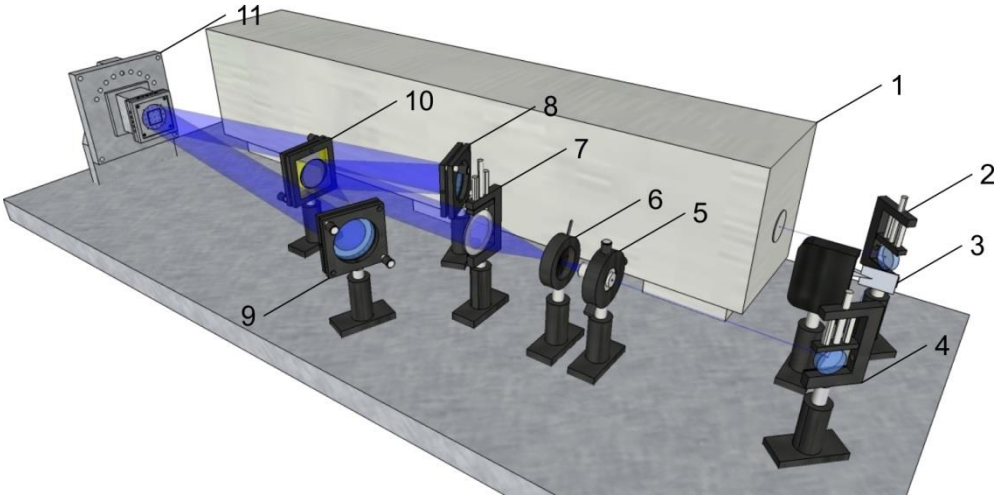

Fig. 3.3. The principal scheme of the holographic lithography system: 1 – laser, 2, 4, 8, 9 – mirrors, 3 – computer controlled shutter, 5 – objective, 6 – pinhole, 7 – lens, 10 – diffraction grating beam splitter, 11 – rotatable sample holder. Published in [A2].

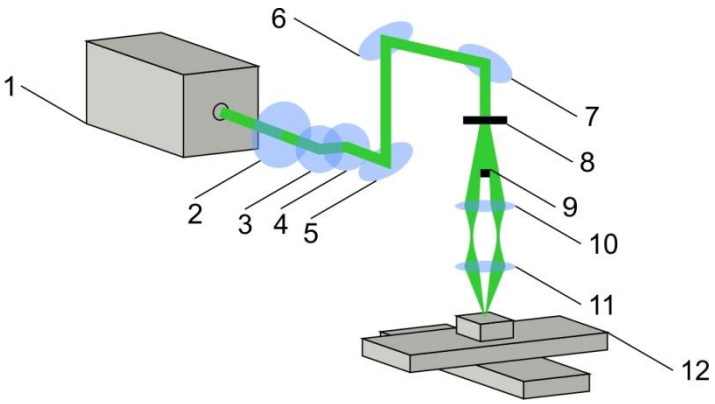

Fig. 3.4. The principal scheme of the direct laser interference patterning system: 1 – laser, 2 – half-wave plate, 3, 4 – Brewster angle polarisers, 5–7 – dichroic mirrors, 8 – diffractive optical element, 9 – mask, 10, 11 – lenses (4f system), 12 – XYZ stage. Elements 2–4 comprise an attenuator. Adapted from [122, 123].

Pitch Λ of the pattern (nm) in interference-based techniques can be determined as [124]:

$$\Lambda = \frac{\lambda}{2n \sin\theta}, \tag{3.1}$$

where λ is the laser wavelength (nm), n is the refractive index of the surrounding medium (in this particular case, it was air), and θ is the angle of incidence. As it can be seen from the equation, when the surrounding medium is air (n = 1), the smallest possible pitch is equal to half the wavelength (when θ = 90°). In order to lower the pitch further, a laser with a shorter wavelength or immersion mediums is/are necessary [89]. In HL, the angle of incidence was changed by changing the positions of the mirrors, while in DLIP it was changed by using the diffractive optical element (DOE) with a different pitch.

Holographic lithography was employed to make patterns in a positive tone ma-P 1205 photoresist (Micro resist technology) on 2 × 2 cm^2 float glass (*Gravera*) substrates. The photoresist was spin-coated at 500–700 rpm for 6 s and at 3000–3200 rpm for 30 s. The resulting thickness of the photoresist layer was 0.5 μm [125]. For the exposure, a 442 nm wavelength, 90 mW power HeCd laser (*CVI Melles Griot 4074-P-A03*) was employed. The laser beam was expanded with a spatial filter: 40×, 0.65 numerical aperture microscope objective (*Lomo*) and 30 μm aperture (*Standa*). It was collimated with 50 mm diameter, 75 mm focal length convex lens (*Eksma Optics*). The beam was split with 50 × 50 mm^2, 1800 lines per millimetre diffraction grating beam splitter (*Thorlabs*). The split beams were overlapped on the sample with a 50 mm dielectric mirror (*Eksma Optics*). The final diameter of the interfering beams was 5 cm. The time of the exposure varied from 4 to 9 seconds, and the laser power was from 89.7 to 90.8 mW (the power density at the sample was 2.9–4.3 mW/cm^2, respectively). After the exposure, the samples were developed in an MF-26A developer (*Micro resist technology*) for 9–14 s.

Direct laser interference patterning was performed on DLC:Ag, DLC, and Ag samples by using the second harmonic (515 nm wavelength) of Yb:KGW *Pharos*

laser (*Light Conversion*) and a *FemtoLab* micro-/nanomachining workstation (*Altechna R&D*). The pulse duration of the laser was 290 fs, the repetition rate was 40 kHz, and the beam size was 75×75 μm^2. In order to get a more uniform square light intensity distribution in the beam, its Gaussian shape was expanded and cropped by passing through the square aperture. DOE was used to split laser beam into two symmetrical (equal intensity) beams and unwanted diffraction orders were blocked with the mask. A 4f lens system was used to overlap the beams onto a single area on the sample surface, which resulted in an interference pattern. The laser, the XYZ sample stage, the attenuator, and DOE were controlled by *SCA* software (*Altechna R&D*). The beam was circularly polarised in order to avoid LIPSS. In order to increase the patterned area, irradiation was performed in a 4×4 array, thus giving the total patterned area of 300×300 μm^2. The applied laser fluence for DLC:Ag samples was 1–17 mJ/cm^2, for DLC it was 1–145 mJ/cm^2, and for a pure silver thin film sample it was 6–145 mJ/cm^2. In all the cases, the applied number of the pulses was between 1 000 and 125 000.

3.2. Characterisation of the properties of thin films

3.2.1. *Microscopy techniques and image analysis*

3.2.1.1. *Optical microscopy*

Optical microscope *B-600MET* (*Optika*) was employed for the visualization of periodic patterns in a photoresist after HL and whole laser irradiated areas in DLC after DLIP. Diffraction limited optical microscopy is not suitable for the imaging of diffraction patterns and nanoparticles in the nanometre scale. Only the highest pitch was visible when using a 100× objective. A 20× objective was suitable to obtain the images, from which, the diameters of the whole irradiation spots were determined and further used in the ablation threshold determination.

Derivative information from optical microscopy images

When a DLC sample was irradiated with elevated fluence Φ (6-145 mJ/cm^2), dark, mostly circular areas were visible under the microscope. For each set of laser irradiation parameters, 16 diameter D values (μm) were obtained (from a 4×4 array) and then averaged. In some cases (at a very high fluence or number of the applied pulses), the number of the measured diameters was reduced to 12 due to the overlap of the irradiated areas, which made it impossible to determine the edges of the affected circles in the centre of the array.

In order to determine the threshold fluence Φ_{th}, the fitting in the *Origin* software was employed to equation [126]:

$$D^2 = 2w^2 \ln \frac{\Phi}{\Phi_{\text{th}}}, \tag{3.2}$$

where w is the estimated laser spot size on the sample surface (μm). Equation (3.2) is valid for Gaussian shaped beams, and linear fitting is valid for the plot of D^2 dependence on ln(Φ).

After observation of DLC:Ag samples under optical microscope, it was determined that laser irradiation was much more uniform within the squares than in

the DLC case, and no dark circles were observed. Thus, it was not possible to determine the DLC:Ag ablation threshold by using the same method.

3.2.1.2. *Scanning electron microscopy*

Most of the samples were investigated by employing a scanning electron microscope (SEM) *Quanta 200 FEG* (*FEI*). Silver containing nanocomposite thin films on the silicon substrate and pure silver thin films on both quartz and silicon substrates were also investigated while employing a SEM *S-4800* (*Hitachi*). The principal scheme of SEM is depicted in Fig. 3.5. In the SEM, a highly focused electron beam interacts with the sample in a vacuum chamber, and generated secondary electrons are used to image the surface of the sample [127]. In the first system, the working distance was 7.3 mm, the accelerating voltage was 30 kV, the emission current was 160 μA, and the scan dwell time was 10 μs. In the second system, the working distance was 6 mm, the accelerating voltage was 15 kV, the beam current was 10 μA, and the scan dwell time was 15 μs.

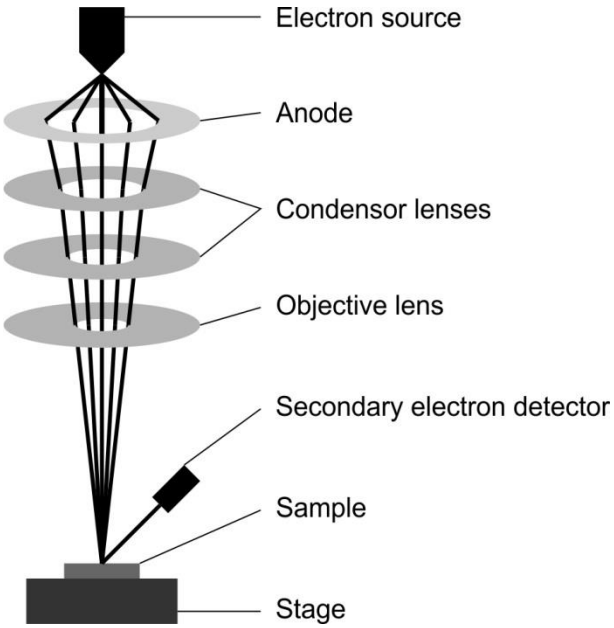

Fig. 3.5. The principal scheme of a scanning electron microscope. Adapted from [127].

3.2.1.3. *Helium ion microscopy*

Helium ion microscopy (HIM) is a method which is similar to SEM imaging, but, instead of the electron beam, it uses an ion beam. Since ions have a higher mass than electrons, the diffraction limit in HIM is lower than in SEM. Also, ions produce more secondary electrons (SE, 3–9 per ion) than electrons (1 per electron) [128]. The comparative scheme of electron and helium ion beams penetration into a material is shown in Fig. 3.6. In the electron beam case, SEs are produced from a larger area, and the obtained image contains non-local information. To the contrary, the helium ion beam excites a narrower volume, at which, SE can escape, and it

produces information in the image from the surface of the probed area. The depth of the field in HIM could be as much as 5 times larger than in SEM [128].

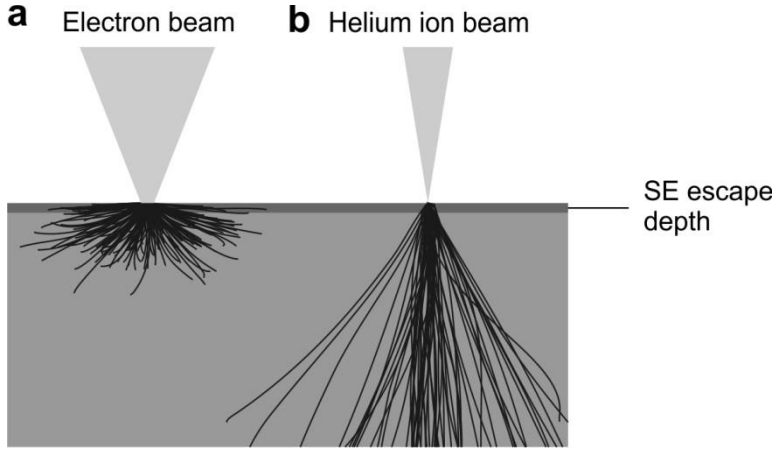

Fig. 3.6. Comparison of the electron beam (a) and helium ion beam (b) interaction with a sample. The black lines represent electron and ion beam paths inside a material, respectively. SE stands for secondary electrons. Adapted from [128].

The samples which were not sufficiently conductive to be measured by using SEM (DLC on quartz and silicon, DLC:Ag on quartz) were measured by using a helium ion microscope *ORION NanoFab* (HIM, *Zeiss*). The sample bias (-60 V) and a flood gun (600 eV) were applied for charge neutralisation. The working distance was 10 mm. 25 kV accelerating voltage and 0.260 pA beam current was applied. The scan dwell time was 2 μs.

The employed HIM additionally has a gallium ion beam which possesses sufficient energy to remove the material. This beam was used to remove a wedge-shaped volume in the thin film in order to reveal the cross-section. The cross-section was then imaged by helium ion beam.

Derivative information from SEM and HIM micrographs

Since it was not possible to determine the threshold fluence for DLC:Ag from optical microscopy, it was assumed that it might be possible to do this from the analysis of the irradiated width. 18 μm field of view microphotographs were used to determine the width W of the laser affected lines (Fig. 3.7a). The width was measured for each line that was visible in the image and then averaged. In some cases, the edge between the ridge and the groove was not clear due to subtle intensity variations in sine-like interference field intensity, and thus these micrographs had to be omitted from the analysis of the width in order to avoid larger errors.

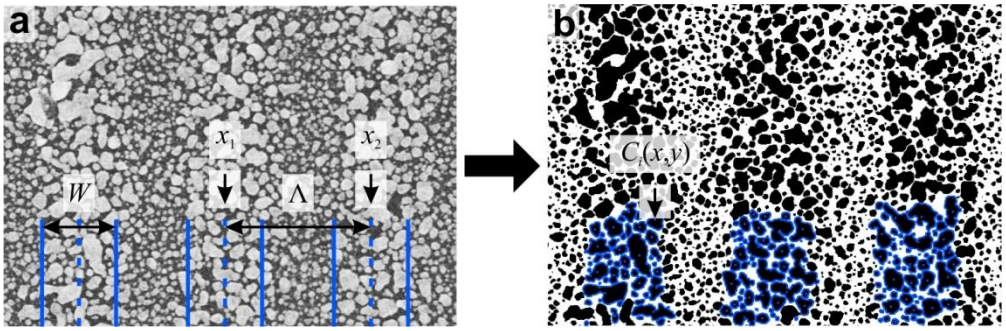

Fig. 3.7. Various parameters measured from SEM micrographs (a): W – width of the irradiated line, x_1, x_2 – centre coordinates of the irradiated line, Λ – pitch of the periodic pattern. (b) The corresponding black (particles) and white (background) image serves for nanoparticle size distribution analysis with marked centres $C_i(x,y)$ of nanoparticles. Published in [A4], presented in [B11].

3.2.1.4. *Transmission electron microscopy*

Transmission electron microscope (TEM) *Tecnai G2 F20 X-TWIN* (*FEI*) with a 200 kV Schottky field emission electron source was used to investigate the cross-section of all DLC:Cu samples. Another TEM, *Talos F200X* (*FEI*), at 200 kV acceleration voltage was used to investigate two of DLC:Ag samples: the one with the lowest silver content (DLC:Ag-2), and the one with the highest content (DLC:Ag-15). The imaging was performed in the regular mode and in the high-angle annular dark-field mode. In the regular mode, the electron beam interacts with the sample, and the transmitted electrons are used to image the internal structure of the sample [127]. The high-angle annular dark-field mode provides images in atomic resolution and is sensitive to the atomic number of the elements composing the material [129].

3.2.1.5. *Fast Fourier transform*

A rough estimate of the DLC:Ag patterning threshold could also be determined from fast Fourier transforms (FFTs). Fourier transformation changes the signal from the spatial domain to the frequency domain. 2D FFT for image processing is defined as [130]:

$$F(u,v) = \int_{-\infty}^{\infty}\int_{-\infty}^{\infty} f(x,y)e^{(-2\pi(ux+vy))}dxdy, \tag{3.3}$$

where x and y are spatial domain dimensions, u and v are spatial frequencies. The general solution is complex [130]:

$$F(u,v) = F_{\mathrm{R}}(u,v) + iF_{\mathrm{I}}(u,v), \tag{3.4}$$

where R and I denote the real and the imaginary parts of the function, respectively.

It can be assumed that the applied laser fluence is above the patterning threshold when the periodic pattern is present in the sample. When the pattern is very faint, its existence can be proven by FFT as it has a diffraction pattern. Thus,

the patterning threshold is in between the two values of the applied fluence when the diffraction pattern is not visible or is present in the FFTs.

SEM microphotographs with 18 μm field of view and 15 μm field of view HIM images were used to determine the pitches of the periodic structures. In order to avoid ambiguities, this investigation was carried out by using *ImageJ* software [131]: after assigning the scale of the micrograph, fast Fourier transform was calculated, and, from the first maximum in it, the pitch was determined.

3.2.1.6. *Distribution of nanoparticle sizes*

SEM micrographs with a 3 μm field of view were used in the nanoparticle size distribution analysis. For this, *ImageJ* software with *Analyze Particles* plugin was used [132]. The threshold value was set manually for every image in order to get the best black and white representation of the sample structure and the areas of particles (Fig. 3.7b). Additionally, the background subtraction, the Gaussian blur, and the watershed functions were applied. In such cases when automatic functions could not satisfactorily resolve each particle, the boundaries between two nearby particles were manually corrected by introducing a one pixel-wide gap. The particles that were touching the edge of the microphotograph were not included in the investigation due to the uncertainty of their sizes. Furthermore, the obtained data of the particle area was filtered in order to obtain only the particles in the laser affected lines. For this, the previously determined W and central coordinates of each line were used (see Fig. 3.7 for explanations of notations): if centre C_i of the particle is within the irradiated line width, it was included. In addition, the particles whose size corresponds to one pixel in the image were omitted from the analysis because they most probably are from the noise in the image. After filtering, the areas of nanoparticles were calculated into diameters. Here, it was assumed that the particles are perfectly round. The diameters were grouped into so-called bins of 5 nm and plotted as a percentage of particles (compared to all the laser affected particles in the image) in each bin. Then, the data from these histograms was fitted in *Origin* software to obtain lognormal distribution which is described by [133]:

$$y = y_0 + \frac{A}{\sqrt{2\pi}\omega x} e^{\frac{-\left(\ln\frac{x}{x_c}\right)^2}{2\omega^2}}, \tag{3.5}$$

Where the y coordinate stands for the particle number in percentage, and the x coordinate stands for the particle diameter, y_0 is the offset, A is the area under the curve, ω is the logarithm of standard deviation, and x_c is the centre coordinate of the function. The mean value μ and standard deviation σ of this function can be calculated as:

$$\mu = e^{\ln x_c + \frac{\omega^2}{2}}, \tag{3.6}$$

$$\sigma = \mu\sqrt{e^{\omega^2} - 1}. \tag{3.7}$$

A variable is lognormally distributed if its logarithm is normally distributed. Lognormal distribution is a skewed distribution with low average values and large variations. Compared to another very popular distribution – the Gaussian one, which is symmetrical – the lognormal distribution has a benefit that its values cannot be

negative [134]. Since the size of a nanoparticle cannot be negative, the lognormal distribution is the most common function for the fitting of this parameter.

The density of nanoparticles in the thin film was calculated as the total number of nanoparticles divided by the total area of the SEM micrograph under investigation. The particle area fraction was calculated as the ratio of the total area of the particles (i.e., the area covered by particles) and the total investigated area (the area of the micrograph).

Particle size distribution analysis was not carried out on HIM images because HIM produced very bright edges of the particles, and the inside of the particles was the same shade as the background thus making it impossible to automatically detect full particles without any 'holes' in them within the applied *ImageJ* software.

3.2.2. *Chemical analysis techniques*

3.2.2.1. *Energy dispersive X-ray spectroscopy*

Energy dispersive X-ray spectroscopy (EDS) was employed to determine the elemental composition of the deposited films. *Quantax 200* system with an *XFlash 4030* detector (*Bruker*) in a *Quanta 200 FEG* (*FEI*) scanning electron microscope was used. The primary energy used for measurements was 5 keV. The obtained concentrations of elements were weight percentages which were calculated into atomic percentages. For EDS, thin films on silicon substrates were used. Since the films are very thin, EDS also gathers some information from the substrate, and silicon concentration had to be eliminated when calculating the concentration of the elements in the films.

3.2.2.2. *Raman spectroscopy*

Raman spectroscopy was employed to determine carbon allotropes in the deposited thin films and to investigate the SERS effect. Raman spectroscopy is based on the Raman scattering effect. The sample is illuminated by a monochromatic laser beam which interacts with the molecules and is scattered inelastically due to the vibrations of the molecules [135].

For the measurements, a *Renishaw inVia* Raman spectrometer with a 532 nm wavelength 45 mW power excitation laser and a 50×, 0.75 numerical aperture microscope objective was employed. The laser power on the sample was 1%, and the exposure time was 10 s. The background was subtracted from the obtained spectra, and the peaks were fitted to the Gauss function in *Origin* software:

$$y = y_0 + \frac{A}{\omega\sqrt{\frac{\pi}{2}}} e^{-2\frac{(x-x_c)^2}{\omega^2}}, \tag{3.8}$$

Where the y coordinate stands for the intensity, the x coordinate stands for the wavenumber, y_0 is the offset, x_c is the centre of the peak (i.e., the coordinate of its maximum position), ω is the width of the peak, and A is the area under the curve.

3.2.3. *Techniques to determine the optical properties*

3.2.3.1. *Ultraviolet-visible-near infrared spectroscopy*

Ultraviolet-visible-near infrared (UV-Vis-NIR) spectroscopy was employed to obtain the optical transmittance and the reflectance spectra. *AvaSpec-2048* (*Avantes*) fibre or a *V-670* (*Jasco*) spectrometer and an *AvaLight-DHC* (*Avantes*) light source were used for this purpose. In order to obtain the transmittance and reflectance of the thin films, the reference and dark spectra were recorded first. The dark spectrum is recorded when the lamp is switched off. The reference spectrum for transmittance was recorded for the quartz substrate without a film, and the reference spectrum for reflectance was recorded from the aluminium mirror. From here, transmittance T and reflectance R were calculated as:

$$T = \frac{I_{\mathrm{T}} - I_{\mathrm{dark}}}{I_0 - I_{\mathrm{dark}}}; \tag{3.9}$$

$$R = \frac{I_{\mathrm{R}} - I_{\mathrm{dark}}}{I_0 - I_{\mathrm{dark}}}, \tag{3.10}$$

where I_{T} and I_{R} is the intensity of the transmitted and reflected light, respectively, I_{dark} is the intensity registered without the light being present, I_0 is the reference intensity (counts).

From transmittance T and reflectance R measurements, absorbance A was calculated:

$$A = 1 - T - R. \tag{3.11}$$

This equation is valid for specular reflections and for quantities in arbitrary units. If the reflection is diffused, its term should also be subtracted. With nanoparticles being present on the substrate surface, it is expected for the light to be scattered. However, when particles are embedded in a matrix, the surface could be sufficiently smooth for the reflection to be specular.

In order to investigate the scattering properties of thin films, reflection measurements were carried out in the integrating sphere *RTC-060-SF* (*Labsphere*) with a stabilized halogen light source *SLS301* (*ThorLabs*) and a *Maya 2000Pro* spectrometer (*Ocean Optics*) and with a trap mounted at the position of specular reflection. The samples on quartz substrates were mounted at the back port of the integrating sphere at an 8° angle of incidence. The trapped specular reflection light does not reach the detector, and only the signal from diffused reflection is registered [136].

3.2.3.2. *Spectroscopic ellipsometry*

Principle of spectroscopic ellipsometry technique

Spectroscopic ellipsometry (SE) is a nondestructive optical technique for the determination of optical constants and the thickness of thin films. It is based on the change of polarisation of light upon its interaction with the sample either in the transmission mode or, more commonly, in the reflection mode [137]. It is possible to evaluate films whose thickness ranges from 0.1 nm to 200 μm, with a resolution of angstroms [138]. The sample surface does not have to be perfectly smooth, but its

roughness should be smaller than the wavelength of light used for the measurements because a higher roughness increases the scattering of light and it, in turn, results in measurement errors [139].

General ellipsometry measures two ellipsometric parameters: the amplitude ratio Ψ and the phase difference Δ. The parameters are related to Fresnel reflection coefficients as [140]:

$$\tan(\Psi)e^{i\Delta} = \frac{r_\mathrm{p}}{r_\mathrm{s}} = \rho, \tag{3.12}$$

$$\tan^2(\Psi) = \frac{R_\mathrm{p}}{R_\mathrm{s}}, \tag{3.13}$$

where r_p and r_s are Fresnel coefficients of p (parallel) and s (perpendicular) polarisation components, respectively, $R_\mathrm{p} = r_\mathrm{p} r_\mathrm{p}^*$ and $R_\mathrm{s} = r_\mathrm{s} r_\mathrm{s}^*$ are polarised reflectivities (* denotes a complex conjugate). Equation (3.12) is denoted as the fundamental ellipsometric equation. The principle of ellipsometry is illustrated in Fig. 3.8.

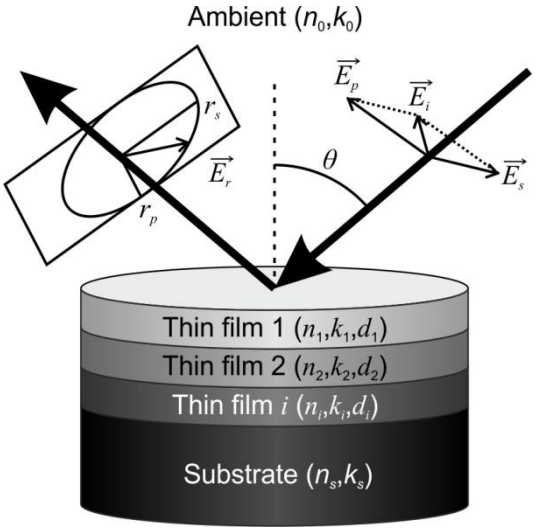

Fig. 3.8. A scheme of polarised light interaction with a multilayered sample in the reflection mode. Here, n is refractive index, k is extinction coefficient, d is thickness, E is electric field, r is Fresnel coefficient, and θ is angle of incidence.

Traditionally, spectroscopic ellipsometry results are also presented by using the Ψ and Δ parameters. However, the actually measured parameters in SE are different and denoted as C, N, and S [141]:

$$C = \sin(2\Psi)\cos\Delta, \tag{3.14}$$

$$N = \cos(2\Psi), \tag{3.15}$$

$$S = \sin(2\Psi)\sin\Delta. \tag{3.16}$$

These parameters are not independent because [141]:

$$C^2 + N^2 + S^2 = 1. \tag{3.17}$$

From here, Eq. (3.12) for non-depolarising samples can be rewritten as:

$$\rho = \frac{C + iS}{1 + N}. \tag{3.18}$$

The dielectric constant of sample ε_s is related to ellipsometric parameters as [137]:

$$\varepsilon_s = \varepsilon_a \sin^2(\theta)\left(1 + \tan^2(\theta)\left(\frac{1-\rho}{1+\rho}\right)^2\right), \tag{3.19}$$

where ε_a is the ambient dielectric constant, and θ is the angle of incidence.

The advantage of spectroscopic ellipsometry is that it is not influenced by light source intensity fluctuations and ambient light [140]. It is non-destructive, it does not require high vacuum or special sample preparations [142]. The most significant disadvantage of SE is its non-direct nature, i.e., the obtained ellipsometric parameters do not yield any specific information about the sample, and modelling is thus needed [143].

Experimental setup of spectroscopic ellipsometry measurements

SE measurements were obtained by using a variable angle rotating compensator spectroscopic ellipsometer *GES5-E* (*Semilab*) in the reflection mode (Fig. 3.9). It is employed with a xenon lamp which produces a 185–2000 nm wavelength light spectrum. The reflected light from the sample was detected by a UV-Vis CCD detector with a range of 190–900 nm and a resolution of 0.8 nm. The CCD detector records full spectra in 2 s. The angle of incidence was chosen up to 75°. The lowest angle of incidence depended on the noise level of the signal from the sample and was between 30° and 45°. The step in the measured angle was 5°. Two beam modes were employed: the parallel beam (3 mm × 12 mm at 75°), and the microspot (365 µm × 470 µm at 75°). The number of measured spots (1–5) depended on the chosen beam mode and the sample size.

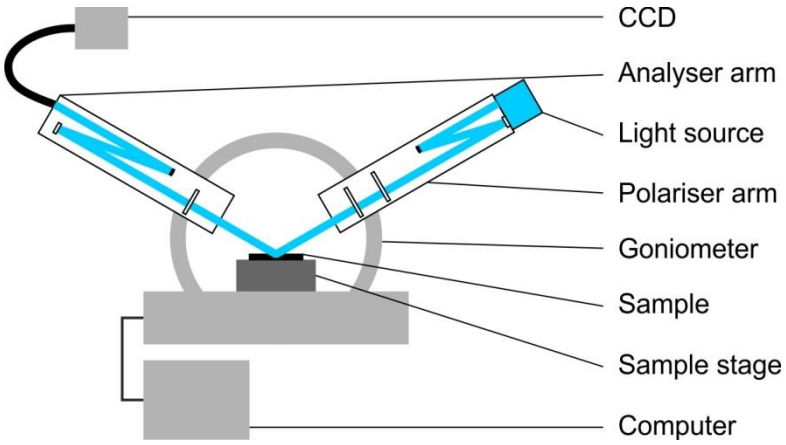

Fig. 3.9. Schematic representation of spectroscopic ellipsometer measurement in reflection mode. The polariser arm houses not only the polariser, but also the compensator.

Modelling of ellipsometric parameters

In order to resolve the thickness of thin films, the refractive index and extinction coefficient, dielectric constants, volume concentrations of materials and

other parameters, modelling of ellipsometric data must be performed. For this, the optical model of the investigated sample was created in *Spectroscopic Ellipsometry Analyzer v1.3.8* (*SEA, Semilab*) software, and the parameters of this model were changed during the fitting procedure until the response from the model matched the experimental results. The nanocomposite layer was described by effective medium approximation (EMA). Silver or copper in this layer was described by using a built-in refractive index database (the so-called *n*&*k* files), while DLC dispersion curves were not in the database. Thus, DLC was described by the dispersion law from several ones available in the software. The model was based on already known parameters so that to reduce the amount of fittable values. The thickness was used from TEM, X-ray reflectivity or quartz microbalance data from the film deposition system with some added degree of freedom. It was assumed that volume concentration is related to atomic concentration from EDS measurement, and this value (with some degree of freedom) was used to create an optical model. Current DLC:Cu model was heavily based on the X-ray reflectivity model used to interpret the same samples.

The Cody-Lorentz dispersion law was employed to describe the optical dispersion of DLC [144] because it proved to be the best from the available ones in the software after several attempts with other dispersion laws based on the determination coefficient (R^2) and root mean square error (RMSE) values. The Cody-Lorentz dispersion law is described as [145]:

$$\varepsilon_2 = \begin{cases} \dfrac{E_1}{E}\exp\left(\dfrac{E-E_\mathrm{t}}{E_\mathrm{u}}\right), & 0 \le E \le E_\mathrm{t} \\ G(E)\dfrac{AE_0\Gamma E}{(E^2-E_0^2)^2+\Gamma^2E^2}, & E > E_\mathrm{t} \end{cases} \tag{3.20}$$

$$G(E) = \frac{(E-E_\mathrm{g})^2}{(E-E_\mathrm{g})^2+E_\mathrm{p}^2}; \tag{3.21}$$

$$E_1 = E_\mathrm{t}L(E_\mathrm{t}). \tag{3.22}$$

Cody-Lorentz dispersion law parameters are described as follows: A – the oscillator amplitude (eV), E_0 – the oscillator peak position (eV), G – the broadening energy (eV), E_g – the band gap (eV), E_p – the transition energy (eV) that separates the absorption onset behaviour from the Lorentz oscillator behaviour, E_u – the slope of the Urbach tail (eV), E_t – the demarcation energy between Urbach tail transitions and the band-to-band transitions (eV). The real part of dielectric function ε_1 is calculated from the Kramers-Kronig relation.

The physical mixture of nanocomposite materials was described by *Bruggeman EMA* which is specifically used to describe embedded inclusions in an effective medium [146]:

$$P_n(\varepsilon_\mathrm{h} = \langle\varepsilon\rangle) = \sum_{j=0}^{n} p_j^{(n)}\langle\varepsilon\rangle^j = 0 \xrightarrow{selection} \langle\varepsilon\rangle, \tag{3.23}$$

$$\epsilon_i = \frac{1}{\gamma}\varepsilon_i, \tag{3.24}$$

$$\bar{c}_i = (\gamma + 1)c_i, \tag{3.25}$$

where ε_i and c_i are dielectric permittivity and concentration of the i^{th} species in the film. The coefficients of polynomes $p_j^{(n)}$ can be expressed quasi recursively by the concentrations and dielectric constants of the components. In case of a mixture of two materials, the coefficients are expressed as [147]:

$$p_0^{(2)} = -\gamma\epsilon_{12}, \tag{3.26}$$

$$p_1^{(2)} = \epsilon_1(1 - \bar{c}_1) + \epsilon_2(1 - \bar{c}_2), \tag{3.27}$$

$$p_2^{(2)} = 1. \tag{3.28}$$

The effective dielectric constant is then derived from the roots of complex coefficient polynomial equations by applying the quadratic formula.

In this study, the spectroscopic ellipsometry experimental data was best described by using the optical model with Bruggeman EMA for nanocomposite and Cody-Lorentz dispersion law for DLC. However, in literature, there is a wide variety of effective medium approximations and dispersion laws: Forouhi-Bloomer [56, 148], Bruggeman [149], Maxwell-Garnett [67, 150] EMAs, Forouhi and Bloomer parametrization [149], Gaussian [151, 152], single Lorentz oscillator [153], isotropic Cauchy with Urbach adsorption [154], Cody-Lorentz [67, 152], Drude-Lorentz [155], new amorphous [156], Tauc-Lorentz [152, 157, 158] dispersion laws, etc.

Prior to the fitting, the experimental spectra were smoothed by using the built-in spline function, and the range was reduced to 300–900 nm due to the increased noise in the deep UV. For the fitting, a simulated annealing algorithm [147, 159] was employed.

In multilayered models, the obtained parameters describe each layer separately, thus, the effective refractive index n_{eff}, the effective extinction coefficient k_{eff}, and the effective metal volume concentration C_{eff} of the whole film were calculated:

$$n_{\text{eff}} = \sum \frac{d_i n_i(\lambda)}{d_{\text{total}}}, \tag{3.29}$$

$$k_{\text{eff}} = \sum \frac{d_i k_i(\lambda)}{d_{\text{total}}}, \tag{3.30}$$

$$C_{\text{eff}} = \sum \frac{d_i C_i}{d_{\text{total}}}, \tag{3.31}$$

where d is the thickness of the i^{th} layer or the total thickness of the film (nm), C_i is the metal volume concentration in the i^{th} layer. Similarly, the effective dielectric functions are calculated. The effective refractive index and the extinction coefficient are derived from the optical path, while the effective volume concentration is derived from arbitrary volumes.

The extinction coefficient k obtained during fitting can be used to find absorption coefficient α (nm^{-1}) [57]:

$$\alpha = \frac{4\pi k}{\lambda}. \tag{3.32}$$

The goodness of fit of the optical model to the experimental data is described by two parameters: RMSE and R^2 [147]:

$$\mathrm{RMSE} = \sqrt{\frac{1}{2N-m}\sum_{i=1}^{N}\left(\left(\frac{f_{\mathrm{m1}}^{i}-f_{\mathrm{c1}}^{i}}{\sigma_{\mathrm{m1}}^{i}}\right)^{2}w_1+\left(\frac{f_{\mathrm{m2}}^{i}-f_{\mathrm{c2}}^{i}}{\sigma_{\mathrm{m2}}^{i}}\right)^{2}w_2\right)}, \quad (3.33)$$

$$\mathrm{R}^2 = 1-\frac{1}{2}\frac{S_{\mathrm{r1}}}{S_{\mathrm{t1}}}-\frac{1}{2}\frac{S_{\mathrm{r2}}}{S_{\mathrm{t2}}}, \quad (3.34)$$

where N is the number of data points in the experimental spectrum, m is the number of data points in the modelled spectrum, f_{m} and f_{c} are measured and modelled (calculated) ellipsometric functions, respectively, σ is the experimental error, and w is the weight factor. The S parameters are calculated as:

$$S_{\mathrm{r1}} = \sum_{i=1}^{N}\left(\frac{f_{\mathrm{m1}}^{i}-f_{\mathrm{c1}}^{i}}{\sigma_{\mathrm{m1}}^{i}}\right)^{2}w_1, \quad (3.35)$$

$$S_{\mathrm{r2}} = \sum_{i=1}^{N}\left(\frac{f_{\mathrm{m2}}^{i}-f_{\mathrm{c2}}^{i}}{\sigma_{\mathrm{m2}}^{i}}\right)^{2}w_2, \quad (3.36)$$

$$S_{\mathrm{t1}} = \sum_{i=1}^{N}\left(\frac{f_{\mathrm{m1}}^{i}-\bar{f}_{\mathrm{m1}}}{\sigma_{\mathrm{m1}}^{i}}\right)^{2}w_1, \quad (3.37)$$

$$S_{\mathrm{r1}} = \sum_{i=1}^{N}\left(\frac{f_{\mathrm{m2}}^{i}-\bar{f}_{\mathrm{m2}}}{\sigma_{\mathrm{m2}}^{i}}\right)^{2}w_2. \quad (3.38)$$

The better the fit, the closer to 1 is the R^2 value and RMSE is closer to 0.

Ellipsometric mapping

The applied intensive electromagnetic fields, e.g., laser irradiation, can change the optical properties of the materials. In order to investigate this effect, spectroscopic ellipsometry mapping was employed. Coordinates of 9898 points (101 × 98 points area) on the sample surface were imported into the measurement software. At every 100 points, the focusing procedure was repeated to maintain the highest intensity of the reflected light. The step between the points in both x and y directions was 30 μm, and the microspot mode was used. The total mapped area was around 3×3 mm^2. The beam size is bigger than the selected step, but it was reasoned that the signal would be integrated over the area, and lesser differences in signal values around the laser irradiated features would be visible. The measurements were taken at a 75° angle of incidence since it demonstrated the least noise.

Laser irradiation using various parameters has a varied impact on the ellipsometric parameters, and it was expected to see contrast variations in the map. This contrast is changing with the wavelength. After acquiring all the data, it was filtered: the spectra values at each wavelength were subtracted from each other, and the wavelength with the highest absolute difference value (i.e., the highest contrast) was chosen for the mapping. The procedure was repeated for both SE parameters, Ψ and Δ, since they might be differently sensitive to the changes of the sample surface and the optical properties.

3.2.4. *X-ray reflectivity technique*

X-ray reflectivity (XRR) is a nondestructive technique requiring fitting of the model to the acquired experimental data so that to determine the thickness and electron density of the materials [160]. The principle of XRR (Fig. 3.10) is based on the interference of X-ray beams reflected from the sample surface and from the interface between the layers [161].

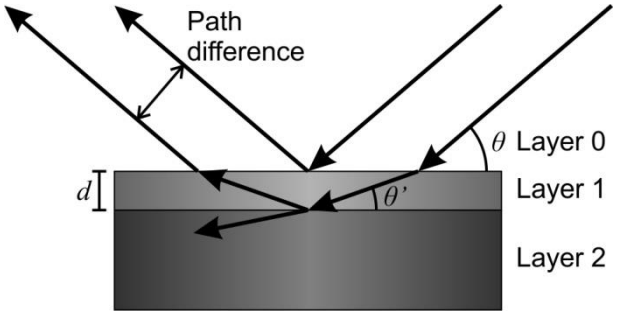

Fig. 3.10. A principal scheme of X-ray beam interaction with the sample during XRR measurements. Adapted from [161].

The XRR measurements for DLC:Cu samples were performed by using a *D8 Discover* diffractometer (*Bruker*) with a copper K_α X-ray source (λ = 0.154 nm). The employed geometry was a parallel beam 60 mm Göbel mirror. The X-ray generator used 40 kV and 40 mA voltage and current, respectively. The 2Theta-Omega scanning range was from 0° to 5° with a step of 0.0025° and 0.1 s time per step. The fitting was performed by using *DIFFRAC.Leptos* (*Bruker*) software. The model had 10 layers (as determined from TEM) with variable thickness, electron density, and roughness. From the results of separate layers, the effective density ρ_{eff} (g/cm^3) of the whole DLC:Cu thin film was calculated as:

$$\rho_{\text{eff}} = \sum \frac{d_i}{d_{\text{total}}} \rho_i, \tag{3.39}$$

where d_i and d_{total} are the thickness of the i^{th} layer and the total thickness of the film (nm), respectively, ρ_i is the density of the i^{th} layer (g/cm^3).

3.2.5. *Two-photon luminescence*

Two-photon luminescence (TPL) is caused by interband transitions of electrons in metal (Fig. 3.11a), which allows to study the near-field of nanostructures [162]. The TPL process is nonlinear: two low energy photons are absorbed by a molecule or an atom, and one higher energy photon is consequently emitted [163]. The TPL technique can also give clues about the oxidation state of silver nanoparticles. However, the TPL signal originates inside nanoparticles, thus, the 1–2 nm of the oxide layer does not significantly change the TPL signal [40]. TPL was used for the investigation of DLC:Ag samples after laser irradiation.

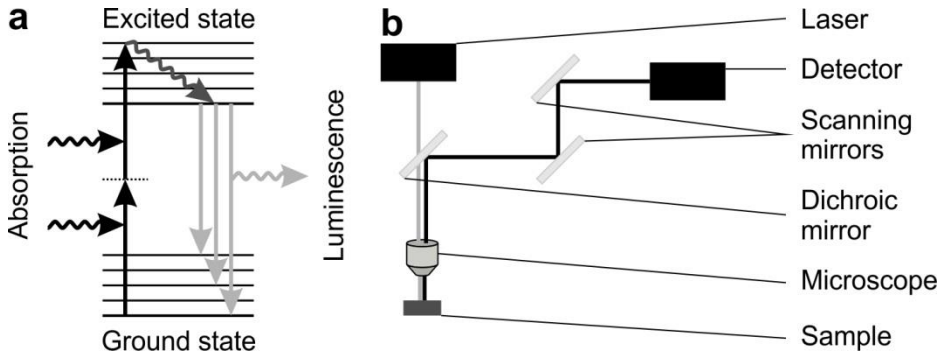

Fig. 3.11. (a) Electronic transitions in TPL process; (b) basic principal scheme of TPL system. Adapted from [163] and [164], respectively.

TPL measurements were performed on two different systems (the principal scheme depicted in Fig. 3.11b). One of them consists of a sub-100 fs, 795 nm wavelength, 75.5 MHz repetition rate titanium-sapphire laser (Tsunami, Spectra Physics), and an inverted scanning laser fluorescence microscope with a 100×, 0.65 numerical aperture objective [165]. The other equipment in use consists of a 200 fs, 730–860 nm wavelength, 80 MHz repetition rate titanium-sapphire laser and a scanning optical microscope with a 100×, 0.70 numerical aperture *Mitutoyo* infinity-corrected objective [40].

4. RESULTS AND DISCUSSION

4.1. Investigation of pristine thin films

4.1.1. *Diamond-like carbon and silver thin films*

In order to understand the properties of nanocomposites, their constituent materials have to be investigated first. The morphology of as deposited silver and DLC thin films is shown in Fig. 4.1. Both of the films are denoted by some roughness. Considering same scale micrographs (Fig. 4.1a for Ag and Fig. 4.1b for DLC), it appears that the roughness of the silver film is higher because it has bigger grains as evident from the contrast difference. Hydrogenated amorphous carbon usually is a very smooth thin film: its surface roughness is around 1 nm, and it depends mostly on the roughness of the substrate [54, 60, 166].

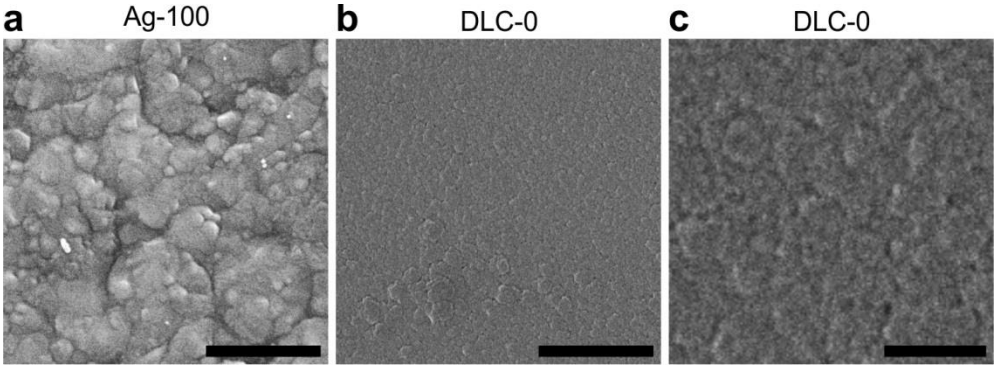

Fig. 4.1. Micrographs of pure materials as deposited on the silicon substrate: (a) SEM of Ag-100, mark size 500 nm, (b) HIM of DLC-0, mark size is 500 nm, (c) zoomed-in view of (b), mark size is 100 nm. Published in [A4].

Spectroscopic ellipsometry experimental curves together with the fitted ones (best fit) of the DLC samples are provided in Fig. 4.2. The dashed (fitted) curves match the solid (experimental) curves very well, and it can be concluded that the developed optical model (described in the Modelling of ellipsometric parameters chapter) is suitable to describe DLC.

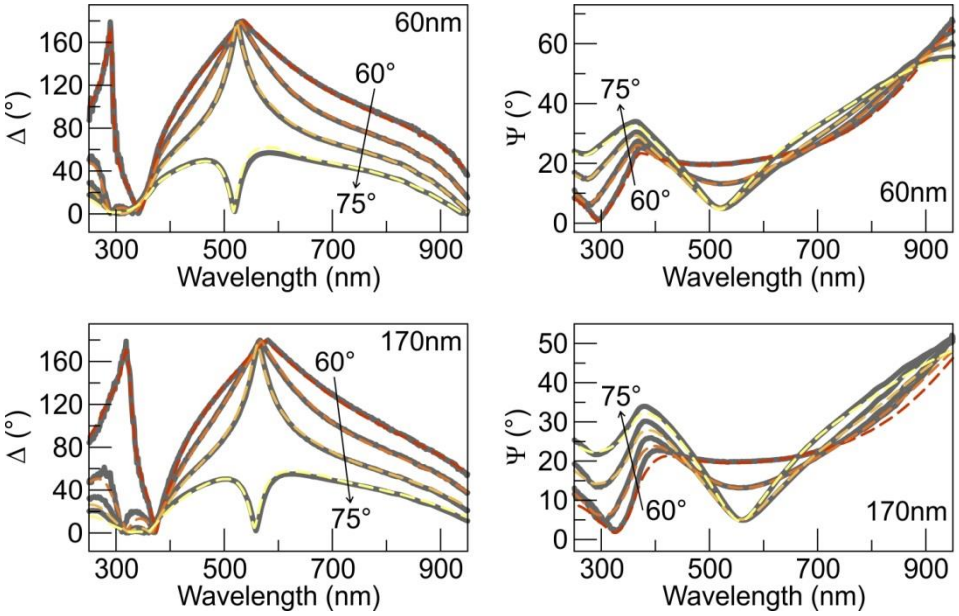

Fig. 4.2. Experimental (grey solid) and best fit (dashed) curves of ellipsometric parameters Δ and Ψ of 60 nm and 170 nm thicknesses DLC on silicon substrates. The arrow and the changing colours indicate the angle of incidence θ from 60° to 75° in steps of 5°. Presented in [B8, B10].

The goodness of fit, the thickness, and the refractive index at 632.8 nm wavelength obtained from SE measurements as well as the thickness from quartz microbalance for DLC samples are presented in Table 4.1. From R^2 and RMSE values, it can be concluded that the model (Cody-Lorentz dispersion law for the DLC layer) fits the data exceptionally well with $R^2 > 0.97$ and RMSE < 2.63. By comparing the thickness values from different techniques, it can be seen that DLC tends to have much lower thicknesses according to the quartz microbalance.

Table 4.1. Spectroscopic ellipsometry fitting results for DLC samples: R^2 is the determination coefficient, RMSE is the root mean square error, d_{SE} is the thickness from SE, d_Q is the thickness from quartz microbalance, n is the refractive index of the film at 632.8 nm wavelength. The values are averages obtained from multiple measurements with standard deviations.

Sample	R^2	RMSE	d_{SE} (nm)	d_Q (nm)	n
DLC-0	0.99 ± 0.01	2.26 ± 0.34	193.2 ± 29.0	60	1.70 ± 0.04
DLC-0’	0.97 ± 0.04	2.63 ± 0.60	220.6 ± 68.7	170	1.74 ± 0.11

The dielectric functions obtained from SE fittings for DLC samples are summarized in Fig. 4.3. By comparing the dielectric functions of a 60 nm thick DLC sample and a 170 nm thick DLC sample, it can be seen that the functions are very similar, thus the slight variations of the supply power during the deposition did not affect the optical properties of DLC films. It also means that the selected optical

model for fitting is good to describe DLC because the optical properties do not change dramatically with the change in thickness (considering it as a bulk material).

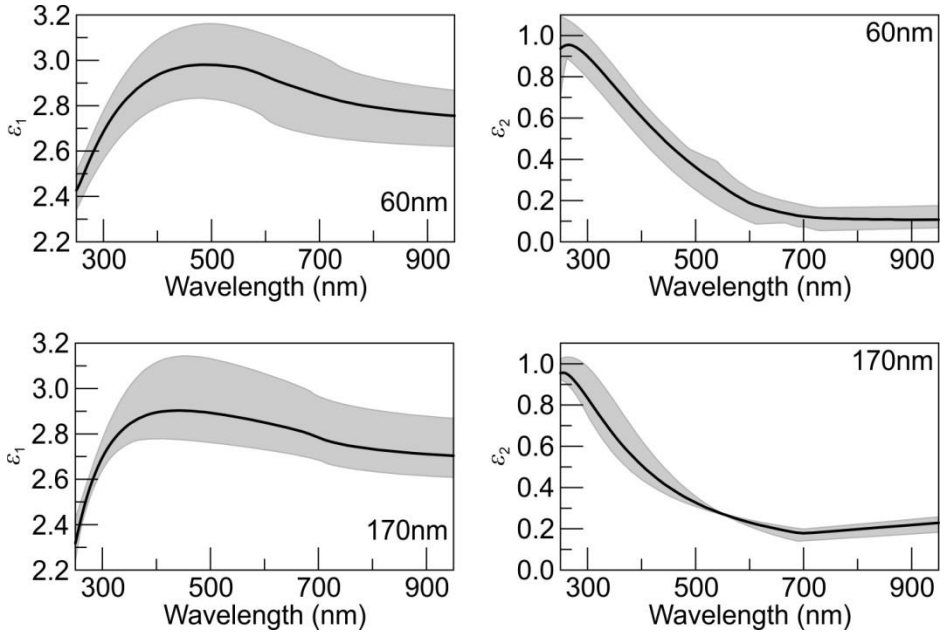

Fig. 4.3. Real (ε_1) and imaginary (ε_2) parts of dielectric function of DLC. The black line is the average value obtained after fitting all the measured spots on a sample. The grey shaded area represents the lowest and highest values from fitting.

4.1.2. *Diamond-like carbon with copper nanoparticles nanocomposites*

From EDS measurements it was determined that copper atomic concentration in DLC:Cu films was between 13.6 at.% and 48.8 at.%. The complete EDS analysis results are provided in Table 4.2. Since the DLC samples were deposited from a C_2H_2 precursor, it is expected that there should be anywhere between 20 at.% and 50 at.% hydrogen present in the film [54, 55]. However, the available elemental analysis method – EDS – is not capable to detect hydrogen, and thus the elemental composition is presented in a percentage of the detected elements.

Table 4.2. Elemental composition of DLC:Cu thin films as obtained from EDS analysis.

Sample	Carbon (at.%)	Oxygen (at.%)	Copper (at.%)
DLC:Cu-14	81.0	5.4	13.6
DLC:Cu-27	66.2	6.4	27.4
DLC:Cu-33	59.3	8.0	32.7
DLC:Cu-44	46.5	9.7	43.8
DLC:Cu-49	44.1	7.1	48.8

4.1.2.1. *Microscopy and X-ray reflectivity analysis results*

A distribution of the nanoparticle diameter in DLC:Cu is depicted in Fig. 4.4. Here, the central diameter (x_c of lognormal distribution as obtained from Equation

(3.5)) is marked as a dot. The central diameter of this specific sample (62.0 at.% copper) is 11 nm. The value is not at the peak of lognormal distribution, but rather it is shifted to the higher nanoparticle diameter due to the skewed nature of the function and its long tail.

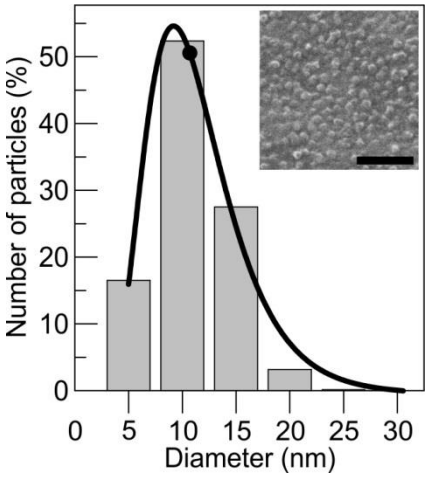

Fig. 4.4. Representative unimodal distribution of copper nanoparticles in DLC:Cu (62.0 at.% Cu) nanocomposite thin film with lognormal fit ($R^2 = 0.99$). The dot marks the central diameter x_c. The inset shows the HIM micrograph of the sample tilted at 20° with a mark size of 100 nm. Published in [A3].

The thicknesses of the DLC:Cu samples were determined from TEM micrographs (Fig. 4.5): 64.7 nm (DLC:Cu-14), 48.2 nm (DLC:Cu-27), 33.4 nm (DLC:Cu-33), 30.4 nm (DLC:Cu-44), and 40.5 nm (DLC:Cu-49). The micrographs also revealed the multilayered nature of the thin films, which helped to create XRR and SE models. From the TEM micrographs, it was determined that copper nanoparticles in DLC:Cu are of 2–6 nm diameter. DLC:Cu-14 and DLC:Cu-27 manifest fairly uniform distribution of copper nanoparticles. DLC:Cu nanocomposites with a higher copper content (DLC:Cu-33, DLC:Cu-44) are distinguished by the larger diameter of the particles and the higher electron density contrast. This is consistent with the separately investigated DLC:Cu sample with 62.0 at.% copper (Fig. 4.4): since this additional sample is denoted by a higher concentration than any other sample under consideration, it is expected for it to have a larger average particle diameter (in this case, 11 nm). In addition, these thin films have some fragments of DLC in-between the nanoparticles as structural layering (the brighter lines in Fig. 4.5). It shows variations in the film density and copper concentration within the depth of the thin DLC:Cu nanocomposite film. This indicates a self-organization of alternating DLC and Cu layers, which was also reported in [45]. It could be explained by segregation, metal catalytic actions, diffusion, etc., but the origin is still not fully understood.

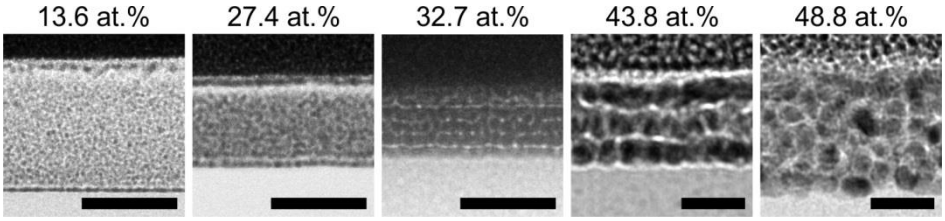

Fig. 4.5. TEM micrographs of the cross-sections of DLC:Cu samples. The mark size for 13.6–32.7 at.% is 50 nm, while for 43.8–48.8 at.%, it is 20 nm. Published in [A1].

According to XRR measurements (Fig. 4.6, the fitting described in the X-ray reflectivity technique chapter), the thickness of nanocomposites was: 51.2 nm (DLC:Cu-14), 43.8 nm (DLC:Cu-27), 24.4 nm (DLC:Cu-33), 25.4 nm (DLC:Cu-44), and 36.4 nm (DLC:Cu-49). The roughness of the surface was approximately 2 nm. The final 10-layer model of DLC:Cu nanocomposite samples revealed low density layers, which is in agreement with the bright regions in TEM micrographs (Fig. 4.5). The effective density of thin films, as calculated from Equation (3.39), was revealed to increase with the increasing copper content. This is expected as copper features a higher density than DLC. The density of DLC ρ_{DLC} (g/cm^3) was calculated when knowing the effective density of the whole film ρ_{eff} from XRR and the copper weight concentration C_{Cu} (in percentage) from EDS:

$$\rho_{\mathrm{DLC}} = \frac{\rho_{\mathrm{Cu}}\rho_{\mathrm{eff}}(100 - C_{\mathrm{Cu}})}{100\rho_{\mathrm{Cu}} - C_{\mathrm{Cu}}\rho_{\mathrm{eff}}}. \tag{4.1}$$

The density of copper ρ_{Cu} was assumed to be lower (7.184 g/cm^3) than bulk copper due to possible oxidation originating from the deposition process. The calculated density of DLC is: 1.722 g/cm^3 (DLC:Cu-14), 1.653 g/cm^3 (DLC:Cu-27), 1.537 g/cm^3 (DLC:Cu-33), 1.503 g/cm^3 (DLC:Cu-44), and 1.427 g/cm^3 (DLC:Cu-49).

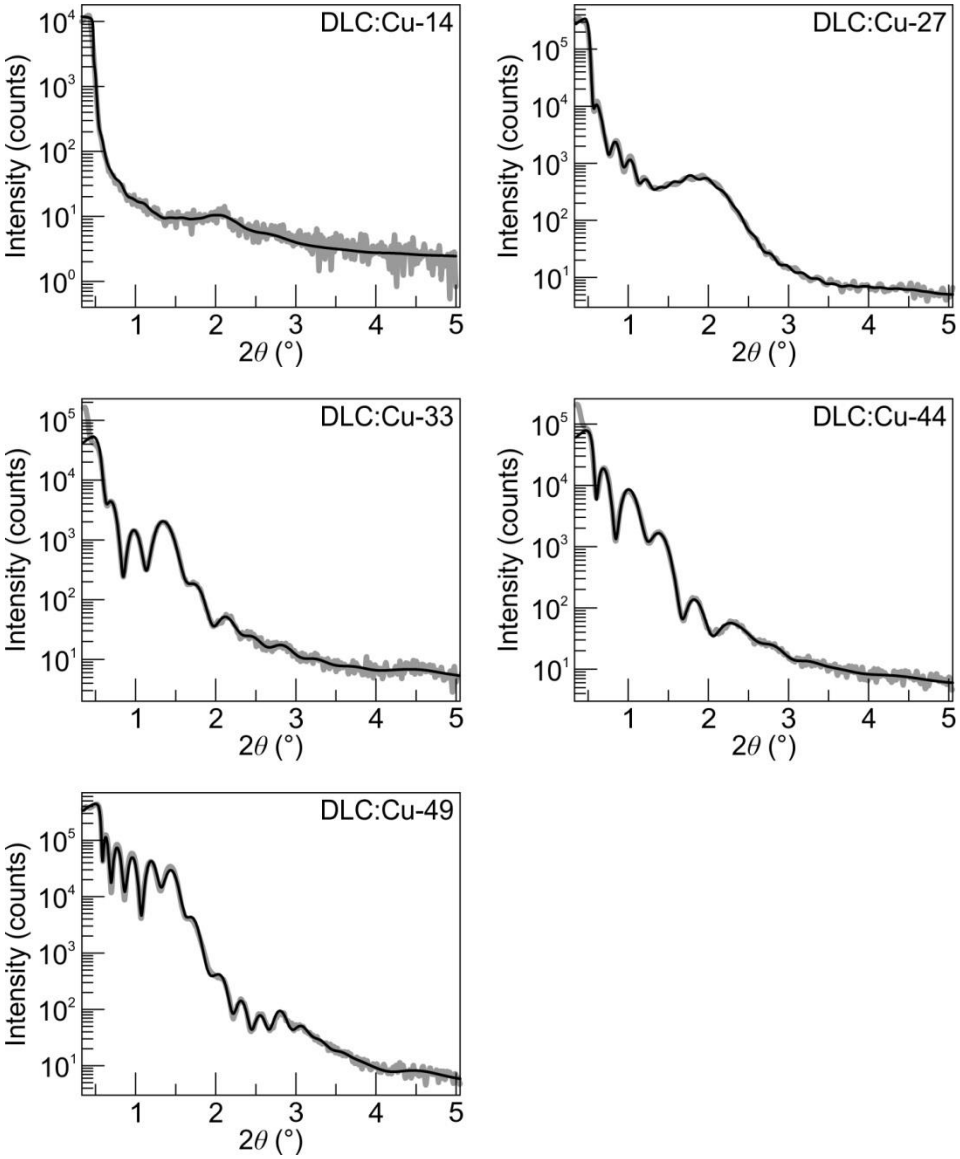

Fig. 4.6. XRR measurement (grey) and fitting (black) curves of DLC:Cu samples ($R^2 \geq 0.98$). Published in [A1].

4.1.2.2. *Raman spectroscopy results*

The obtained Raman scattering spectra of DLC:Cu thin films with peaks fitted by using Equation (3.8) are depicted in Fig. 4.7. These spectra are not very different from DLC Raman scattering spectra: they have a G peak and a D peak as a shoulder. No other peaks can be distinguished. Thus, the copper concentration does not exert a sizable impact on the Raman scattering spectra. This was also confirmed by Meškinis *et al*. for various copper concentrations [32, 167].

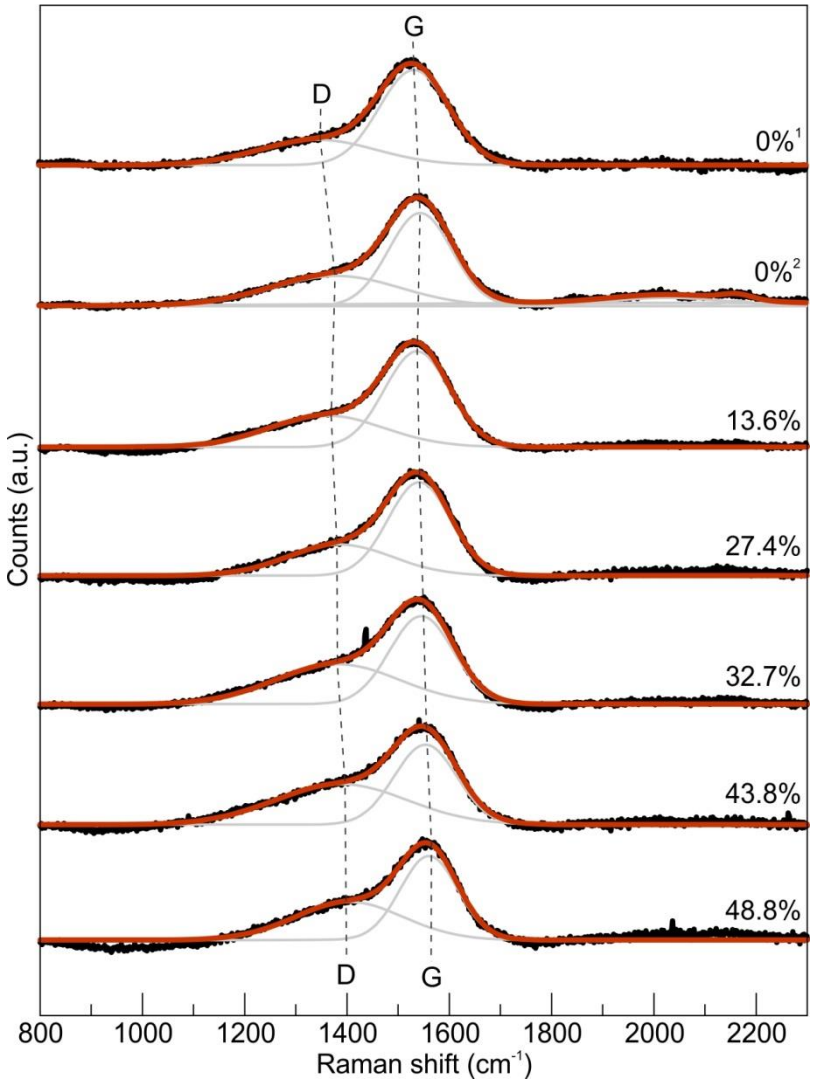

Fig. 4.7. Raman scattering spectra of DLC and DLC:Cu samples ($R^2 \geq 0.97$). The percentages indicate copper atomic concentration in the sample. [1]DLC-0, [2]DLC-0'.

4.1.2.3. *Optical spectroscopy results*

The normalized absorbance spectra of DLC:Cu samples are depicted in Fig. 4.8. The measured wavelength range of DLC:Cu and DLC is different due to the different spectrometers used for measurements. All the DLC:Cu samples, except for DLC:Cu-14 (denoted as 13.6% in Fig. 4.8), exhibit absorbance peaks: at 610 nm (DLC:Cu-27), 641 nm (DLC:Cu-33), 640 nm (DLC:Cu-44), and at 632 nm (DLC:Cu-49). Small differences in the absorbance peak positions indicate similar sizes of the nanoparticles in the DLC:Cu samples. It was previously reported that LSPR is possible for films with more than 10 at.% copper and particles bigger than 2 nm [168, 169], which is consistent with the current findings. Smaller particles lack

conduction electrons, and the surface charge density is reduced, which dampens and broadens LSPR.

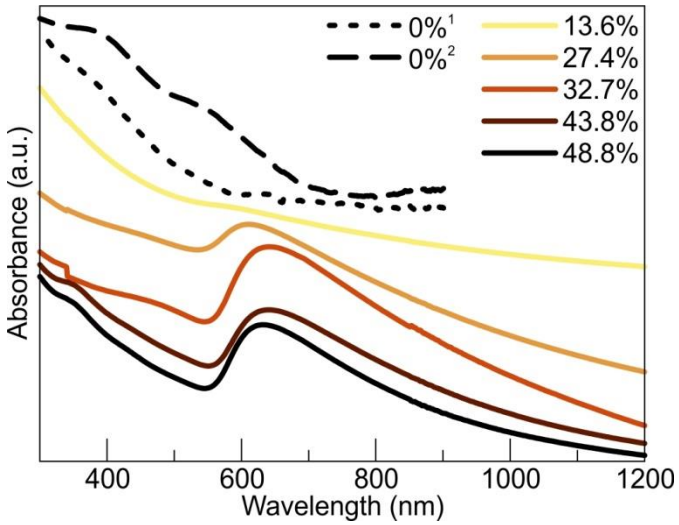

Fig. 4.8. Normalised and shifted for clarity optical absorbance spectra of DLC:Cu and DLC samples. The legend indicates copper atomic content in the sample. Here, the dashed lines are pure DLC ([1]DLC-0, [2]DLC-0'), and the solid lines are DLC:Cu (the colour darkens with the increasing copper concentration). Published in [A1].

4.1.2.4. *Spectroscopic ellipsometry results*

Spectroscopic ellipsometry experimental curves together with the fitted ones (best fit) of DLC:Cu samples are provided in Fig. 4.9 (Δ) and Fig. 4.10 (Ψ). The dashed (fitted) curves match the solid (experimental) curves very well, and it can be concluded that the created optical model (described in the Modelling of ellipsometric parameters chapter) is suitable to describe DLC:Cu. When comparing the DLC:Cu absorbance spectra (Fig. 4.8) and their ellipsometry spectra (Fig. 4.10) at a 75° incidence angle, it can be noted that they share a peak at just above 600 nm.

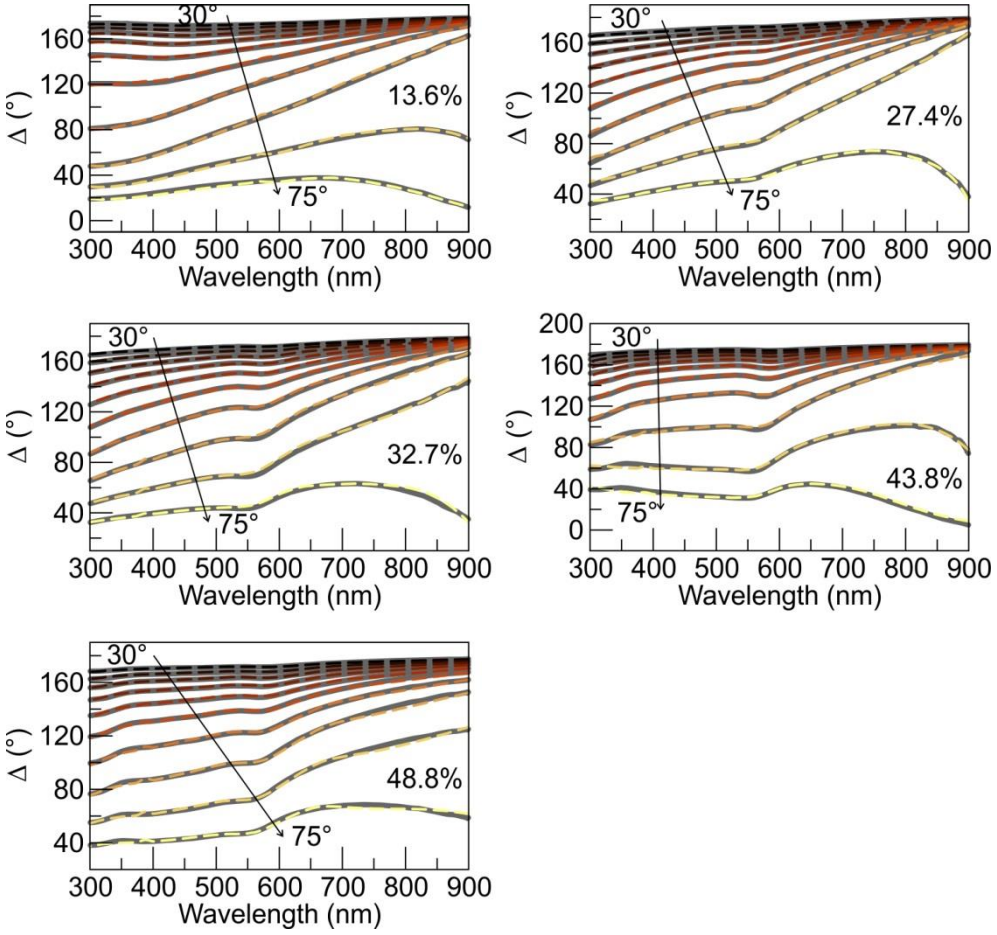

Fig. 4.9. Experimental (grey solid) and best fit (dashed) curves of ellipsometric parameter Δ of DLC:Cu samples on the quartz substrate. Percentage indicates the atomic concentration of copper in the samples. The arrow and the changing colours indicate the angle of incidence θ from 30° to 75° in steps of 5°. Published in [A1].

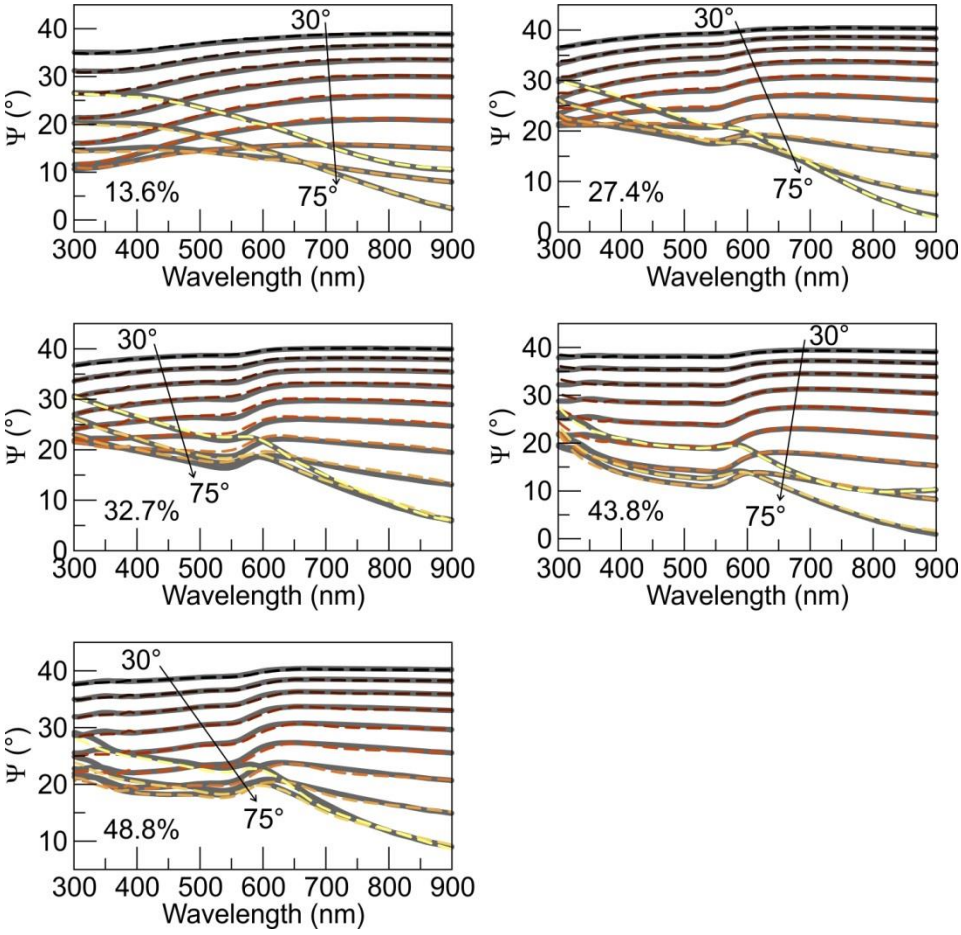

Fig. 4.10. Experimental (grey solid) and best fit (dashed) curves of ellipsometric parameter Ψ of DLC:Cu samples on the quartz substrate. Percentage indicates the atomic concentration of copper in the samples. The arrow and the changing colours indicate the angle of incidence θ from 30° to 75° in steps of 5°. Published in [A1].

The goodness of fit, the total thickness, the effective metal volume concentration, and the effective refractive index at 632.8 nm wavelength obtained from SE measurements for DLC:Cu samples are presented in Table 4.3. From the R^2 and RMSE values, it can be seen that the 10-layer model (Cody-Lorentz dispersion law for DLC, Bruggeman EMA for the nanocomposite layer) fits the data exceptionally well for the DLC:Cu samples: $R^2 > 0.94$, RMSE < 0.96. The complete information about the employed DLC:Cu multilayered optical model for spectroscopic ellipsometry is given in Table 4.4.

Table 4.3. Spectroscopic ellipsometry fitting results for DLC:Cu samples: R^2 is the determination coefficient, RMSE is the root mean square error, *d* is the thickness, *C* is the metal volume concentration, n_{eff} is the effective refractive index of the whole nanocomposite film at 632.8 nm wavelength. The values are averages obtained from multiple measurements with standard deviations.

Sample	R^2	RMSE	*d* (nm)	*C* (V.%)	n_{eff}
DLC:Cu-14	0.98 ± 0.00	0.72 ± 0.05	50.7 ± 7.0	10 ± 2	1.87 ± 0.05
DLC:Cu-27	0.98 ± 0.01	0.53 ± 0.09	43.4 ± 1.1	16 ± 1	2.29 ± 0.15
DLC:Cu-33	0.94 ± 0.02	0.87 ± 0.09	32.3 ± 2.5	24 ± 3	2.04 ± 0.08
DLC:Cu-44	0.96 ± 0.02	0.96 ± 0.16	27.6 ± 2.2	25 ± 2	1.98 ± 0.18
DLC:Cu-49	0.98 ± 0.00	0.78 ± 0.07	34.1 ± 0.6	31 ± 7	1.81 ± 0.16

Table 4.4. Optical 10-layer model parameters of DLC:Cu thin film obtained by spectroscopic ellipsometry. Here, *d* is the thickness of the layer, *C* is either atomic (at.%) or volume (V.%) concentration of copper, *n* is the refractive index at 632.8 nm wavelength, ± denotes standard deviation of the parameter above it.

C (at.%)	Parameter	Layer No.									
		1	2	3	4	5	6	7	8	9	10
13.6	*d* (nm)	11.4	16.7	2.8	1.1	4.2	4.8	4.0	0.7	2.5	1.0
	±	5.2	2.6	2.1	0.3	0.2	0.6	2.4	0.3	0.1	0.1
	C (V.%)	16.9	9.2	4.3	10.8	10.5	9.9	4.7	2.4	1.8	20.6
	±	0.02	0.06	0.03	0.09	0.04	0.06	0.03	0.02	0.01	0.03
	n	2.35	1.72	2.17	2.30	1.82	1.64	1.41	1.63	1.55	1.80
	±	0.72	0.48	1.17	0.92	0.51	0.27	0.31	0.41	0.29	0.55
27.4	*d* (nm)	9.4	1.6	9.0	6.4	8.3	2.2	2.2	2.1	1.8	0.4
	±	0.6	0.4	0.5	0.6	0.1	0.1	0.1	0.1	0.1	0.1
	C (V.%)	21.0	7.3	16.9	15.9	16.6	9.6	15.6	3.0	15.3	32.9
	±	0.03	0.04	0.09	0.10	0.03	0.08	0.10	0.03	0.05	0.03
	n	3.03	3.03	2.59	1.83	1.87	1.91	1.51	1.60	2.15	2.46
	±	1.10	0.97	0.64	0.53	0.40	0.95	0.28	0.49	0.57	0.48
32.7	*d* (nm)	2.7	2.4	0.9	2.2	3.1	1.5	2.5	4.8	3.3	8.9
	±	0.1	0.1	0.1	0.2	0.1	1.0	0.9	1.3	0.3	1.8
	C (V.%)	56.4	21.3	6.8	68.1	13.2	2.8	63.1	1.9	52.7	2.6
	±	0.07	0.05	0.03	0.02	0.05	0.02	0.01	0.01	0.03	0.01
	n	3.18	2.03	2.60	2.32	2.25	1.98	2.72	1.74	1.61	1.57
	±	0.70	0.62	0.75	1.64	1.05	0.37	0.62	0.41	0.64	0.38
43.8	*d* (nm)	3.4	2.4	1.4	1.1	2.4	1.0	3.3	4.2	4.2	4.2
	±	0.4	0.1	0.1	0.2	1.1	0.5	0.2	0.7	0.7	2.0
	C (V.%)	43.7	8.0	38.3	4.5	11.0	26.7	30.0	3.9	70.7	4.8
	±	0.05	0.06	0.04	0.05	0.05	0.04	0.03	0.04	0.02	0.03
	n	2.31	2.36	1.83	2.48	1.92	2.35	1.71	1.46	2.25	1.42
	±	1.02	0.69	0.65	0.85	0.24	1.24	0.95	0.59	0.83	0.61
48.8	*d* (nm)	3.0	1.1	2.7	1.0	1.8	0.9	2.4	11.2	8.1	4.5
	±	2.2	0.2	0.3	1.1	1.7	0.6	0.4	0.5	0.8	0.7
	C (V.%)	65.3	59.6	19.1	79.9	12.5	94.3	24.3	28.5	14.3	34.0
	±	0.37	0.07	0.23	0.33	0.11	0.03	0.35	0.01	0.04	0.20
	n	2.12	2.55	2.89	1.03	2.13	0.32	2.27	1.75	1.37	1.84

	±	1.91	1.13	1.34	1.37	0.20	0.11	0.69	0.12	0.37	0.86

The thickness values of the nanocomposites as determined by various techniques are compared in Table 4.5. As it can be seen, the agreement between the TEM, XRR, and SE results is fairly good considering the standard deviations of the measured values. Since TEM is a most direct method to measure the film thickness, it should be considered as the actual thickness. The exceptional agreement of the SE results with TEM could be expected from a 10-layer model heavily based on XRR and TEM measurements since it involves more fittable parameters and, thus, more degrees of freedom. The most prominent disagreement in the thickness values are from quartz microbalance. DLC:Cu tends to feature much higher thicknesses according to quartz microbalance. However, quartz microbalance is a mass measurement technique, and the thickness is obtained non-directly, thus the differences are possible if the density variation from sample to sample is not taken into account. Other possible reasons for the differences in the results obtained by different techniques are the surface roughness and not fully described interfaces in the models.

Table 4.5. Comparison of DLC:Cu thickness obtained by various techniques: quartz microbalance during the deposition, transmission electron microscopy (TEM), X-ray reflectivity (XRR), and spectroscopic ellipsometry (SE).

Sample	Thickness (nm)			
	Quartz microbalance	TEM	XRR	SE[a]
DLC:Cu-14	100	64.7	51.2	50.7 ± 7.0
DLC:Cu-27	100	48.2	43.8	43.4 ± 1.1
DLC:Cu-33	100	33.4	24.4	32.3 ± 2.5
DLC:Cu-44	100	30.4	25.4	27.6 ± 2.2
DLC:Cu-49	100	40.5	36.4	34.1 ± 0.6

[a]Error value in spectroscopic ellipsometry results is standard deviation of the values obtained for the same sample at different spots.

The comparison of the copper content in DLC:Cu thin films within the depth obtained by different techniques is depicted in Fig. 4.11. The EDS data represents copper L_α line intensity. The XRR and SE data was obtained from the fitting when using 10-layer models. The copper volume concentration and the effective density of DLC:Cu thin films vary within the depth and are in good agreement with TEM EDS. Thus, the XRR and SE can be used for the initial investigation of the sample structure when destructive thickness profiling techniques are not desirable.

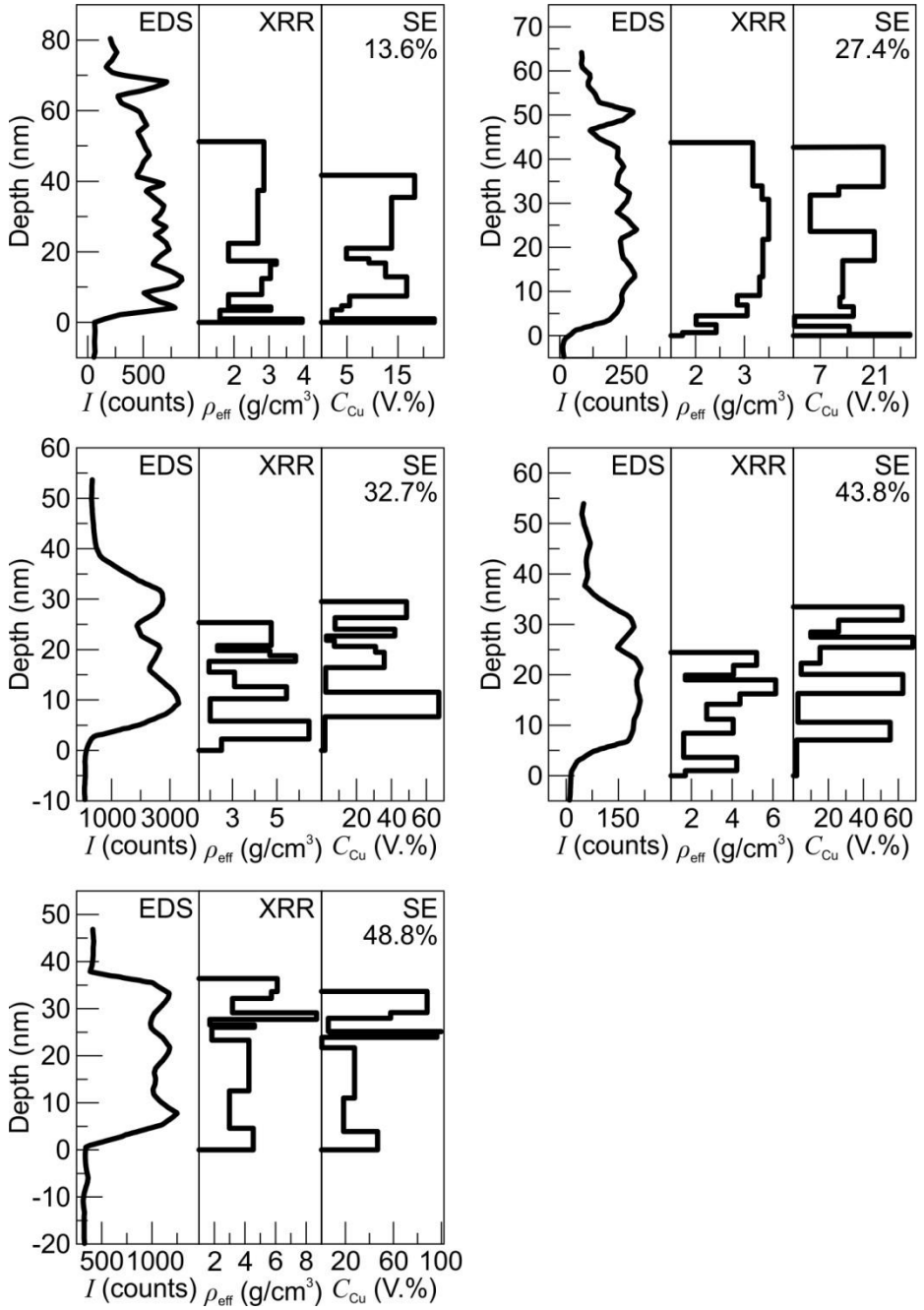

Fig. 4.11. Comparison of copper content depth profiles in DLC:Cu thin films obtained by EDS (intensity I of Cu L_α line), XRR (effective density ρ_{eff} of thin film), and SE (Cu volume concentration) techniques. DLC:Cu samples are indicated by their atomic Cu percentage. Published in [A1].

The dependence of the volume concentration and the effective refractive index on copper atomic concentration is depicted in Fig. 4.12. Copper volume concentration follows the linear trend depending on copper atomic concentration. To the contrary, the refractive index dependence in the DLC:Cu case does not follow a fully linear trend. At first, the refractive index is increasing with the increasing copper atomic concentration. At 27.4 at.% copper, the refractive index value is the highest, and it starts to decrease with the increasing copper concentration. Copper shows an absorption peak at around 600 nm, and LSPR is a possible explanation of the decreasing refractive index. Additionally, copper has a high extinction above the 500 nm wavelength, which results in a refractive index below 1.0, and, at the same time, the decreasing effective refractive index of DLC:Cu nanocomposite. The sample with the lowest copper content (DLC:Cu-14, 13.6 at.%) features a lower effective refractive index than the remaining DLC:Cu nanocomposites. It is consistent with the results of the absorbance spectra (see Fig. 4.8) where DLC:Cu-14 did not exhibit any absorbance peak.

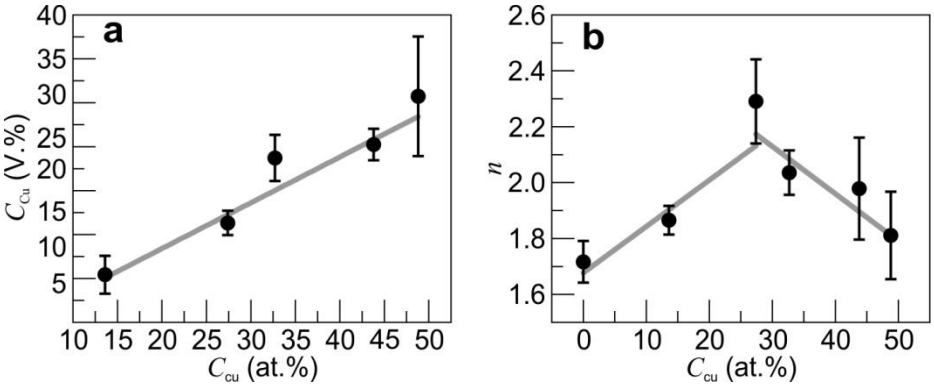

Fig. 4.12. Copper volume concentration (a) and refractive index of DLC:Cu at 632.8 nm wavelength (b) dependencies on atomic copper concentration. Dots are the average values obtained from SE fittings, and error bars are standard deviations. Grey lines are linear fits ($R^2 = 0.90$ and $R^2 \geq 0.65$, respectively). Published in [A1].

In plasmonic applications, a more important parameter than the refractive index is the dielectric function, and, thus, it was investigated more thoroughly. The dielectric functions obtained from the SE fittings for DLC:Cu are summarized in Fig. 4.13 (ε_1) and Fig. 4.14 (ε_2). DLC:Cu real parts of dielectric function agree with the absorbance spectra (Fig. 4.8) by having a dip above 600 nm. In the case of pure copper (Fig. 2.2), there is a peak at a similar wavelength in ε_1 and a dip in ε_2. As the extrema features of copper are preserved, the nanocomposites are still plasmonic. The values of the dielectric functions of DLC:Cu (Fig. 4.13, Fig. 4.14) are very different from pure copper (Fig. 2.2). The real part of the dielectric function no longer has a negative part, and, in most cases, it is very constant up to 600 nm, yet it slightly increases with the further increase of the wavelength. This is partly because the results are averaged throughout the sample, which might have some inconsistencies in the film. The imaginary part of the dielectric function exhibits

lower values in nanocomposites than in pure copper. This is advantageous because it indicates lower losses in the material.

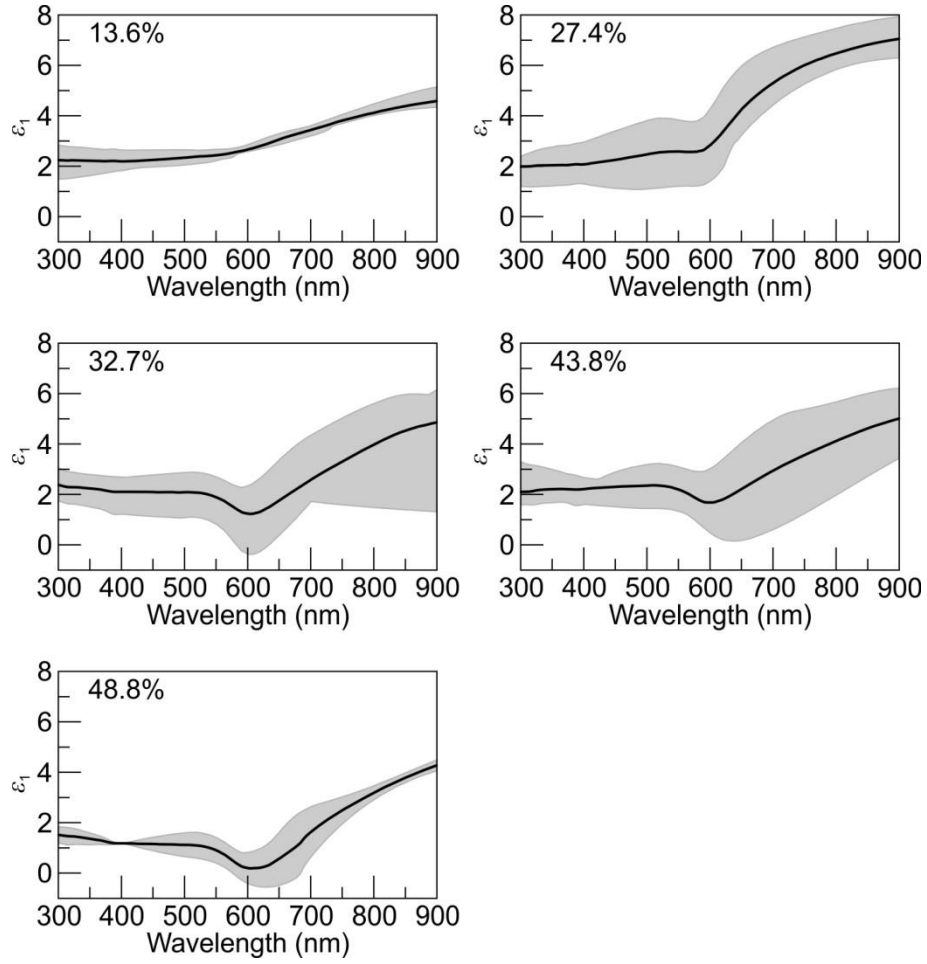

Fig. 4.13. Real part (ε_1) of dielectric function of DLC:Cu nanocomposite films. Black line is the average value obtained after fitting all the measured spots on a sample. Grey shaded area represents the lowest and highest values from fitting. Percentage is the atomic concentration of copper in the film.

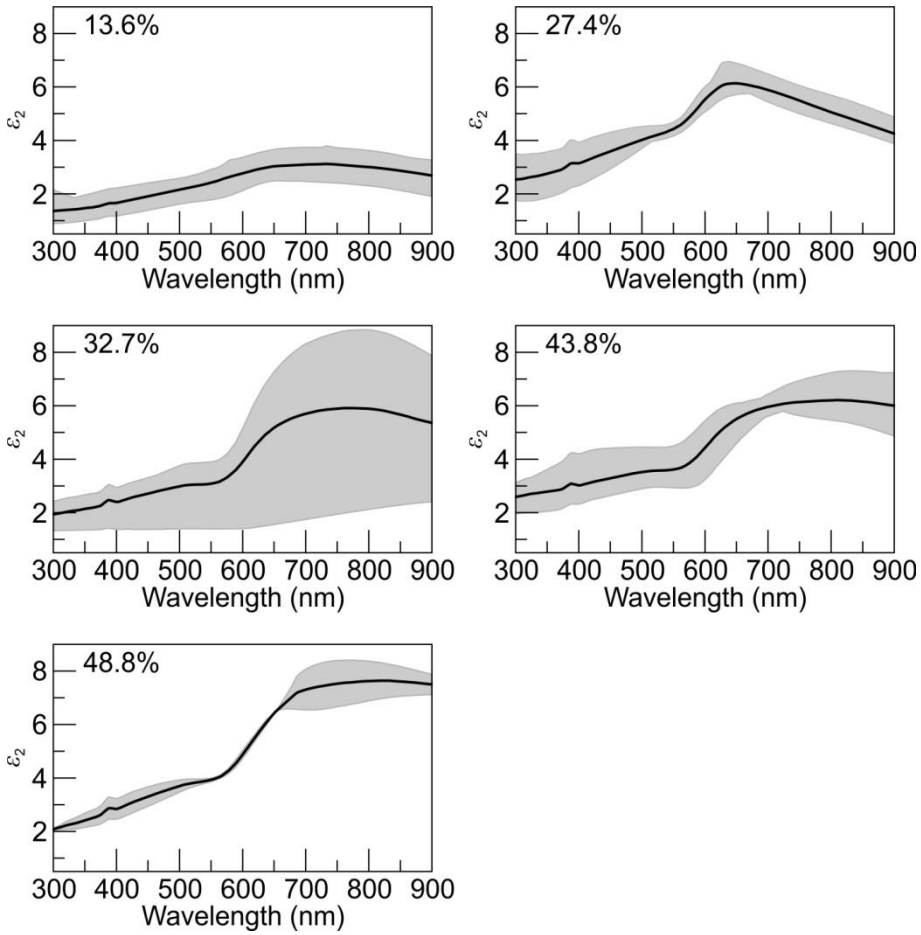

Fig. 4.14. Imaginary part (ε_2) of dielectric function of DLC:Cu nanocomposite films. Black line is the average value obtained after fitting all the measured spots on a sample. Grey shaded area represents the lowest and highest values from fitting. The percentage is the atomic concentration of copper in the film.

4.1.3. *Diamond-like carbon with silver nanoparticles nanocomposite films*

From the EDS measurements, it was determined that silver atomic concentration in DLC:Ag samples is between 2.0 at.% and 15.3 at.%. The overall chemical composition of the films determined by EDS is given in Table 4.6. As already mentioned in the case of DLC:Cu nanocomposites, it is expected that there should be some hydrogen present in the films, however, EDS is not capable to detect it.

Table 4.6. Elemental composition of DLC:Ag thin films as obtained from EDS analysis.

Sample	Carbon (at.%)	Oxygen (at.%)	Silver (at.%)
DLC:Ag-2	97.4	0.6	2.0
DLC:Ag-2’	95.4	2.3	2.3

DLC:Ag-6	89.5	4.5	6.0
DLC:Ag-7	81.3	12.2	6.5
DLC:Ag-8	76.6	15.5	7.9
DLC:Ag-14	71.4	14.5	14.1
DLC:Ag-14’	74.7	11.2	14.1
DLC:Ag-15	68.6	16.1	15.3

4.1.3.1. *Microscopy analysis results*

Morphology of as deposited DLC:Ag thin films is depicted in Fig. 4.15. DLC:Ag with 2.3 at.% of silver has visible nanoparticles only in the vicinity of surface defects. DLC:Ag with 2.0 at.% silver has surface features, but it is hard to distinguish whether it is a dense population of very small nanoparticles, or merely surface roughness. Other DLC:Ag samples with a higher silver content definitely have nanoparticles present with a variety of sizes and densities.

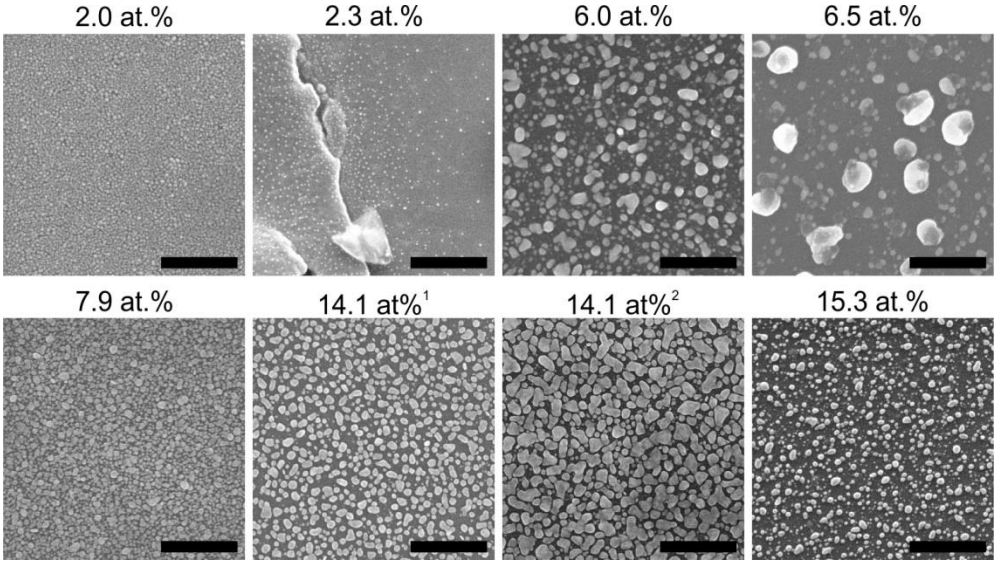

Fig. 4.15. SEM micrographs of as deposited DLC:Ag nanocomposite thin films of different silver concentrations on silicon substrate. Mark size is 500 nm. [1]DLC:Ag-14, [2]DLC:Ag-14’. Published in [A4], presented in [B2, B3, B5, B7, B9, B13].

The nanoparticles densities in pristine films as determined from SEM micrographs are as follows: 293 μm^{-2} (DLC:Ag-6), 244 μm^{-2} (DLC:Ag-7), 920 μm^{-2} (DLC:Ag-8), 336 μm^{-2} (DLC:Ag-14), 249 μm^{-2} (DLC:Ag-14’), and 601 μm^{-2} (DLC:Ag-15). Particle density and area fraction dependencies on atomic silver concentration are depicted in Fig. 4.16. These parameters are important for sensor application, since the response of a sensor depends on the area fraction [170]. Particle density and area fraction do not appear to follow a clear tendency in relation to silver concentration. It means that this could be more related to deposition parameters, which was extensively studied by Meškinis *et al*. [167, 171, 172]. Also, film thickness could play an important role here, since, for the thicker films, the metal can be distributed in the whole volume, which increases the atomic

concentration, but decreases the area fraction. It was reported that the surface area fraction depends on the particle size and can be varied by changing the duration of deposition [173, 174].

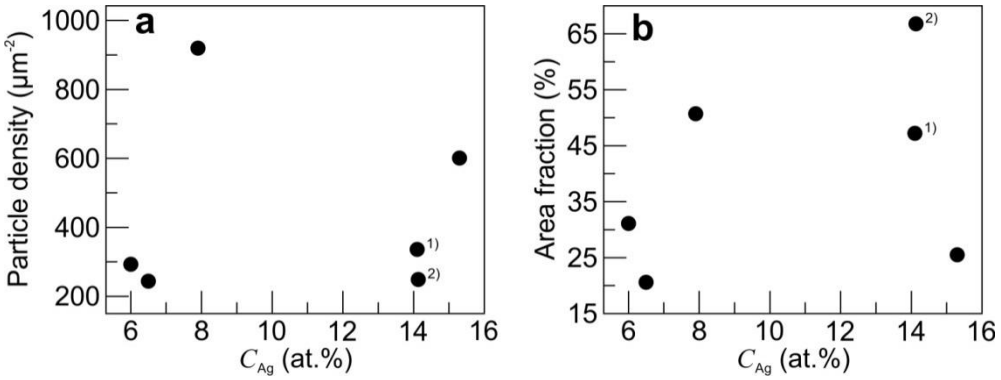

Fig. 4.16. Particle density (a) and particle area fraction (b) dependence on silver atomic concentration in DLC:Ag nanocomposites. [1)]DLC:Ag-14, [2)]DLC:Ag-14'.

Histograms of nanoparticle fractions of certain diameters and their lognormal fits, as obtained from Equation (3.5), are depicted in Fig. 4.17. Only sample DLC:Ag-14 has bimodal distribution, all the remaining samples have unimodal distributions. Sample DLC:Ag-7 has a sizable fraction of nanoparticles in the range of 15–35 nm, and this shoulder could be interpreted as a second peak in the distribution. However, the fraction of the smallest nanoparticles is so high that lognormal distribution can no longer be used to fit the data. Similarly, DLC:Ag-14' does not follow the lognormal trend because it has a large amount of the smallest nanoparticles, and the amount of the larger particles decreases exponentially. Interestingly, two samples with the same silver atomic concentration (14.1 at.%) have very different distributions of the particle size. However, the deposition parameters were different for these films, and the resulting carbon and oxygen concentrations are different. This means that the films actually grow differently, and that there might be variations of silver concentration within the depth of the film (e.g., DLC:Ag-14 might be more uniform, while DLC:Ag-14' could have more silver at the top than at the bottom of the film), whereas particle analysis takes into account only the particles which are visible at the surface. A thorough TEM analysis is necessary to draw particular conclusions.

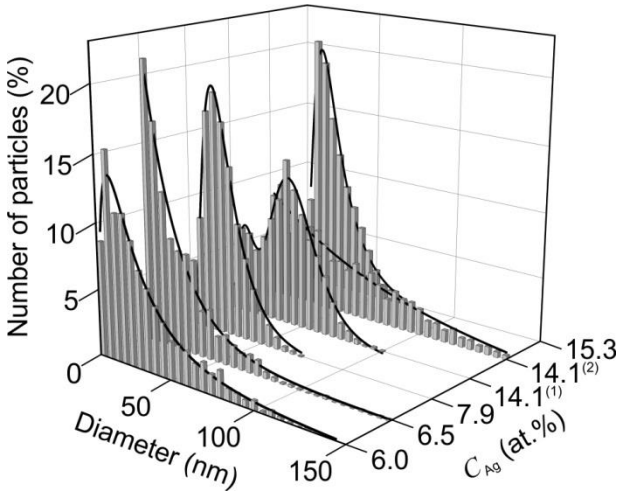

Fig. 4.17. Particle distributions by diameters in nanocomposite films with different silver atomic concentration and their lognormal fits ($R^2 \geq 0.96$). (1)DLC:Ag-14, (2)DLC:Ag-14'.

The central diameters of DLC:Ag nanocomposites with unimodal distributions are: 26 nm (DLC:Ag-6), 24 nm (DLC:Ag-8), 20 nm (DLC:Ag-15), and less than 5 nm (DLC:Ag-7, DLC:Ag-14'). In DLC:Ag-14 bimodal distribution, most of the particles are around 17 nm and 46 nm in diameter.

The cross-sectional views of DLC:Ag-2 and DLC:Ag-15 samples are shown in Fig. 4.18. In the case of DLC:Ag-2, in approximately 5 μm cross-section view, only 5 nanoparticles were discovered. This means that, in the SEM micrograph of the top view (Fig. 4.15), the visible features should be the surface roughness and not nanoparticles. To the contrary, in the TEM micrograph of the DLC:Ag-15 sample, many silver nanoparticles are visible. They appear to be more on the surface of the film than inside it. This was also observed for another sample, namely, for DLC:Ag-14', after investigating it at the tilted angle when using SEM (Fig. 4.19). The thickness of the DLC:Ag-2 thin nanocomposite film as determined from TEM is around 117.1 nm. The thickness of DLC:Ag-15 is either 26.8 nm (the continuous part of the film), or 74.8 nm (including the height of the biggest nanoparticles).

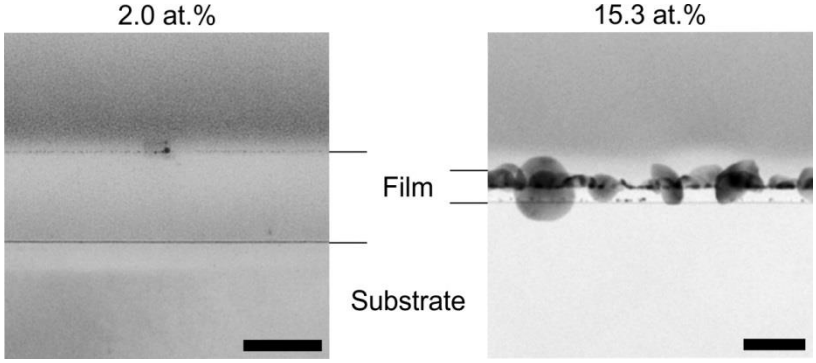

Fig. 4.18. TEM micrographs of the cross-sections of DLC:Ag samples. Mark size is 100 nm.

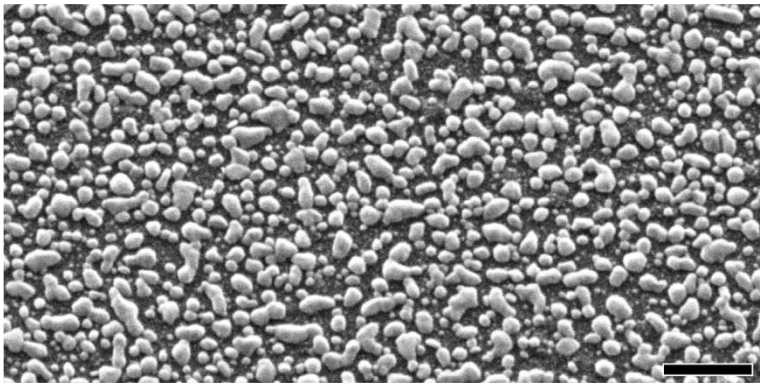

Fig. 4.19. SEM micrograph of DLC:Ag-14’ sample tilted at 30° angle. Mark size is 200 nm.

High-angle annular dark-field TEM imaging together with EDS was used to obtain the elemental distribution in the vicinity of silver nanoparticles in the DLC:Ag-2 and DLC:Ag-15 samples (Fig. 4.20). Silver nanoparticles appear white in these TEM images. In elemental analysis, the brighter colouring means a higher concentration of the corresponding element. Carbon is mostly uniformly distributed with a lower concentration at the places of nanoparticles. Oxygen is also abundant in the samples with a slightly increased concentration at the nanoparticles. This indicates oxidation of silver. Sulphur is mostly found at the nanoparticles, and it proves that not only oxidation, but also sulfurization could be a problem for nanocomposites containing silver, especially when nanoparticles form closer to the surface and are not fully protected by a matrix.

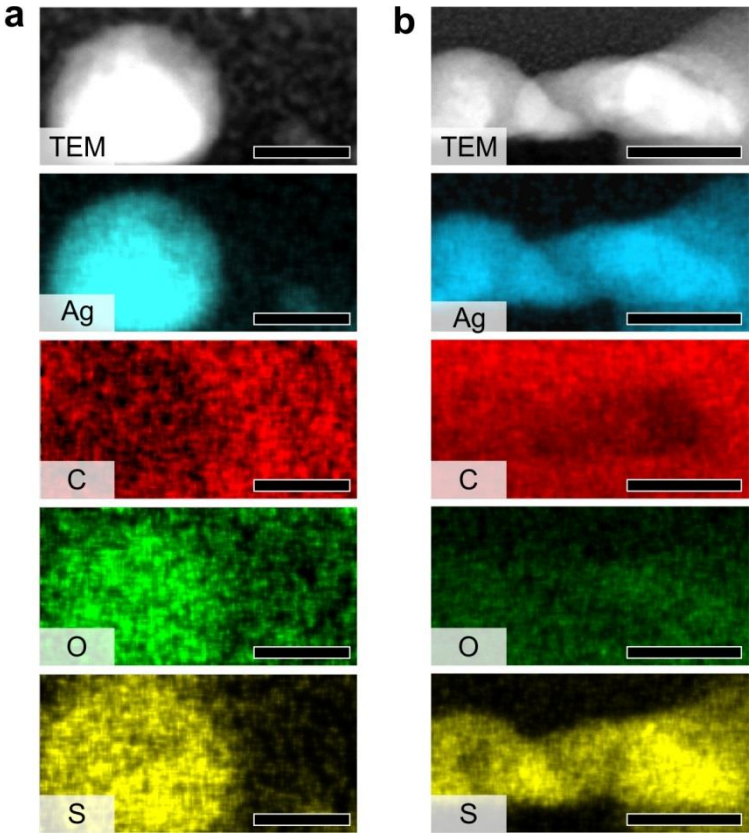

Fig. 4.20. TEM close-up of nanoparticles of DLC:Ag-2 (a) and DLC:Ag-15 (b) samples with EDS mapping of the same area of silver, carbon, oxygen, and sulphur elements. Mark sizes are 10 nm and 30 nm, respectively.

4.1.3.2. *Raman spectroscopy results*

The Raman spectroscopy results of DLC:Ag samples with peaks fitted by using Equation (3.8) are summarized in Fig. 4.21. The Raman scattering spectra of both DLC-0 samples (0%[1] and 0%[2] in Fig. 4.21) are consistent with amorphous hydrogenated diamond-like carbon (a-C:H) spectra reported elsewhere [119, 175–178]. The shoulder at 1400 cm^{-1} and the peak at 1535 cm^{-1} are called D and G peaks, respectively. Nanocomposite samples have better pronounced D peaks which get increased with the increasing silver content in the nanocomposite films. Starting from approximately 6.0–6.5 at.% of silver, the D peak no longer appears as a shoulder, but rather as a separate peak.

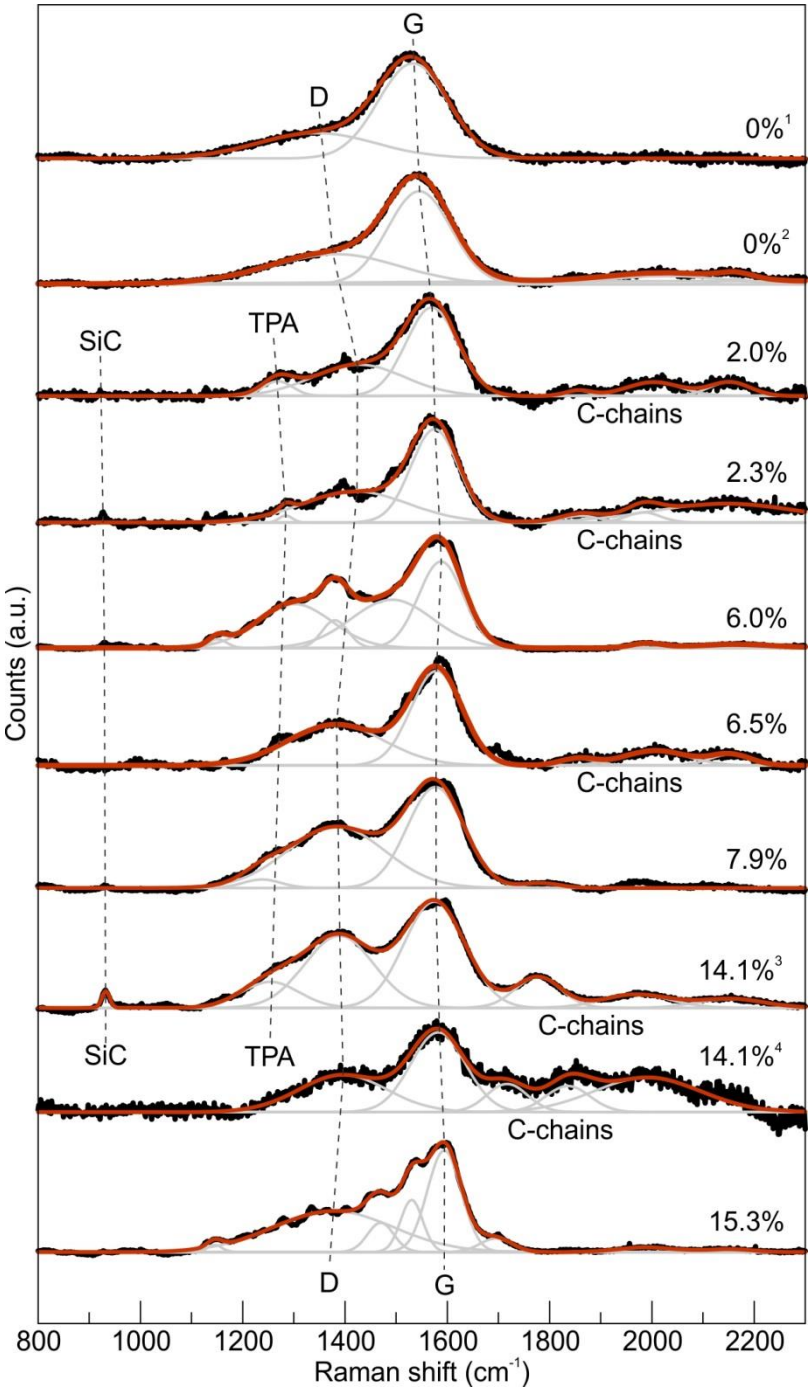

Fig. 4.21. Raman scattering spectra of DLC and DLC:Ag samples ($R^2 \geq 0.94$). The percentages indicate silver atomic concentration in the sample. [1]DLC-0, [2]DLC-0', [3]DLC:Ag-14, [4]DLC:Ag-14'. Published in [A4].

It was previously reported that a clear SERS effect can be obtained for nanocomposites with 11.3 at.% silver [119]. The findings of this study are consistent because the sample with 14.1 at.% silver (DLC:Ag-14) showed the most expressed Raman scattering spectrum peaks. However, the specific number for the enhancement factor could not be determined due to the differences in the intensity of Raman scattering spectra when investigating different spots on the same sample. Two of the samples (with 6.0 at.% and 15.3 at.%) have more complicated spectra, which is quite different from the rest of the samples. It could be the influence of the particle sizes and the distance between them on SERS, which was reported in [119]: The SERS signal increases with the increasing particle size and with the decreasing interparticle distance. In fact, the average nanoparticle diameters of samples DLC:Ag-6 and DLC:Ag-15 were among the biggest ones (Fig. 4.17). The interparticle distance was not measured for the samples, only area fractions were investigated (Fig. 4.16b), thus a full conclusion about the reason of the emerging additional peaks in Raman scattering spectra cannot be given yet. It could also be related to some contamination of the samples.

In addition to the increased D and G peaks, other peaks also emerge in the nanocomposite Raman spectra (Fig. 4.21). The peak at 932 cm^{-1} is commonly found in samples on quartz substrate and is related to SiC bond [179, 180]. This peak, although much smaller in comparison with other peaks in the spectrum, is present in the spectra of samples DLC:Ag-2, DLC:Ag-2', DLC:Ag-6, DLC:Ag-8, and DLC:Ag-14 (see Fig. 4.21). The peak intensity depends on the thickness of the film and the SERS effect. Without the SERS effect, the peak should increase with the decreased thickness of the thin film. The shoulder at 1245 cm^{-1} is known to increase with the increasing hydrogen content in the film and is related to transpolyacetylene (TPA) [58, 181, 182]. Smaller repetitive peaks above 1700 cm^{-1} are related to carbon chains of various lengths (C-chains) [183, 184].

4.1.3.3. *Optical spectroscopy results*

DLC-0, DLC:Ag-8 and DLC:Ag-14 samples on quartz substrate were measured in an integrating sphere with a trap in order to determine the diffused reflectance and the validity of Equation (3.11) usage so that to determine absorbance. The obtained spectra are depicted in Fig. 4.22. For all the three samples, the spectra are monotone, the reflectance increases towards longer wavelengths. DLC:Ag-14 demonstrated higher diffused reflectance than the two other tested samples, and also the increase of reflectance towards the longer wavelengths was more rapid. It can be assumed that, for samples with lower metal concentration, diffused reflection is negligible, and Equation (3.11) holds. Samples with a higher metal content might require taking diffuse reflection into account. Since only relative absorbance difference between the samples is important for further experiments, it was decided not to use different methods, but rather to normalize the absorbance spectra, thus making absorbance qualitative and not quantitative.

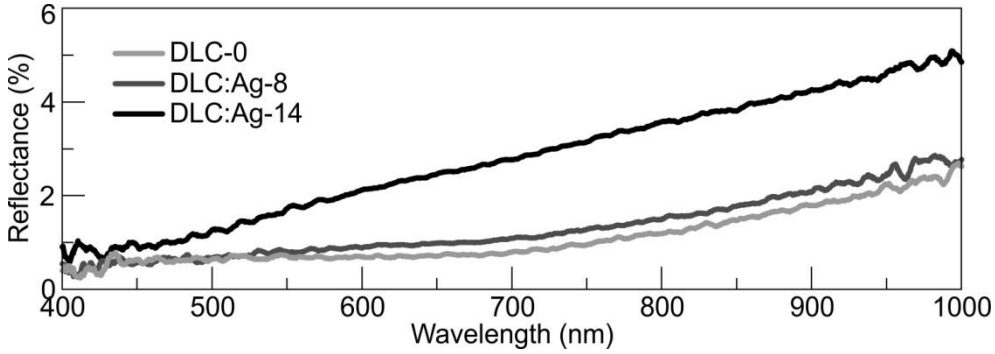

Fig. 4.22. Diffused reflectance spectra of DLC and DLC:Ag samples.

The normalized absorbance spectra of DLC:Ag samples on quartz substrates as calculated by using Equation (3.11) are depicted in Fig. 4.23 with the offset of each curve for clarity. DLC:Ag-8 and DLC:Ag-14 (in Fig. 4.23 legend, denoted as 7.9 at.% and 14.1 at.%, respectively) have broad absorbance peaks at 390 nm and 530 nm, respectively. Moreover, DLC:Ag-14 has a shoulder at 383 nm. The remaining samples also exhibit broad peaks or shoulders in the range of 363–412 nm. All of these peaks in DLC:Ag samples can be attributed to LSPR. All DLC:Ag samples exhibit reduced absorbance towards the IR range and also a minimum in UV at around 315–333 nm. Thicker samples absorb more, and thus it is not possible to quantitatively compare the differences in DLC:Ag spectra in the IR region. As expected, the absorbance spectrum of DLC (both thicknesses) is different from the nanocomposite spectra: it is more monotonous, and absorbance decreases with the increasing wavelength. DLC is almost transparent from 600–700 nm. This is a typical spectrum of a-C:H type DLC, as deposited from a C_2H_2 precursor [178].

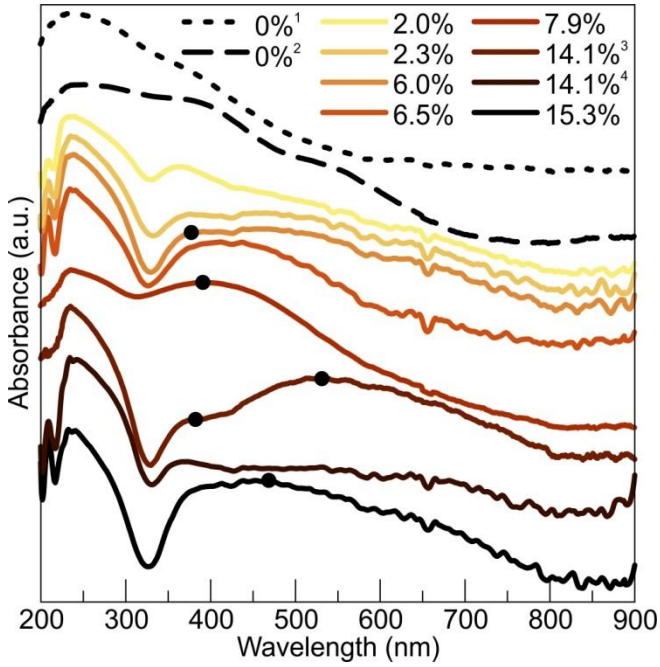

Fig. 4.23. Normalized and shifted for clarity optical absorbance spectra of DLC:Ag and DLC samples. The legend indicates silver atomic content in the sample. Here, the dashed lines are pure DLC ([1]DLC-0, [2]DLC-0'), and the solid lines are DLC:Ag (the colour darkens with the increasing silver concentration, [3]DLC:Ag-14, [4]DLC:Ag-14'). Black dots mark absorbance peaks used in Fig. 4.24. Published in [A4].

The imaginary part of dielectric function ε_2 of DLC (obtained by SE, Fig. 4.3) which describes the losses in the material agrees well with the absorbance spectra (the intermittent lines in Fig. 4.23): with the increasing wavelength, the value of ε_2 decreases and becomes constant in the infrared region, which is also true for absorbance.

The bimodal nature of the nanoparticle size distribution of the DLC:Ag-14 sample (see Fig. 4.17) can already be predicted from its absorbance spectrum (Fig. 4.23) since the latter has not only a peak, but also a shoulder. This is consistent with DLC:Ag-6, DLC:Ag-8, and DLC:Ag-15 samples which have single peaks in the absorbance spectra, and their nanoparticle size distributions are unimodal. DLC:Ag-7 demonstrates a fairly clear absorbance peak which is in between the shoulder and the peak of DLC:Ag-14 sample. This is consistent with nanoparticle distributions because DLC:Ag-7 had an increased number of nanoparticles with diameters of 15–35 nm, which is, consequently, in between DLC:Ag-14 x_c values of 17 nm and 46 nm.

The absorbance peak position for DLC:Ag was determined from the spectra in Fig. 4.23 (black dots), and its dependence on the central diameter of Ag nanoparticles in DLC:Ag thin films determined from lognormal fitting (see Fig. 4.17) was investigated. The resulting data from DLC:Ag-6, DLC:Ag-8, DLC:Ag-14, and DLC:Ag-15 and the linear fit are depicted in Fig. 4.24. For some samples, the

data was omitted from the investigation because x_c values were not available: DLC:Ag-7 and DLC:Ag-14' diameter distributions do not follow the lognormal law, whereas DLC:Ag-2 and DLC:Ag-2' do not have particles suitable for distribution analysis. The rest of the data seems to follow the quasi-linear relation, and the increased size of nanoparticles results in the red-shift of the absorbance peak, which is consistent with other studies [4, 185, 186]. The deviation from true linear dependence could be related to the broadness of absorbance peaks.

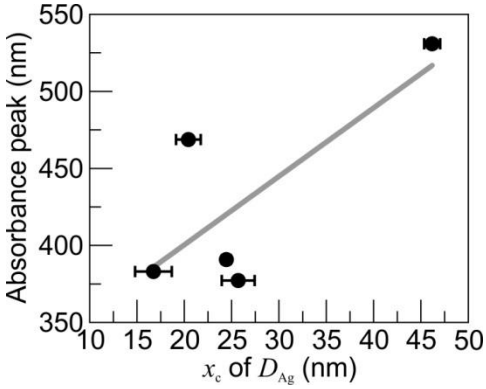

Fig. 4.24. Absorbance peak position dependence on x_c values of silver nanoparticle diameters (D_{Ag}) in DLC:Ag thin films. The grey line is linear fit to the data ($R^2 = 0.43$).

4.1.3.4. *Spectroscopic ellipsometry results*

Spectroscopic ellipsometry experimental curves together with the fitted ones (best fit) of DLC:Ag samples are presented in Fig. 4.25 (Δ) and Fig. 4.26 (Ψ). The dashed (fitted) curves match the solid (experimental) curves very well, and it can be concluded that the created optical model (described in the Modelling of ellipsometric parameters chapter) is suitable to describe DLC:Ag. When comparing DLC:Ag with at least 7.9 at.% silver ellipsometric spectra (Fig. 4.25, Fig. 4.26) with its absorbance spectra (Fig. 4.23), it can be noted that the extrema of the spectra fall into a very similar position: slightly above 300 nm.

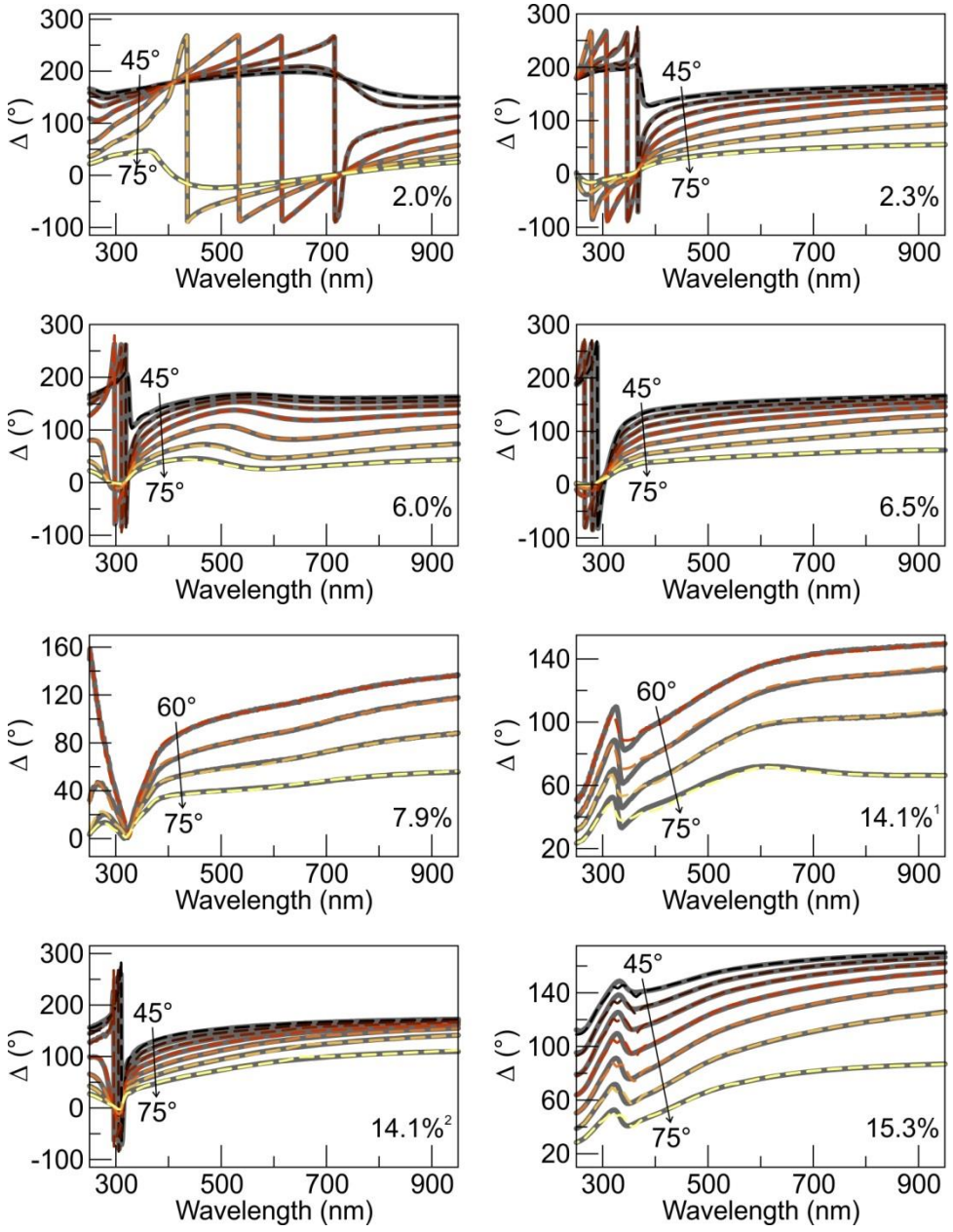

Fig. 4.25. Experimental (grey solid) and best fit (dashed) curves of ellipsometric parameter Δ of DLC:Ag samples on silicon substrate. The percentage indicates the atomic concentration of silver in the samples. The arrow and the changing colours indicate angle of incidence θ from 45° or 60° to 75° in steps of 5°. [1]DLC:Ag-14, [2]DLC:Ag-14'. Presented in [B1, B2, B8, B10, B12].

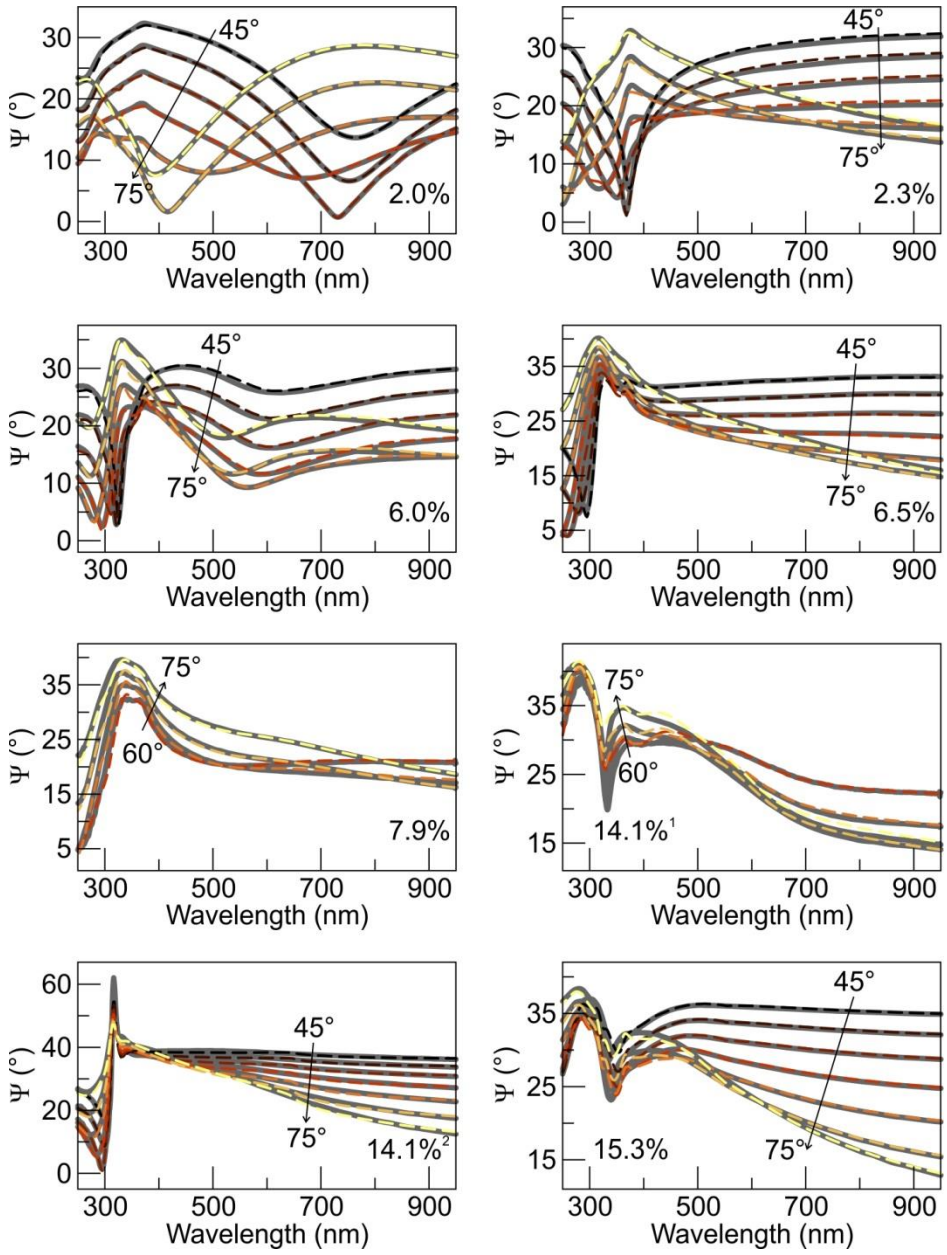

Fig. 4.26. Experimental (grey solid) and best fit (dashed) curves of ellipsometric parameter Ψ of DLC:Ag samples on silicon substrates. The percentage indicates the atomic concentration of silver in the samples. The arrow and the changing colours indicate angle of incidence θ from 45° or 60° to 75° in steps of 5°. [1]DLC:Ag-14, [2]DLC:Ag-14'. Presented in [B1, B2, B8, B10, B12].

The goodness of fit, total thickness, effective metal volume concentration, and effective refractive index at 632.8 nm wavelength obtained from SE measurements for DLC:Ag samples are presented in Table 4.7. From R^2 and RMSE values in Table

4.7, it can be seen that the model (Cody-Lorentz dispersion law for DLC, Bruggeman EMA for the nanocomposite layer) fits the data exceptionally well with $R^2 > 0.95$ and RMSE < 2.94.

Table 4.7. Spectroscopic ellipsometry fitting results for DLC:Ag samples: R^2 is the determination coefficient, RMSE is the root mean square error, *d* is thickness, *C* is metal volume concentration, n_{eff} is the effective refractive index of the whole nanocomposite film at 632.8 nm wavelength. The values are averages obtained from multiple measurements with standard deviations.

Sample	R^2	RMSE	*d* (nm)	*C* (V.%)	n_{eff}
DLC:Ag-2	0.96 ± 0.03	1.95 ± 0.30	74.7 ± 17.4	6 ± 3	1.99 ± 0.40
DLC:Ag-2’	0.96 ± 0.02	2.54 ± 0.76	54.5 ± 23.2	8 ± 4	1.86 ± 0.42
DLC:Ag-6	0.97 ± 0.01	2.10 ± 0.29	61.0 ± 11.7	10 ± 3	1.99 ± 0.16
DLC:Ag-7	0.97 ± 0.01	2.40 ± 0.90	57.1 ± 10.1	7 ± 1	2.17 ± 0.16
DLC:Ag-8	0.97 ± 0.02	1.88 ± 0.69	57.8 ± 13.9	9 ± 4	2.18 ± 0.14
DLC:Ag-14	0.95 ± 0.03	2.94 ± 1.55	42.5 ± 12.9	26 ± 15	2.11 ± 0.76
DLC:Ag-14’	0.97 ± 0.01	2.19 ± 0.28	65.5 ± 12.1	20 ± 3	2.75 ± 0.42
DLC:Ag-15	0.96 ± 0.02	1.93 ± 0.64	50.1 ± 20.2	21 ± 10	2.19 ± 0.40

The complete information about the employed DLC:Ag multilayered optical model for spectroscopic ellipsometry is given in Table 4.8. DLC:Ag samples not mentioned in the table were fitted by using a single layer for the nanocomposite, thus the results are directly presented in Table 4.7. Contrary to DLC:Cu nanocomposites, DLC:Ag samples were fitted by using the optical model with fewer layers because it significantly reduces the fitting time, whereas the goodness of fit is still very good.

Table 4.8. Optical 2-layer model parameters of DLC:Ag thin film obtained by spectroscopic ellipsometry. Here, *d* is the thickness of the layer, *C* is the volume concentration of silver, *n* is refractive index at 632.8 nm wavelength. The values are presented with standard deviations.

Sample	Parameter	Layer No.	
		1	2
DLC:Ag-2	*d* (nm)	33.5±16.5	41.2±12.4
	C (V.%)	5.1±2.3	5.1±4.4
	n	1.96±0.70	1.78±0.62
DLC:Ag-2’	*d* (nm)	24.7±13.9	29.8±13.4
	C (V.%)	11.9±10.8	5.8±4.7
	n	1.96±0.55	1.69±0.48
DLC:Ag-6	*d* (nm)	30.0±10.9	31.0±12.2
	C (V.%)	11.2±4.0	9.1±4.0
	n	2.07±0.79	1.65±0.63
DLC:Ag-7	*d* (nm)	31.6±14.5	25.5±7.3
	C (V.%)	3.9±4.0	9.7±6.0
	n	2.52±0.64	1.91±0.11
DLC:Ag-14’	*d* (nm)	42.4±6.7	23.0±9.8
	C (V.%)	19.1±6.7	21.8±5.7

	n	3.15±0.41	1.84±0.93
DLC:Ag-15	*d* (nm)	24.7±12.6	25.3±14.2
	C (V.%)	25.2±17.3	14.1±5.8
	n	3.05±0.92	1.60±0.42

The thickness values of the nanocomposites as determined by various techniques are compared in Table 4.9. DLC:Ag-2 thickness from SE is lower than that determined from TEM. This difference could be caused by an assumption in the SE model that the sample has silver nanoparticles, however, they were very scarce. The most prominent disagreement in the thickness values stems from quartz microbalance. DLC:Ag tend to exhibit much higher thicknesses according to quartz microbalance. Also, DLC:Ag samples are distinct with their high standard deviations in SE measurements. The measurements were obtained at different spots on the sample, and some of them had colour changes across the sample. This could indicate variations in the film thickness. Additionally, differences in the results might be due to surface roughness. The same reasoning is valid for the thickness of DLC (Table 4.1).

Table 4.9. The comparison of DLC:Ag and DLC thickness obtained by different techniques: quartz microbalance during the deposition, transmission electron microscopy (TEM), and spectroscopic ellipsometry (SE).

Sample	Thickness (nm)		
	Quartz microbalance	TEM	SE[a]
DLC:Ag-2	140	117.7	74.7 ± 17.4
DLC:Ag-2’	100	-	54.5 ± 23.2
DLC:Ag-6	120	-	61.0 ± 11.7
DLC:Ag-7	100	-	57.1 ± 10.1
DLC:Ag-8	60	-	57.8 ± 13.9
DLC:Ag-14	60	-	42.5 ± 12.9
DLC:Ag-14’	160	-	65.5 ± 12.1
DLC:Ag-15	100	26.8-74.8	50.1 ± 20.2

[a]The error value in spectroscopic ellipsometry results is the standard deviation of the values obtained for the same sample at different spots.

Silver volume concentration and refractive index dependencies on silver atomic concentration are summarized in Fig. 4.27. The linear model fits the data reasonably well in both cases. In Fig. 4.27b, the pure DLC refractive index value is also included (i.e., the average of DLC-0 and DLC-0’), which also agrees with the linear fit. A good linear fit of differently estimated silver concentrations should be expected and proves that spectroscopic ellipsometry is a feasible approach to determine the volume concentration of metal particles in a nanocomposite film.

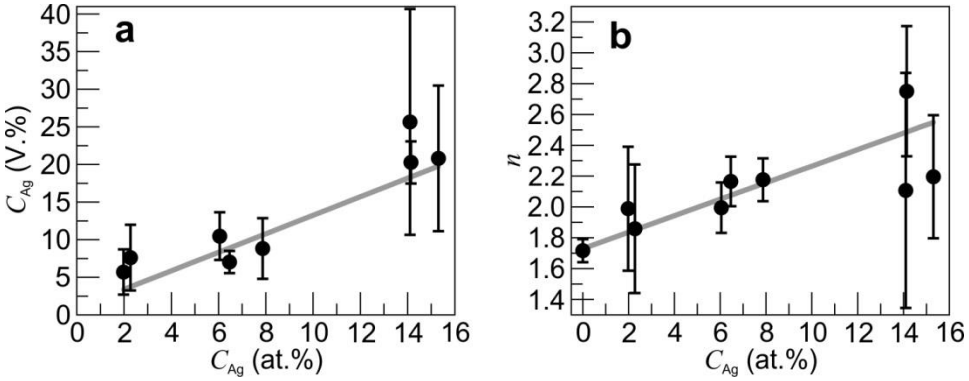

Fig. 4.27. Silver volume concentration (a) and refractive index of DLC:Ag at 632.8 nm wavelength (b) determined from SE dependencies on atomic silver concentration determined from EDS. Dots are the average values obtained from SE fittings, and error bars are standard deviations. Grey lines are linear fits ($R^2 = 0.77$ and $R^2 = 0.87$, respectively).

By comparing silver and copper containing DLC thin films refractive indices dependencies on metal concentrations (Fig. 4.27a and Fig. 4.12a, respectively), it is visible that they are both increasing at relatively low metal concentrations. At higher metal concentrations, the DLC:Cu refractive index starts to decrease. Further research with higher silver concentrations would be of interest in order to discover whether the increasing trend continues or starts to drop as in the case of DLC:Cu.

The dielectric functions obtained from SE fittings for DLC:Ag samples are summarized in Fig. 4.28 (ε_1) and Fig. 4.29 (ε_2). DLC:Ag dielectric functions agree with the absorbance spectra (Fig. 4.23) by having a dip at approximately 330 nm. This dip was not observed in DLC dielectric functions (Fig. 4.3) and thus is a result of silver in the thin film. In the case of pure silver (Fig. 2.2), there is a peak at the same wavelength in ε_1 and a dip in ε_2. As the extrema features of the metals are preserved, the nanocomposites are still plasmonic. The values of dielectric functions of DLC:Ag (Fig. 4.28, Fig. 4.29) are very different from pure silver (Fig. 2.2). The real part of the dielectric function no longer features a negative part, and, in most cases, it is very constant: it changes very slightly with the change of the wavelength. This is partly because the results are averaged throughout the sample, which might have some inconsistencies in the film. When incorporated in the device, the material could work the same way at any incident light, thus making it a versatile option. The imaginary part of the dielectric function exhibits lower values in nanocomposites than in pure silver. This is advantageous because it indicates lower losses in the material.

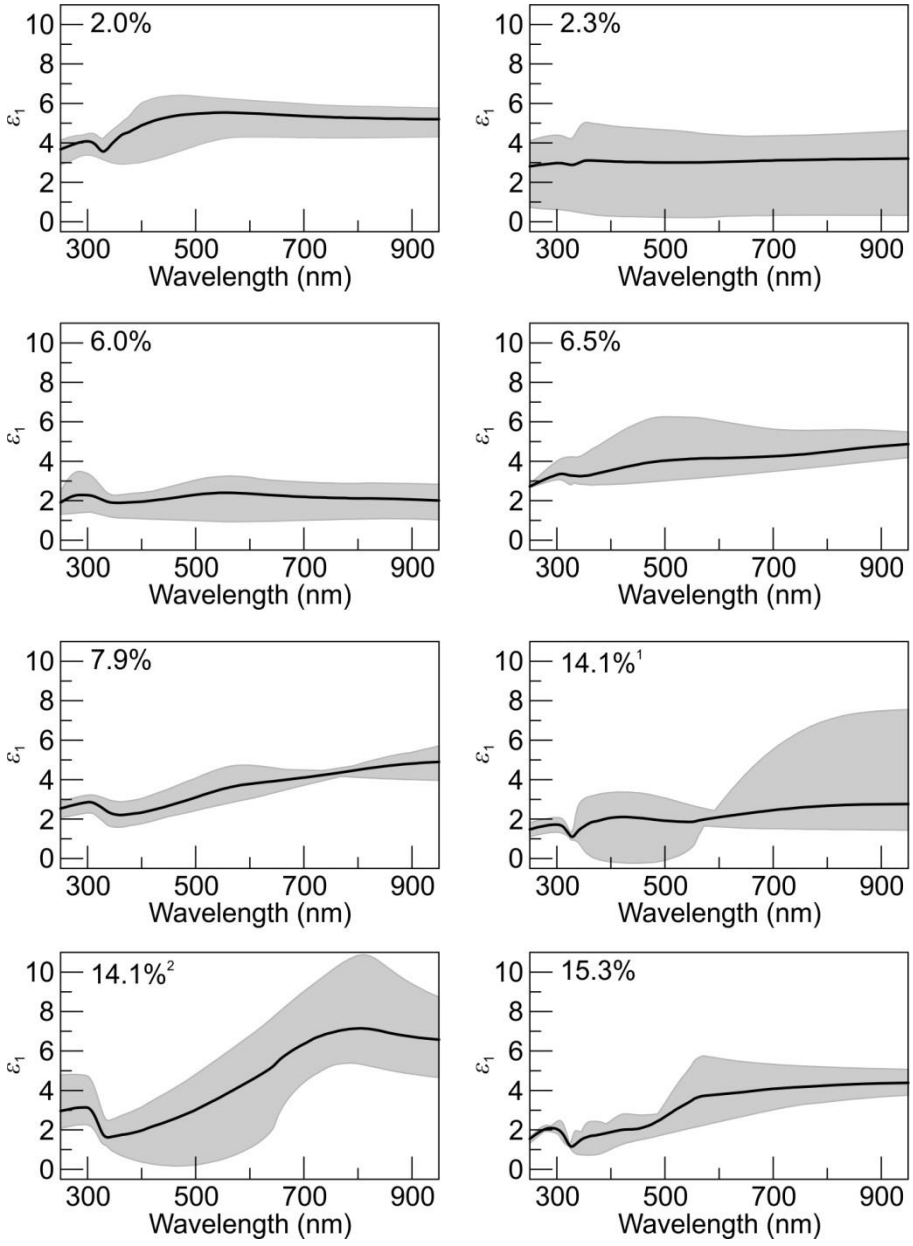

Fig. 4.28. The real part (ε_1) of dielectric function of DLC:Ag nanocomposite films. Black line is average value obtained after fitting all the measured spots on a sample. The grey shaded area represents the lowest and highest values from fitting. The percentage is the atomic concentration of silver in the film.

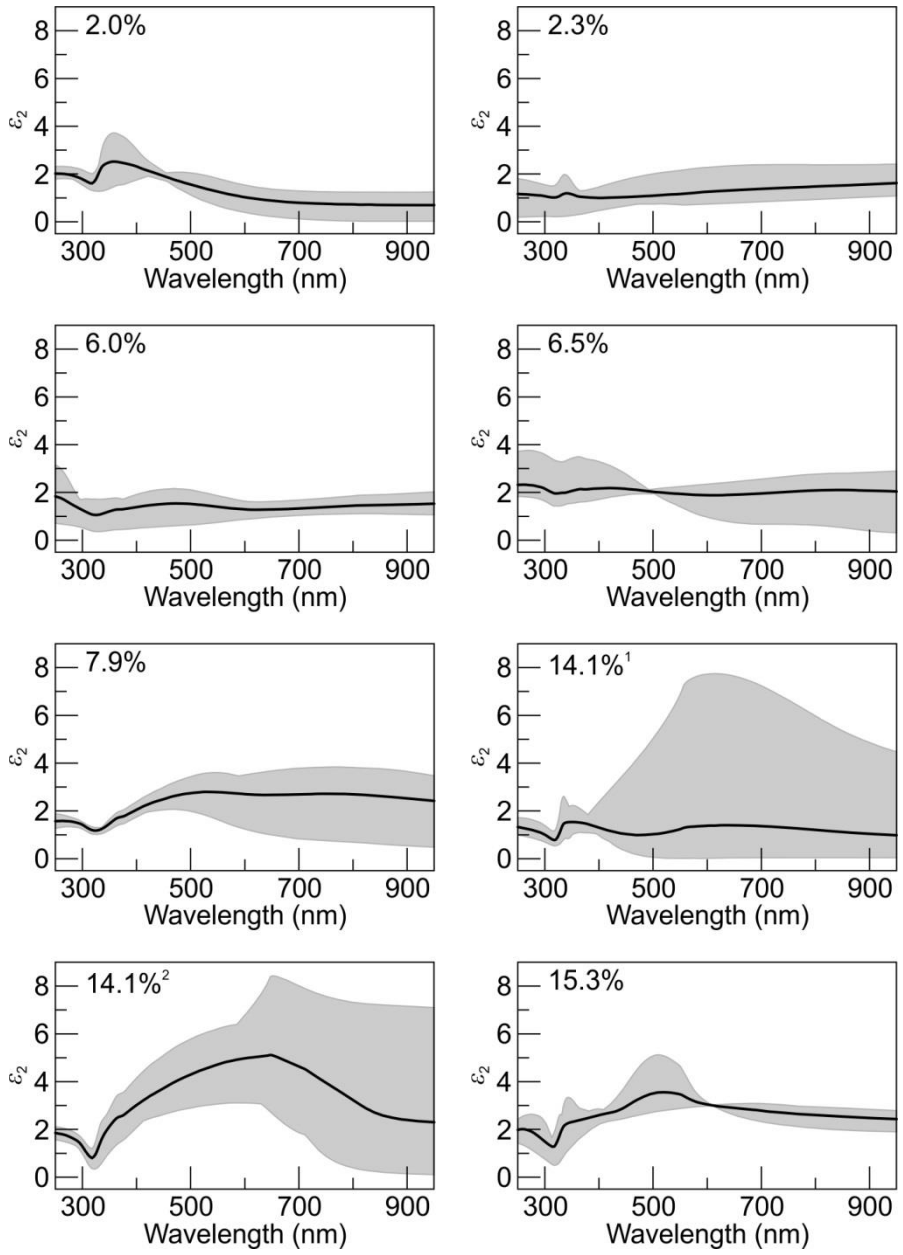

Fig. 4.29. The imaginary part (ε_2) of dielectric function of DLC:Ag nanocomposite films. Black line is average value obtained after fitting all measured spots on a sample. The grey shaded area represents the lowest and highest values from fitting. The percentage is the atomic concentration of silver in the film.

4.2. Periodic structures in thin films

After the investigation of pristine nanocomposites, the next step was to create periodic patterns in them. At first, interference patterns were calculated (Fig. 4.30)

by using *MATLAB* software and laser beam interference formalism which was extensively described in [A2] in order to investigate the possible geometries. These models can be used to predict the pattern for both holographic lithography and direct laser interference patterning.

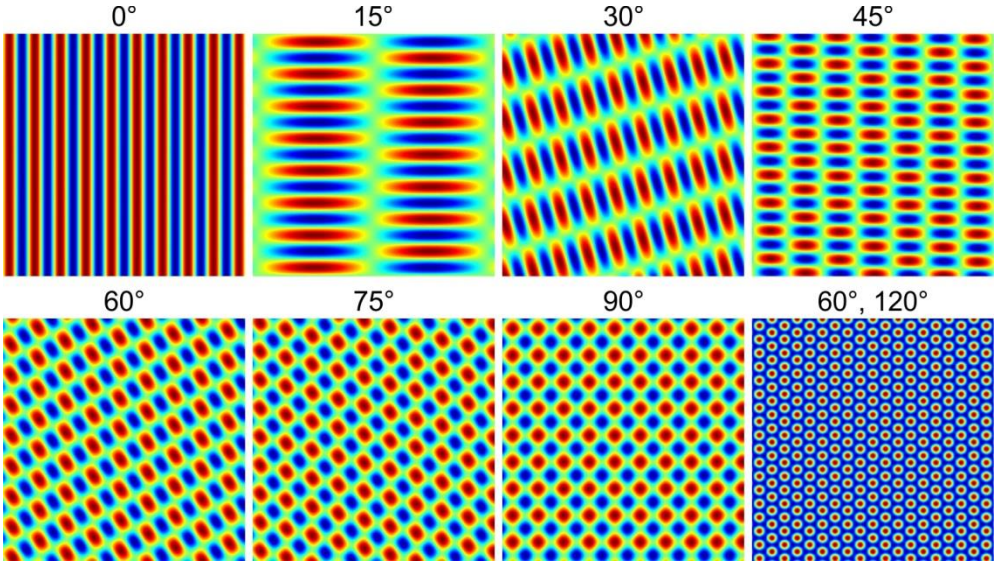

Fig. 4.30. Two beam interference field models for different numbers of exposure and angles between them: single exposure (0°), double exposure (15°–90°), and triple exposure (60°, 120°). Red parts correspond to maxima, while blue parts correspond to minima. Published in [A2].

The modelling was tested while fabricating structures in photoresist by employing the holographic lithography technique. The obtained pitch of the periodic structures was 1.2 μm. The fabricated structures were with periodicities in one and two dimensions (Fig. 4.31, the angle between exposures is indicated above each image) with the corresponding point lattice types: rhombus (15°, 30°, 45°, 75°), triangular (60°, triple exposure with 60° and 120°), and square (90°). The rotational symmetry of 2D structures was 2-fold (15°, 30°, 45°, 60°, 75°), 4-fold (90°), or 6-fold (triple exposure with 60° and 120°). By comparing the calculated models as shown in Fig. 4.30 and the micrographs of the corresponding patterns in Fig. 4.31, it is clear that the experiment matches the modelling exceptionally well. The variations from the ideal shapes of the patterned structures appear from the local variations of the exposure intensity or the thickness of the photoresist. Not all of the patterns were exposed through the full depth of the photoresist, which resulted in a reduced contrast of the periodic pattern (Fig. 4.31 30°, 75°, and triple exposure). In holographic lithography, the pattern quality depends on the ratio of exposure times. The quality is described as the intensity of diffracted light from the pattern in the first order maxima. It is the highest when all of the first diffraction maxima have the same intensity. Three exposures of equal durations gave the worst efficiency of light in the diffracted first order maxima. Thus, the duration of each exposure must be tailored individually to obtain the best results.

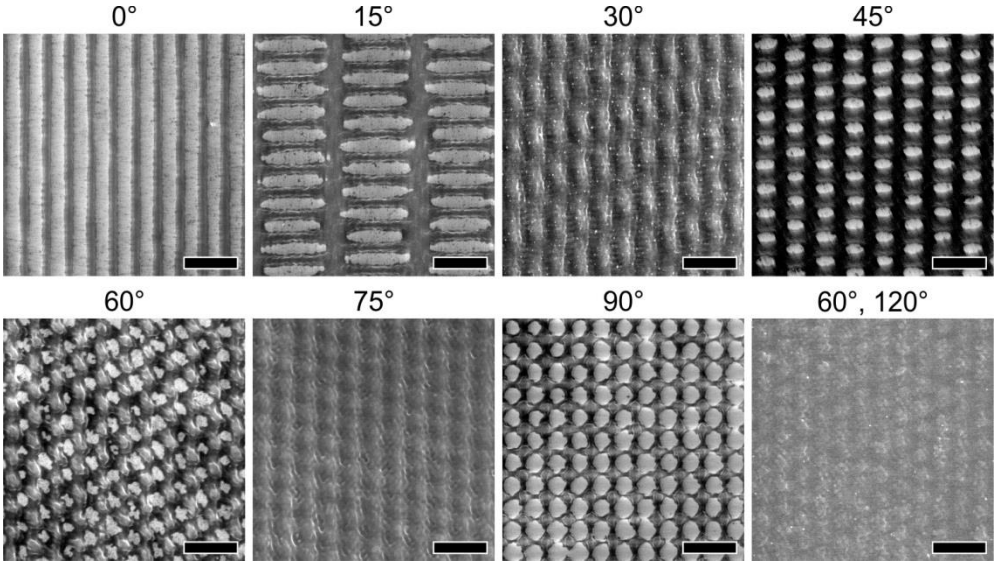

Fig. 4.31. SEM micrographs of 1D (0°, single exposure) and 2D (15°–90° double exposures, 60°, 120° triple exposure) periodic structures in photoresist on glass substrates fabricated by HL. Mark size is 3 μm. Published in [A2].

The FFTs of images of periodic structures in photoresist fabricated by holographic lithography are depicted in Fig. 4.32. It is evident that different point lattice and symmetry types yield unique diffraction patterns.

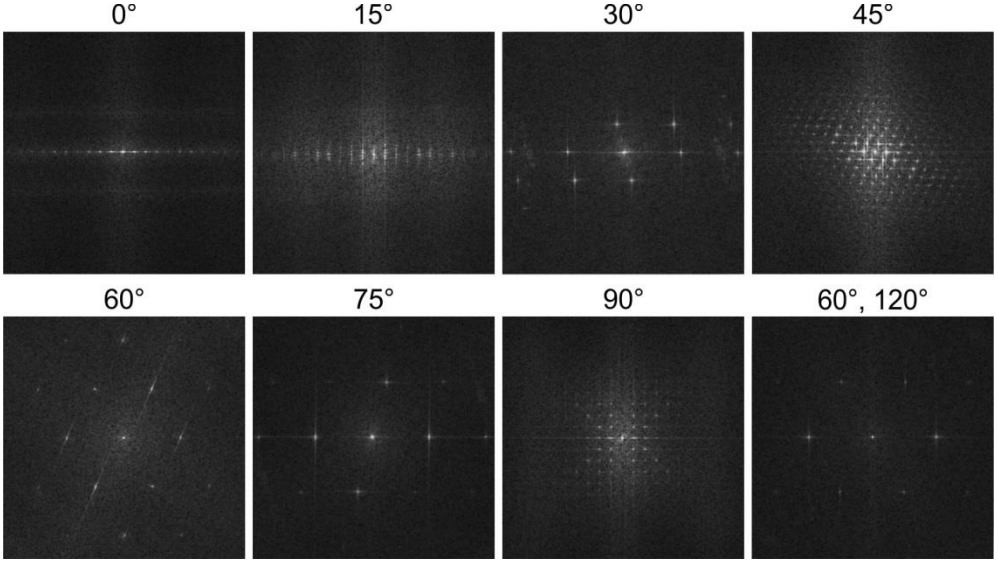

Fig. 4.32. FFTs of 1D (0°, single exposure) and 2D (15°–90° double exposures, 60°, 120° triple exposure) periodic structures in photoresist from optical microscope and SEM (Fig. 4.31) micrographs. Published in [A2].

As the calculated patterns were verified in the photoresist by using holographic lithography, the simplest cases were carried out in nanocomposite by using direct laser interference patterning. The resulting structure of double DLIP with a 90° angle in between irradiations in DLC:Ag-7 is depicted in Fig. 4.33. A lower magnification micrograph (Fig. 4.33a) also shows unaffected film on the left for better understanding of the affected area. A close-up micrograph (Fig. 4.33b) shows square formations of silver nanoparticles with a pitch in both directions of about 1.3 μm. In between the squares, the nanoparticles seem to be removed, or at least their concentration is effectively reduced.

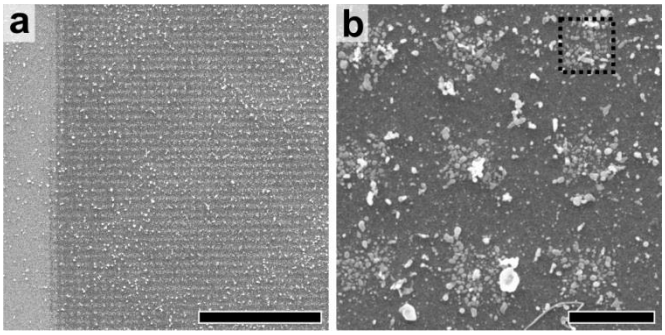

Fig. 4.33. SEM micrographs of two magnifications of 2D (double irradiation with 90° angle) periodic structures in DLC:Ag-7 thin film fabricated by DLIP with 4 mJ/cm^2 laser fluence and 1000 pulses. One of the square formations of silver nanoparticles is marked for clarity. Mark sizes are 20 μm (a) and 1 μm (b).

Even though the 2D pattern was successfully implemented in the DLC:Ag thin film, the best laser parameters for DLIP still had to be determined. It was decided to systematically study the effects of laser fluence and the number of pulses on the 1D periodic pattern and silver nanoparticles. The structures with two pitches in DLC:Ag were fabricated: 564 ± 14 nm and 1306 ± 46 nm as determined from the FFTs of SEM and HIM micrographs. Typical SEM and HIM images are depicted in Fig. 4.34 (DLC:Ag-8, 564 nm), Fig. 4.35 (DLC:Ag-8, 1306 nm), Fig. 4.36 (DLC:Ag-14, 564 nm), Fig. 4.37 (DLC:Ag-14, 1306 nm), Fig. 4.38 (DLC-0), and Fig. 4.39 (Ag-100).

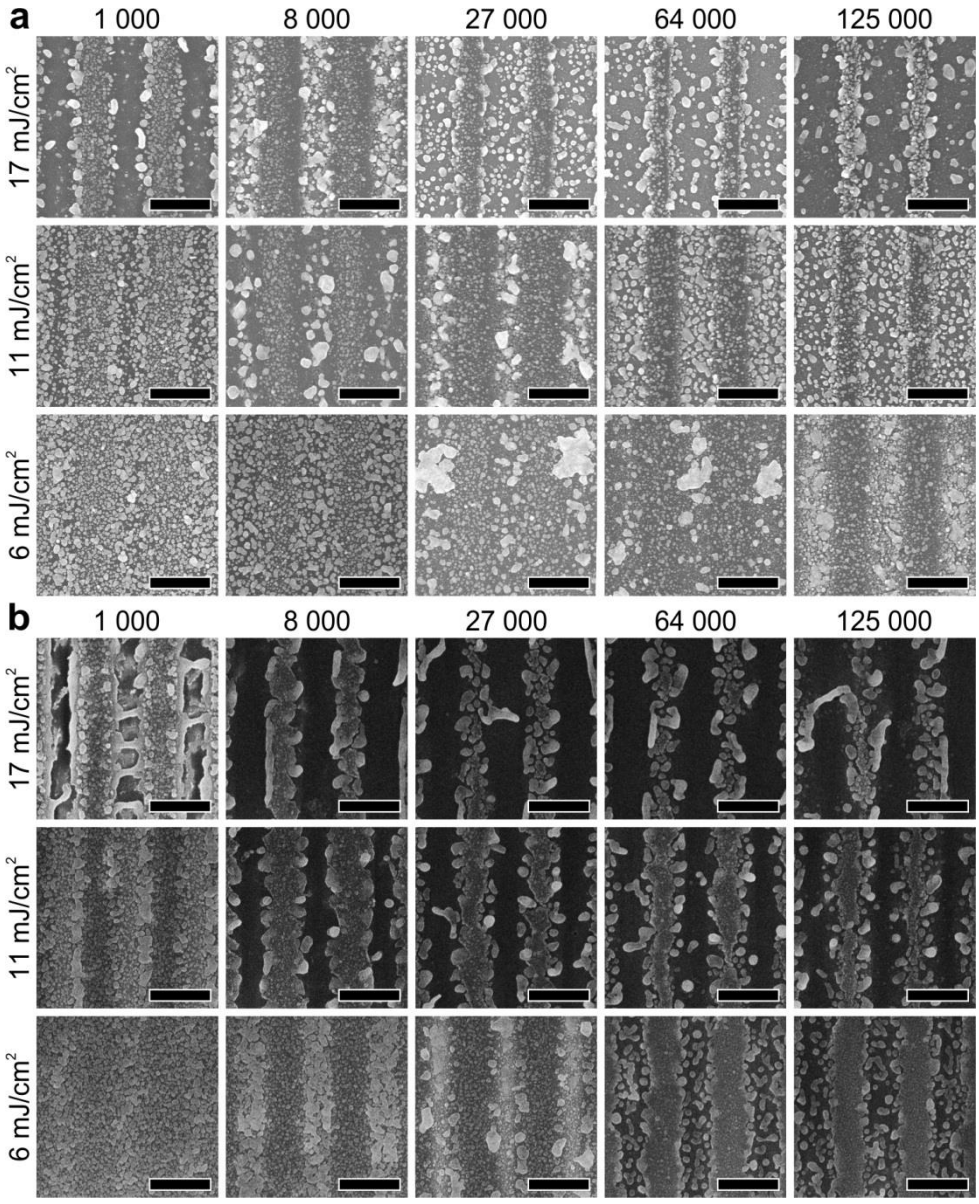

Fig. 4.34. Micrographs of 564 nm pitch periodic structures in DLC:Ag-8 on silicon (a, SEM) and quartz (b, HIM) substrates. Mark size is 500 nm. Laser fluence is indicated to the left of the image, while the number of pulses is at the top. Published in [A4], presented in [B5, B9, B11].

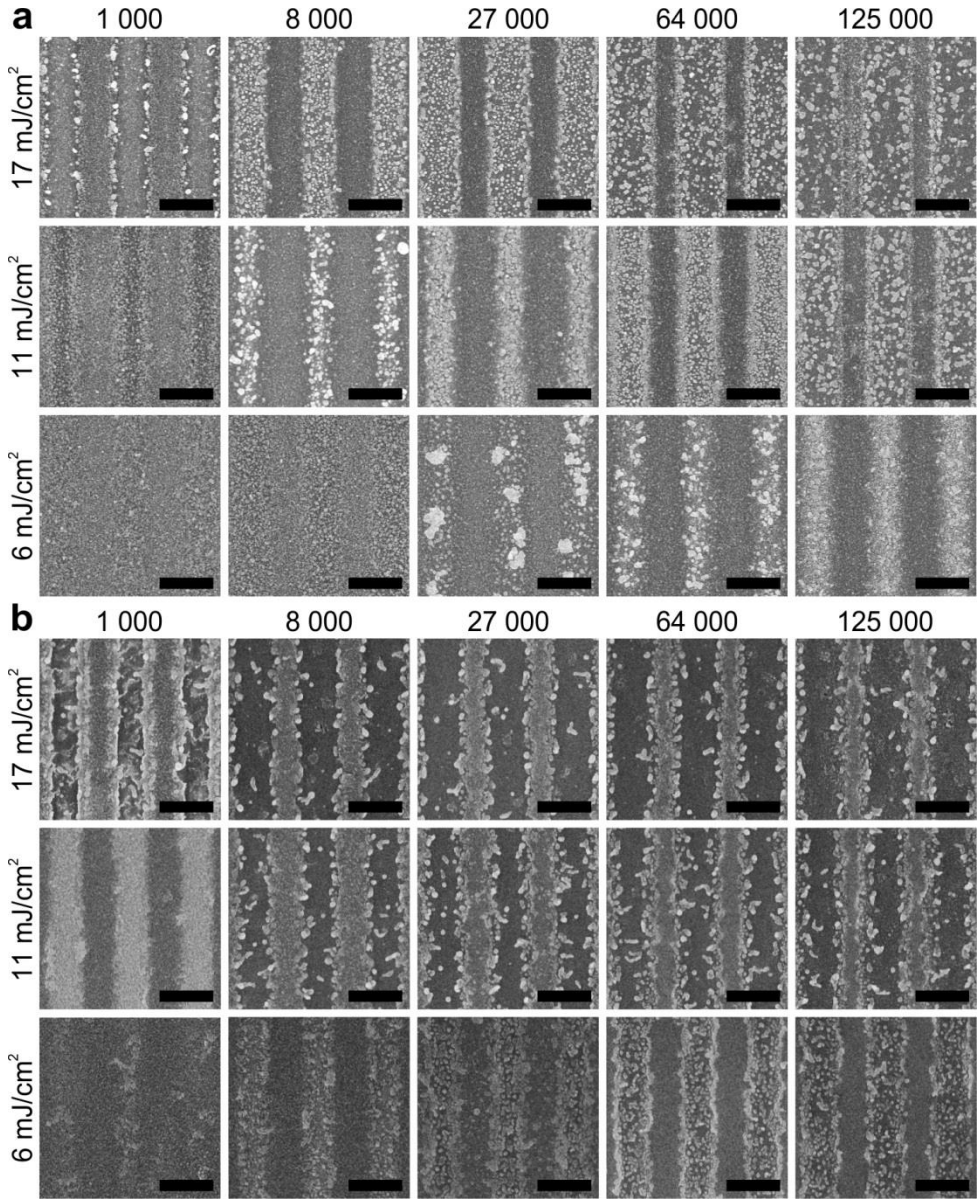

Fig. 4.35. Micrographs of 1306 nm pitch periodic structures in DLC:Ag-8 on silicon (a, SEM) and quartz (b, HIM) substrates. Mark size is 1 μm. Laser fluence is indicated to the left of the image, while the number of pulses is at the top. Published in [A4], presented in [B4, B5].

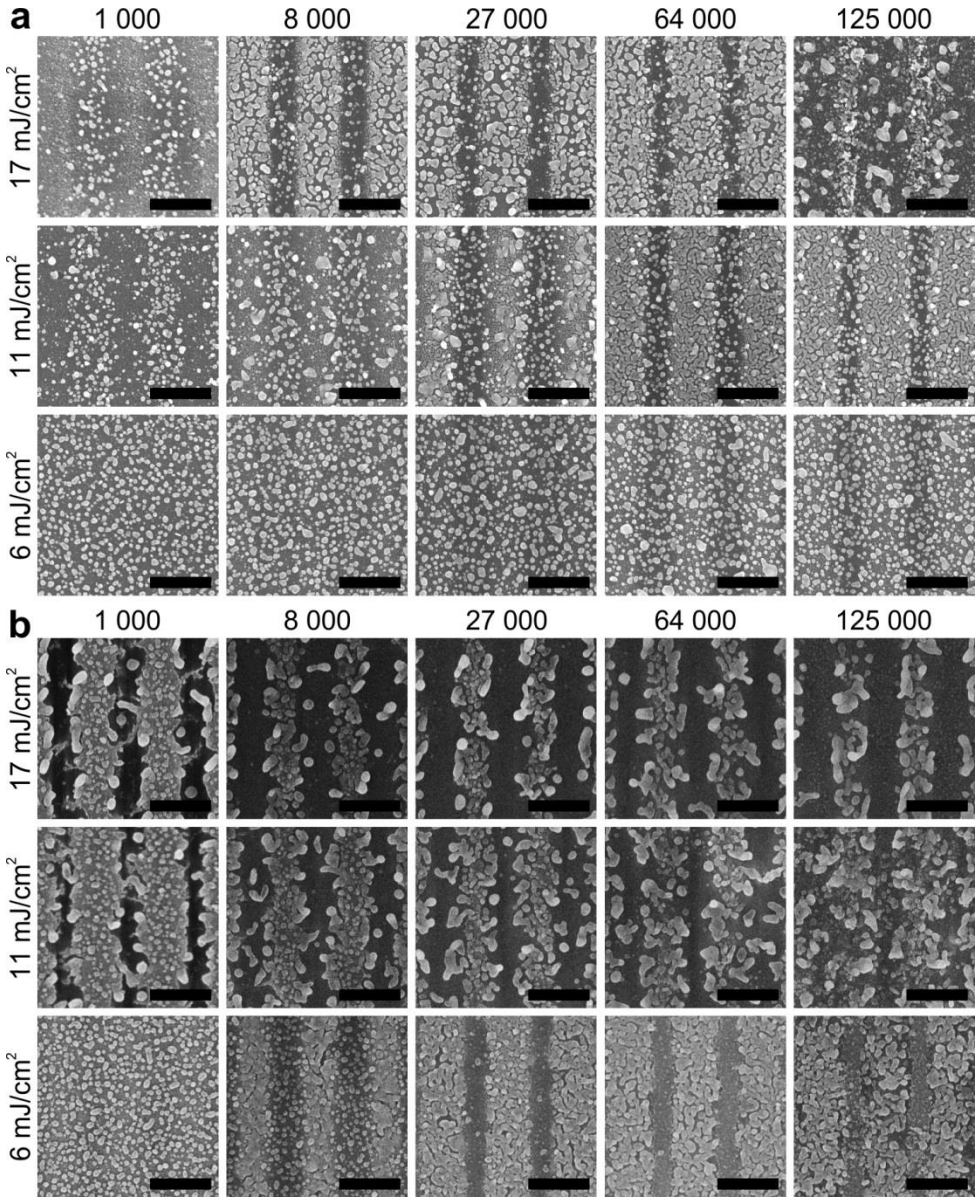

Fig. 4.36. Micrographs of 564 nm pitch periodic structures in DLC:Ag-14 on silicon (a, SEM) and quartz (b, HIM) substrates. Mark size is 500 nm. Laser fluence is indicated to the left of the image, while the number of pulses is at the top. Published in [A4], presented in [B4, B5].

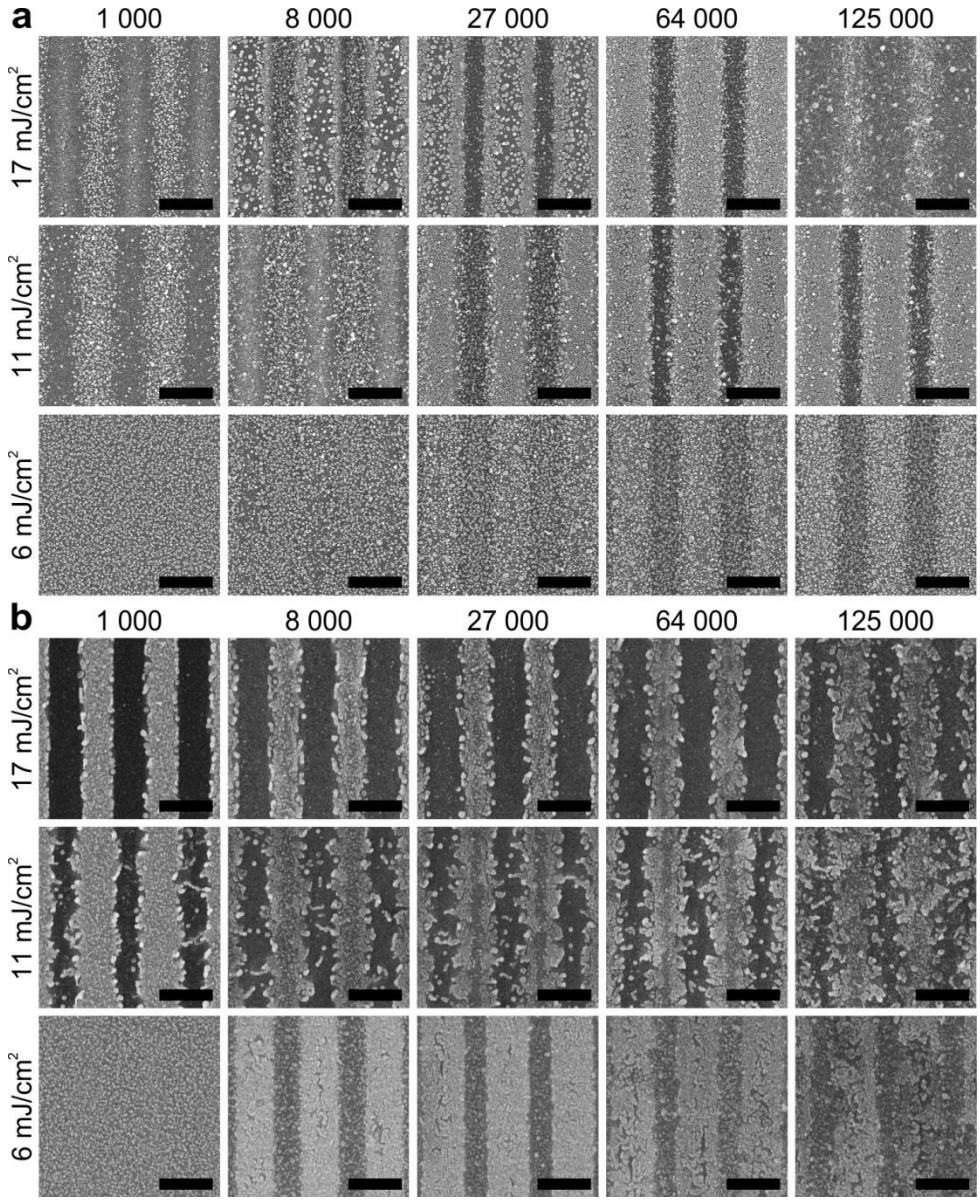

Fig. 4.37. Micrographs of 1306 nm pitch periodic structures in DLC:Ag-14 on silicon (a, SEM) and quartz (b, HIM) substrates. Mark size is 1 μm. Laser fluence is indicated to the left of the image, while the number of pulses is at the top. Published in [A4], presented in [B5, B11].

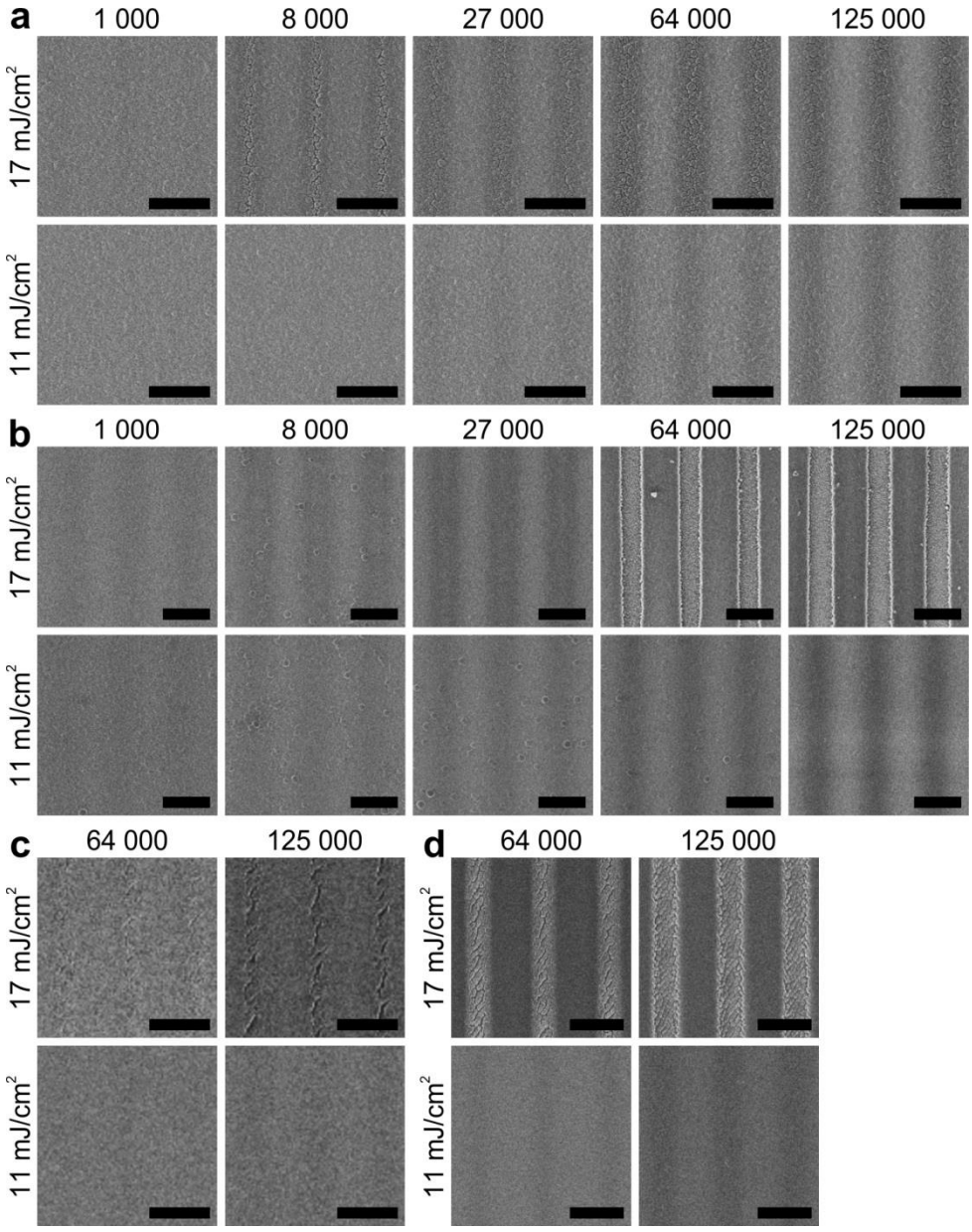

Fig. 4.38. HIM micrographs of periodic structures in DLC-0: (a) 564 nm on silicon substrate, mark size is 500 nm, (b) 1306 nm on silicon substrate, mark size is 1 μm, (c) 564 nm on quartz substrate, mark size is 500 nm, (d) 1306 nm on quartz substrate, mark size is 1 μm. The laser fluence and the number of pulses are indicated to the left and at the top of the image, respectively. Published in [A4], presented in [B4, B5, B11].

A pure silver thin film (Ag-100, Fig. 4.39) was irradiated specifically with higher laser fluence. However, the patterning was not successful: lower fluences resulted in a very small patterned area, while, at the highest, 145 mJ/cm^2, fluence,

the film was perforated and the substrate was ablated. Henley *et al*. reported that thinner films require higher laser fluence for structurization. The authors observed similar perforation of thinner nickel films upon laser irradiation, while thicker films broke up into discrete particles [187]. Delamination of a tetrahedral amorphous carbon film from the silicon substrate was also reported in [63]. This was associated with the distances between the interference maxima being shorter than the thermal diffusion length of silicon. Thus, the heat conducts through the film into the substrate and results in melting and delamination.

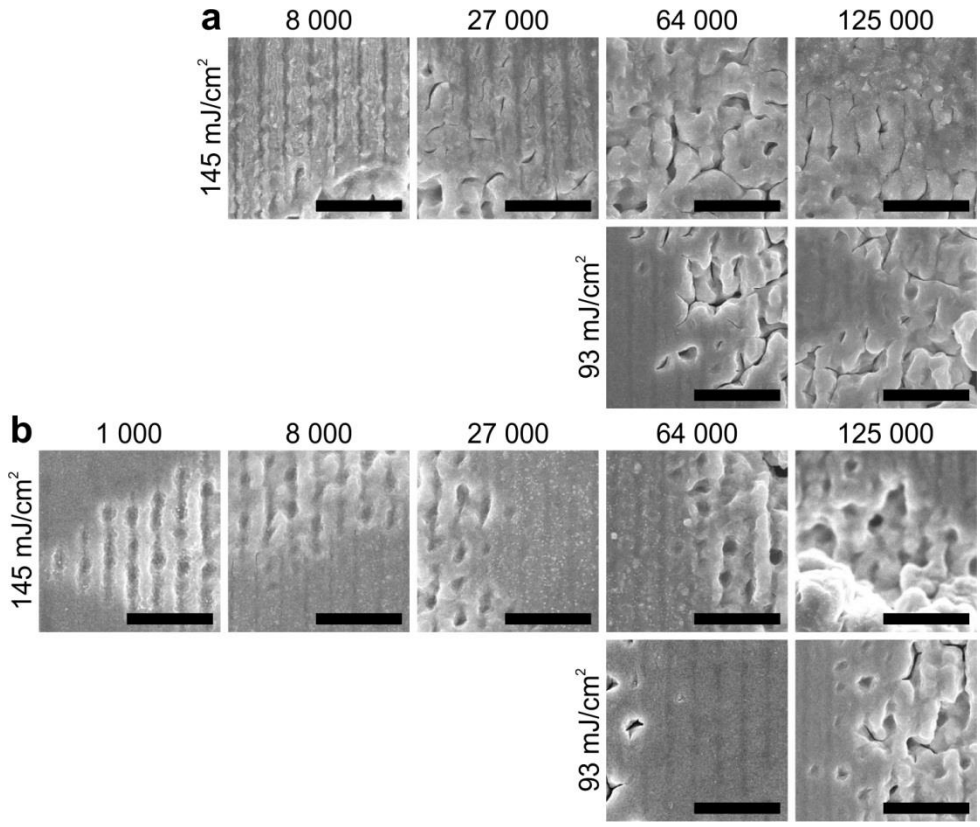

Fig. 4.39. SEM micrographs of 564 nm periodic structures in Ag-100 film on silicon (a) and quartz (b) substrates. Mark size is 2 μm. Published in [A4], presented in [B4, B5, B11].

Representative FFTs of micrographs of DLC:Ag and DLC periodic structures are presented in Fig. 4.40 and Fig. 4.41, respectively. Well pronounced periodic patterns have clear FFTs. When the pattern appears without sharp edges (with a slight grey gradient in the image, common to DLC-0 HIM micrographs), the FFT still shows a good diffraction image, and thus the patterning can be considered successful. In Fig. 4.40, at both pitches, FFTs of 1 mJ/cm^2 and 1 000 pulses have only single white dot in the centre, and it means that the pattern at this energy density does not exist. The same is valid for DLC at 17 mJ/cm^2 and 1 000 pulses (Fig. 4.41). When comparing FFTs of different pitches, it is evident that, for a higher

pitch, the maxima in the FFTs (bright spots) are closer together (the comparison is valid when FFTs are obtained from the same magnification images).

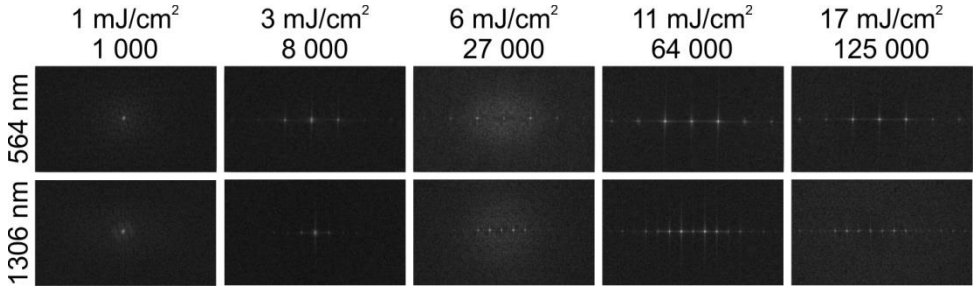

Fig. 4.40. FFTs of periodic structures in DLC:Ag-8 sample on silicon substrate obtained from SEM micrographs (Fig. 4.34, Fig. 4.35) of 564 nm and 1306 nm pitches and affected with 1–17 mJ/cm^2 laser fluence and 1 000–125 000 pulses. Published in [A4], presented in [B11].

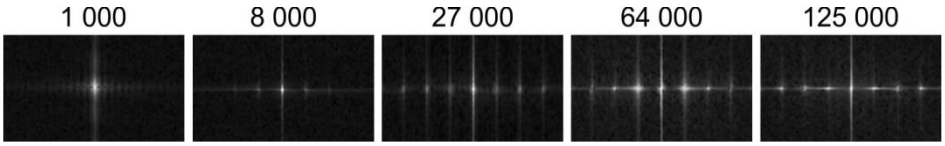

Fig. 4.41. FFTs of periodic structures in DLC-0 sample on quartz substrate obtained from HIM micrographs (Fig. 4.38b) of 1306 nm pitch and affected with 17 mJ/cm^2 laser fluence and 1 000–125 000 pulses. Published in [A4].

The cross-section of the DLC:Ag sample with the highest silver content (15.3 at.%) after irradiation with the highest number of pulses (125 000) was investigated by using HIM. This was possible after the removal of the material with a gallium ion beam which is available at the same HIM system. The corresponding micrographs are depicted in Fig. 4.42. The laser affected depth was determined to be around 35 nm. As it was already noticed for pristine DLC:Ag films (Fig. 4.18, Fig. 4.19), silver nanoparticles are still situated more on the surface of the film than in it. After laser irradiation, nanoparticles became bigger and less dense.

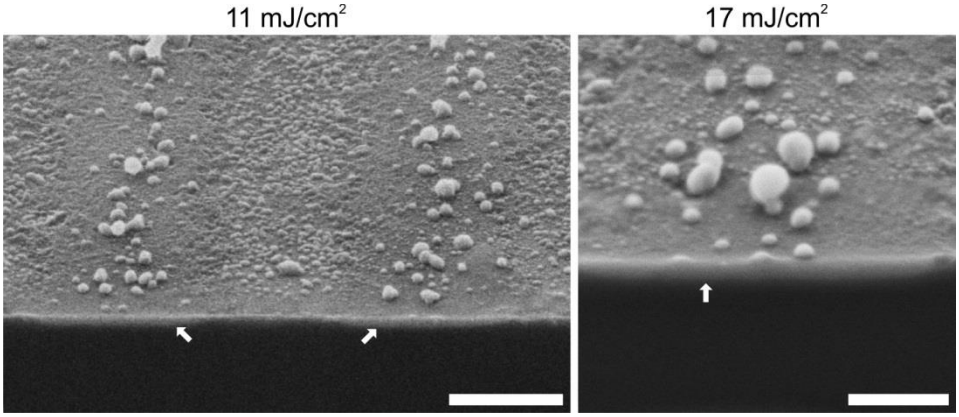

Fig. 4.42. HIM cross-section micrographs of DLC:Ag with 15.3 at.% silver on silicon substrate after irradiation with 125 000 pulses and 11 mJ/cm^2 (mark size is 500 nm) and 17 mJ/cm^2 (mark size is 200 nm). Arrows indicate the affected depth of the film. Presented in [B3, B7, B13].

4.2.1. *Tendencies of the width of laser irradiated line*

The investigation of the laser affected line width *W*, as obtained from micrographs as shown in Fig. 4.34–Fig. 4.37, dependence on the applied number of pulses is depicted in Fig. 4.43. With the increasing number of pulses, the width of the affected line increases and approaches a value close to the pitch of the periodic structure. At higher laser fluences (11 and 17 mJ/cm^2), the increase is faster (the steeper line increase in the graph) compared with the lower fluence (6 mJ/cm^2).

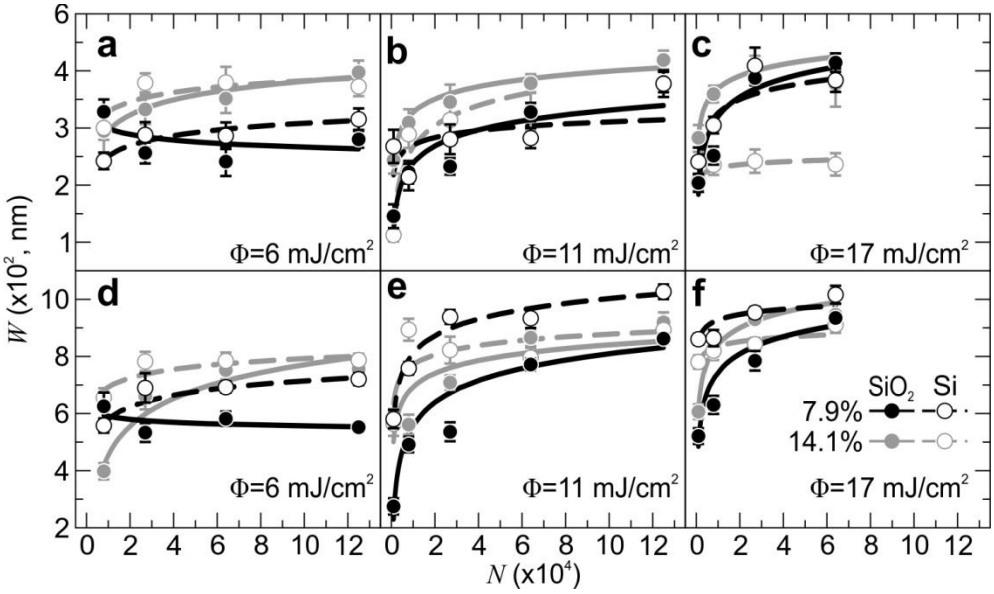

Fig. 4.43. Dependence of laser affected line width *W* on the number of applied pulses *N* in 564 nm (a–c) and 1306 nm (d–f) pitch cases at laser fluence of 6 mJ/cm^2 (a, d), 11 mJ/cm^2

(b, e), and 17 mJ/cm^2 (c, f). Error bars are the standard deviation of multiple measurements. The lines only serve as guides for the eyes. Published in [A4], presented in [B11].

When the interference field is employed for patterning, the sample surface is affected only at the vicinity of the interference maxima where the intensity value is above the threshold (Fig. 2.4). When increasing the laser intensity, the larger part of the interference field is above the threshold, which results in wider features on the sample surface. Additionally, when applying multiple pulses on the same spot, the threshold value is lowered, and thus the width can be increased without the change in laser fluence. When irradiated up to 27 000 pulses, the width of the laser affected line increases up to 2 times. A further increase of the number of pulses results in an additional increase in the laser affected line width of up to 1.2 times. When the intensity of two interfering beams is equal, the light intensity in the interference minima is equal to zero. This means that the light at the minima cannot reach the intensity above the threshold and there should always be at least a very narrow unaffected line. This explains why the width dependence on laser fluence and the number of pulses reaches the saturation value close to the pitch. Similar results were previously reported on the ablation of nickel foil when using the same DLIP setup: very narrow lines remained at the maximum applied laser energy density [123].

At first, it was assumed that the analysis of the width could lead to the patterning threshold value. However, the sinusoidal nature of the interference field made it hard to determine some of the edges of the laser affected lines thus introducing errors in measurements. Taking into account the data only from micrographs with the sharpest contrast between the affected and the unaffected lines, the data set was too small to make confident conclusions, and the patterning threshold determination from the width analysis became unfeasible.

4.2.2. *Patterning and ablation thresholds*

The patterning threshold for DLC:Ag was determined from the FFTs (Fig. 4.40) of SEM and HIM micrographs: when the diffraction pattern is present at the FFT, the fluence was assumed to be above the patterning threshold. When the FFT had a single bright spot in the centre, the fluence was assumed to be below the threshold. However, this method offers only an approximate value of the patterning threshold, and the real threshold is in between the two (below/above) determined values. For DLC:Ag-8, the determined patterning threshold values are below 6 mJ/cm^2 (1 000 pulses), 3 mJ/cm^2 (8 000 pulses), and 1 mJ/cm^2 (27 000 and more pulses). The DLC:Ag-14 patterning threshold is below 11 mJ/cm^2 (1 000 pulses), 6 mJ/cm^2 (8 000 and 27 000 pulses), and 3 mJ/cm^2 (64 000 and 125 000 pulses). These values are valid for the studied thin films on both silicon and quartz substrates.

The patterning of the silver thin film resulted in perforation, and, because of that, it was assumed that the applied laser fluence was below the threshold, i.e., the threshold is above 145 mJ/cm^2 at any number of applied pulses.

DLC was additionally irradiated with increased laser fluence. The optical microscope images of the resulting patterned areas are depicted in Fig. 4.44. After measuring the diameter D of each irradiated area, the ablation threshold of DLC was

determined from Eq. (3.2): D^2 dependence on lnΦ was plotted, and the linear fit was applied (Fig. 4.45). This approach was suitable for the case of DLC because the entire irradiated areas can be approximated into the Gaussian shape. The threshold value for a certain number of pulses is the one at the intersection of the linear fit with the *x* axis. The obtained values were plotted as dependence on laser pulses (the natural logarithm scale), and, again, the linear fit was applied (Fig. 4.46). The ablation threshold for a single pulse was obtained from the intersection of the linear fit with the *y* axis.

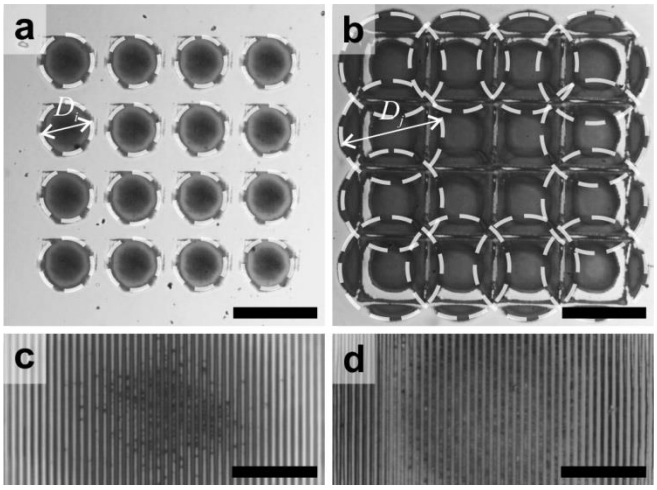

Fig. 4.44. Optical microscope images of DLC-0 sample after irradiation with 50 mJ/cm^2 laser fluence and 1 000 pulses (a, c) and 145 mJ/cm^2 laser fluence and 125 000 pulses (b, d). Mark sizes are: 100 μm (a, b), 15 μm (c, d). Dashed white circles were used for measuring the diameter of the irradiated area. Published in [A4], presented in [B11].

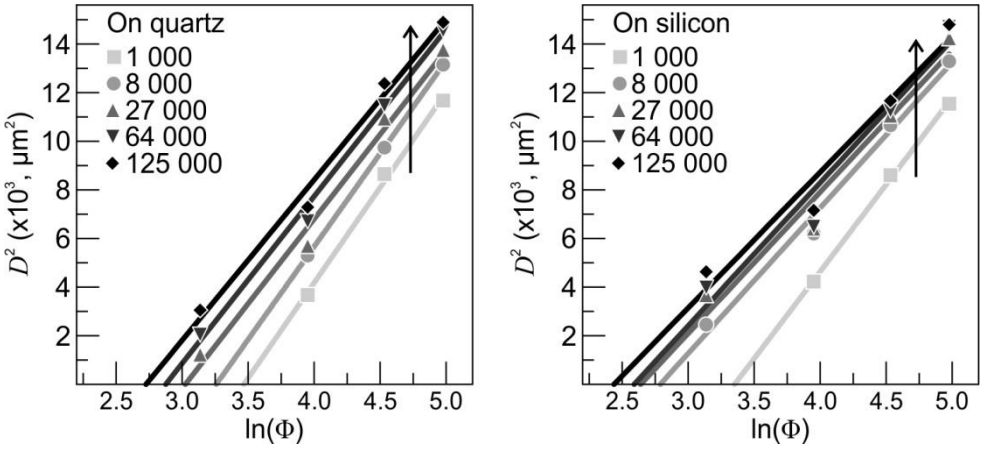

Fig. 4.45. Laser affected area diameter *D* dependence on laser fluence Φ for the DLC-0 sample on quartz and silicon substrates. Different symbols represent different numbers of pulses: square – 1 000, circle – 8 000, up-triangle – 27 000, down-triangle – 64 000, rhombus – 125 000 (the arrow indicates the direction of the increasing number of pulses). Lines are linear fits ($R^2 \geq 0.93$). Published in [A4], presented in [B11].

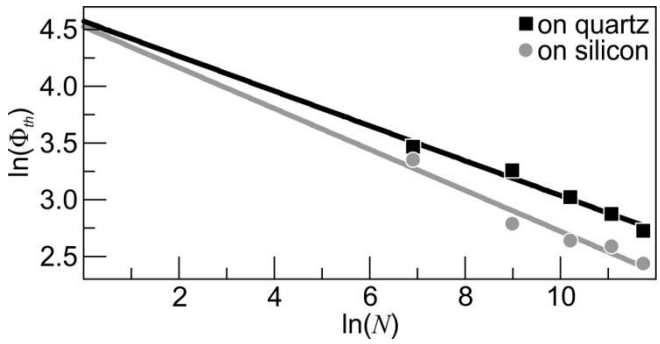

Fig. 4.46. Threshold fluence Φ_{th} dependence on the number of laser pulses N for DLC-0 sample on quartz (black squares) and silicon (grey circles) substrates. The lines are linear fits ($R^2 \geq 0.93$). Published in [A4], presented in [B11].

The summary of the obtained threshold values is presented in Table 4.10. As it can be seen, applying multiple pulses effectively lowered the patterning threshold of DLC:Ag and the ablation threshold of DLC. This is consistent with the incubation effect. The ablation threshold of DLC was lowered up to 8 times if comparing the single pulse and 125 000 pulses. Previously, Di Niso *et al*. reported that the ablation threshold of stainless steel is effectively lowered 4 times by applying 25 000 pulses compared to a single pulse [126]. Even though the tested materials are different, the results are very similar: in our case, the ablation threshold of DLC was lowered approximately 5 times at 27 000 pulses. The incubation effect can be explained by surface modification from multiple pulses which lowers the reflectivity and thus increases the absorbance of laser light [95]. The incubation effect is also present for the patterning threshold as the DLC:Ag patterning threshold was reduced 6–11 times depending on the silver content in the film. This is also indirectly evident from the laser affected lines width analysis when the affected lines become wider with the increased number of pulses. Since patterning does not necessarily require removal of material, the patterning threshold of DLC is lower than its ablation threshold.

Table 4.10. Summary of obtained patterning (DLC:Ag, DLC) and ablation (DLC, Ag) threshold values.

Sample	Threshold fluence (mJ/cm^2) at a certain number of pulses					
	1	1 000	8 000	27 000	64 000	125 000
DLC:Ag-8	N/A[a]	<6	<3	<1	<1	<1
DLC:Ag-14	N/A[a]	<11	<6	<6	<3	<3
DLC-0 on silicon[b]	N/A[a]	<6	<3	<3	<3	<3
DLC-0 on quartz[b]	N/A[a]	>17	>17	<17	<11	<11
DLC-0 on silicon[c]	148	45	26	22	21	18
DLC-0 on quartz[c]	156	51	41	32	28	24
Ag-100	N/A[a]	>145	>145	>145	>145	>145

[a]Due to a different methodology, it was not possible to obtain single pulse threshold values.
[b]Patterning threshold.
[c]Ablation threshold.

By comparing the absorbance of DLC and DLC:Ag samples (Fig. 4.23), it can be noted that DLC has a lower absorbance than DLC:Ag. This suggests that the DLC ablation/patterning threshold should be higher than in the case of DLC:Ag, which is confirmed by comparing the multiple pulses threshold values (Table 4.10). The difference in the DLC:Ag and DLC patterning thresholds is most probably due to LSPR induced effective light absorption in silver nanoparticles as well as because of the field enhancement phenomenon at the silver-DLC interface under intense light irradiation. Stalmashonak *et al*. investigated isolated silver nanoparticles in a glass matrix and noticed that a region of smaller nanoparticles is generated around the main particle after laser irradiation, which was addressed to the electric field exceeding the breakdown of glass, and high-density electron plasma was formed around the metal nanoparticle [188, 189]. In our case, the density of nanoparticles in the nanocomposite was much higher, thus, the particles were able to interact with each other, and no smaller residual particles around the main particle after ablation are observed. This could be explained by immediate redistribution of these particles with the neighbouring ones.

The extrapolated DLC ablation and patterning thresholds are not the same on different substrates (Table 4.10). This can be explained by the difference in the refractive index (at 515 nm $n_{Si} = 4.21$ [190], $n_Q = 1.46$ [191]), reflectivity, and the absorption of the substrates. The obtained ablation threshold values are slightly smaller than those reported by other authors (Table 4.11), but this can be explained by different laser wavelengths because DLC absorbance at 800 nm is lower compared to 515 nm absorbance in our experiments (Fig. 4.23).

Table 4.11. Literature values of single pulse ablation threshold of Ag and DLC.

Material	Ablation threshold (mJ/cm^2)	Laser wavelength (nm)	Laser pulse length	Reference
Ag	1500	800	100 fs	[192]
Ag	820	248	23 ns	[193]
Ag	170-1400[a]	515	200 fs	[194]
DLC	160[b]	800	150 fs	[195]
DLC	243-251	800	120 fs	[196]

[a]Depends on numerical aperture.
[b]The number of applied pulses was not specified in the paper.

By looking at the silver ablation threshold values determined by other authors (Table 4.11), it is apparent that, in this experiment, the maximum applied laser fluence (145 mJ/cm^2) is much lower than the reported ablation thresholds. This explains why the patterning of the silver thin film was not successful. The delamination of the film is caused by the stresses and shockwaves generated by fs-laser irradiation which causes the disruption in the interface of the metal film and substrate [197]. This effect can occur even after a single pulse, and thus subsequent pulses contribute to the patterning of the substrate instead of the silver thin film.

4.2.3. *Size distributions of nanoparticles*

One sample (DLC:Ag-15) was tested under an optical dark-field microscope (Fig. 4.47). The unaffected part of the sample exhibits many different colours (green, red, yellow) which blend into a brown shade. In contrast, the affected part of the sample glows mostly in blueish and purplish colours which make up straight periodic lines. This difference indicates the change in the silver nanoparticles size after laser irradiation.

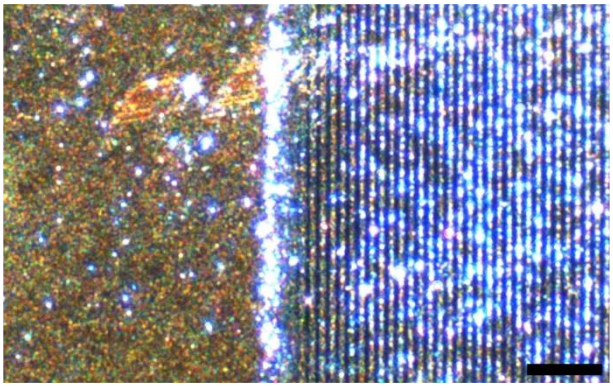

Fig. 4.47. Dark-field microscopy image of DLC:Ag-15 sample: the left side is unaffected, and the right side is patterned by DLIP with Φ = 6 mJ/cm^2 and N = 27 000 pulses. The pitch of the structure is 1306 nm. Mark size is 10 μm.

As the change of the silver nanoparticle size after laser irradiation was already observed in cross-section micrographs (Fig. 4.42) and in a dark-field image (Fig. 4.47), it was decided to systematically analyse the distributions of the particle size in DLC:Ag-8 and DLC:Ag-14 samples. The histograms with their corresponding lognormal fits, as obtained from Equation (3.5), are depicted in Fig. 4.48 (DLC:Ag-8) and Fig. 4.49 (DLC:Ag-14). They show the change in the distribution of nanoparticle sizes after laser irradiation compared to the unaffected (N = 0) samples.

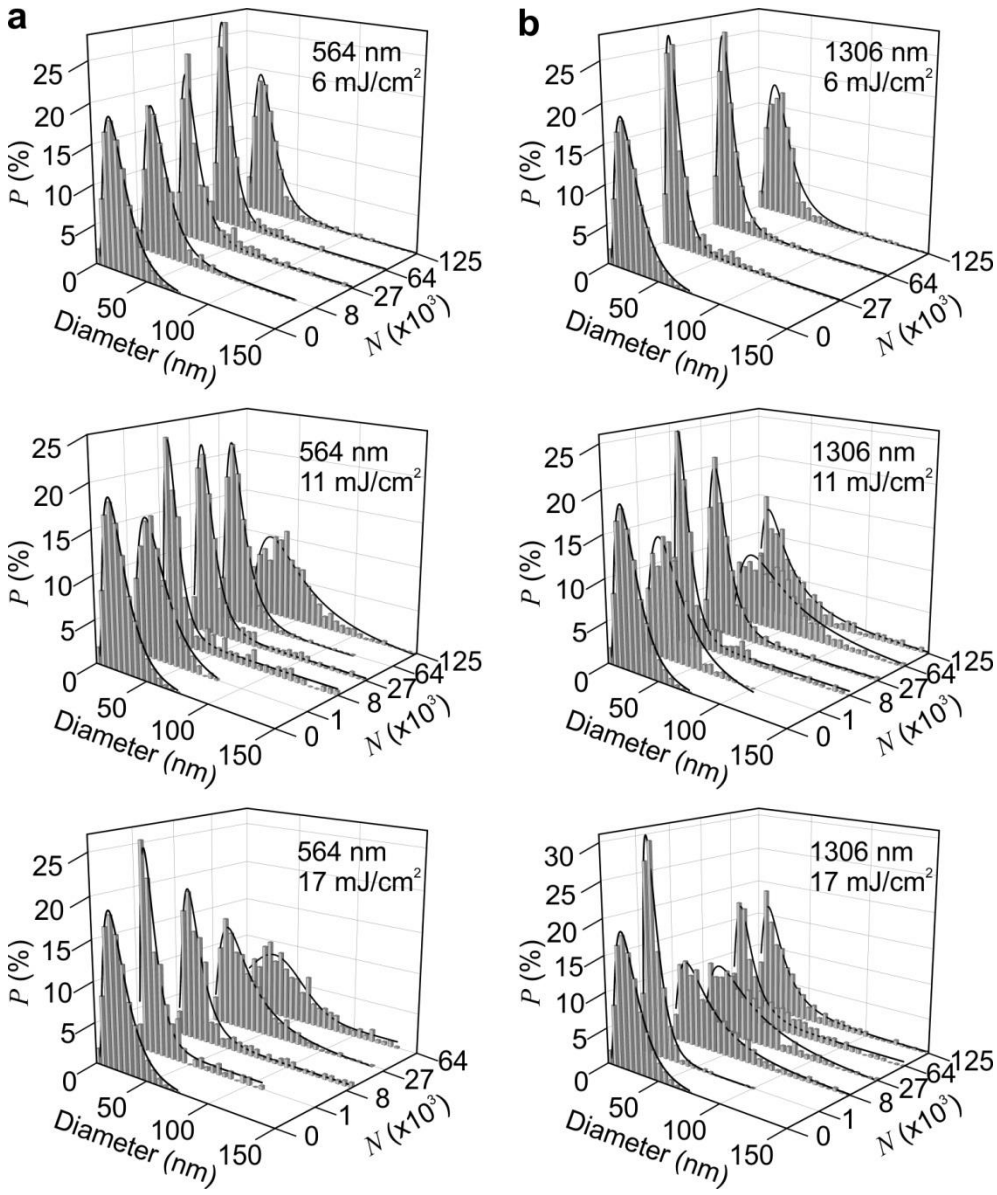

Fig. 4.48. Nanoparticle diameters distributions at 6–17 mJ/cm^2 laser fluence and 0–125 000 number of pulses of DLC:Ag-8 on silicon substrate at 564 nm (a) and 1306 nm (b) pitches. *P* represents a fraction of particles of each diameter compared to all the affected particles at specific energy densities ($R^2 \geq 0.91$). $N = 0$ represents unaffected sample. Published in [A4], presented in [B6, B7, B9, B11].

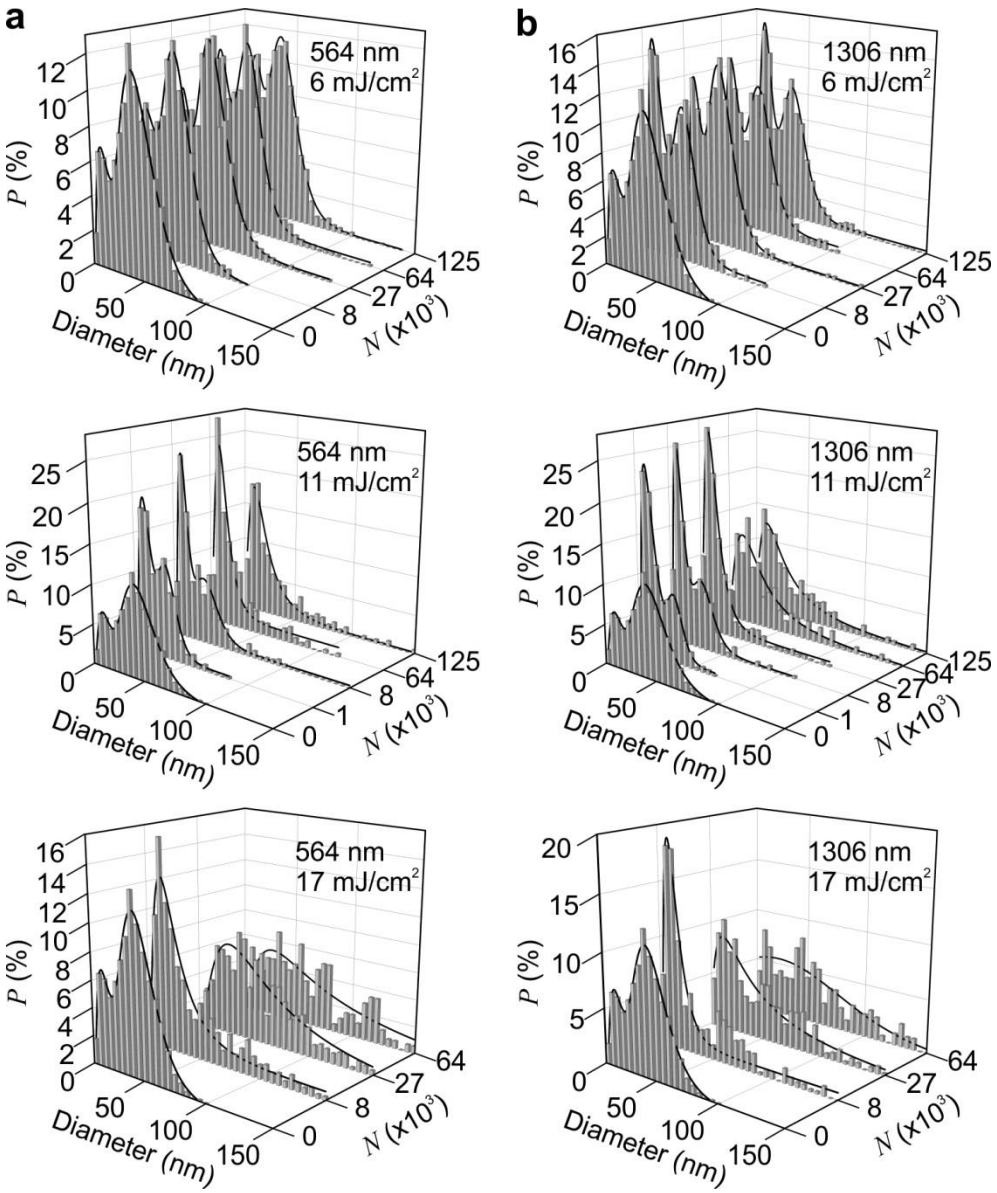

Fig. 4.49. Nanoparticle diameters distributions at 6–17 mJ/cm^2 laser fluence and 0–125 000 number of pulses of DLC:Ag-14 on silicon substrate at 564 nm (a) and 1306 nm (b) pitches. *P* represents a fraction of particles of each diameter compared to all the affected particles at specific energy densities ($R^2 \geq 0.76$). $N = 0$ represents unaffected sample. Published in [A4], presented in [B11].

After the investigation of pristine samples (Fig. 4.17), it was observed that DLC:Ag-8 is denoted by unimodal distribution with the central diameter of 24 nm, while DLC:Ag-14 exhibits bimodal distribution with the central diameters of 17 nm and 46 nm. The change of the central diameters after laser irradiation (from Fig. 4.48 and Fig. 4.49) is summarised in Fig. 4.50. DLC:Ag-8 nanoparticle distribution

remains unimodal at any laser irradiation level. However, the bimodal nature of DLC:Ag-14 is changed into unimodal distribution after irradiation with $\Phi = 11$ mJ/cm^2, $N = 27\,000$. At 17 mJ/cm^2 laser fluence, it also becomes unimodal. For both silver concentrations, the central diameter x_c of the distribution shifts towards the larger particles with the increasing laser fluence, which indicates agglomeration or removal of smaller particles. At the same time, the particle density after laser irradiation is reduced up to 7 times compared to pristine samples, which backs-up the theory of agglomeration and removal. However, at a lower number of the applied pulses, the central diameter is lower than in pristine samples, which suggests fragmentation. It can be concluded that, initially, the particles are fragmented, but, later, agglomeration takes place, and, finally, removal (ablation) is observed. This is summarized in Fig. 4.51. Also, at the highest energy levels, the nanoparticles size distribution (Fig. 4.49) widens significantly, which indicates the presence of variously sized particles. Stietz *et al*. presented the possibility to tailor the nanoparticle shape by intense laser light in order to achieve a uniform distribution, which is feasible with thermal and non-thermal effects [198]. With this work, it was proved that homogenization is possible not only for nanoparticles on a substrate, but also in a matrix, i.e., for nanocomposites.

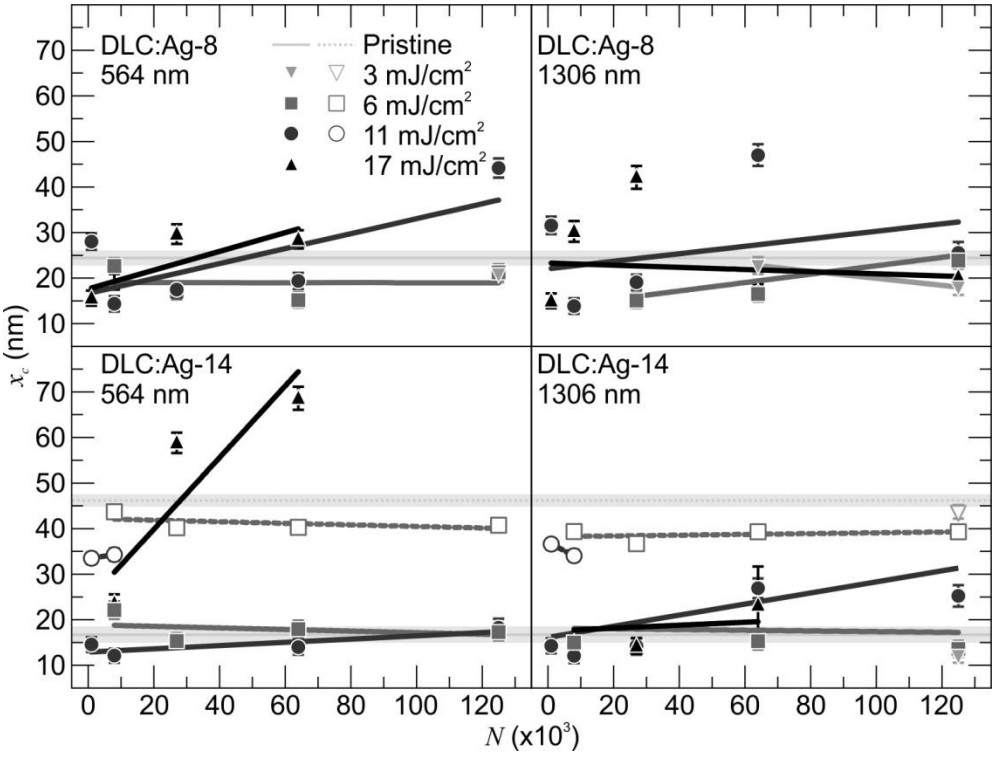

Fig. 4.50. Central diameter x_c of silver nanoparticles dependence on the number of applied pulses N for DLC:Ag-8 and DLC:Ag-14 in 564 nm and 1306 nm pitches at 3–17 mJ/cm^2. The pristine (unaffected sample parts) values are horizontal lines with shaded area. Empty symbols and dashed lines represent the second peak characteristic to DLC:Ag-14. The lines only serve as guides for the eyes. Published in [A4].

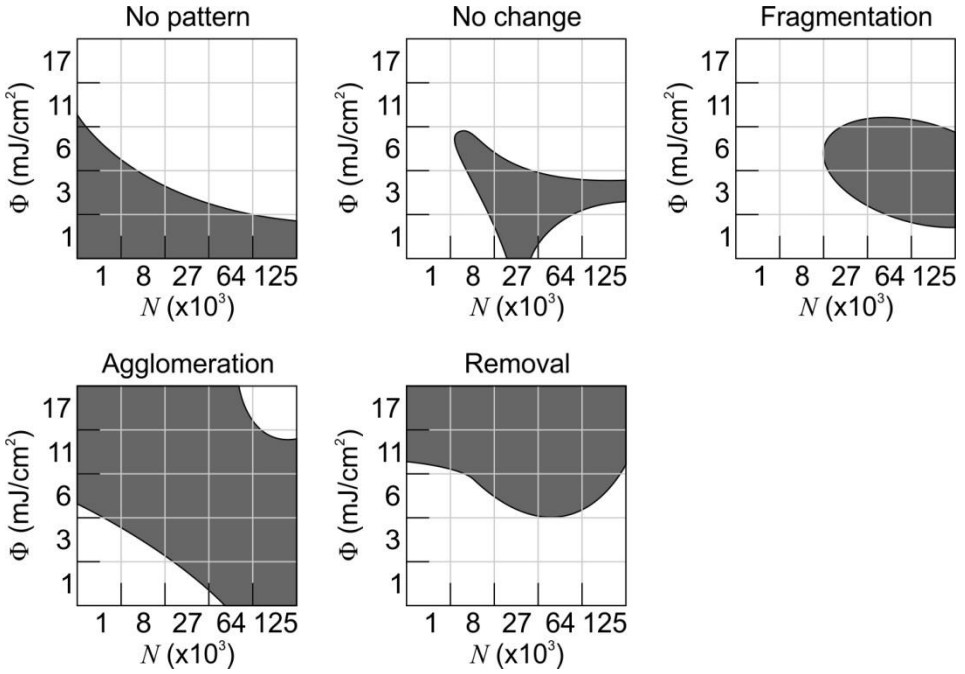

Fig. 4.51. Schematic illustration of the possible changes of silver nanoparticles in DLC:Ag-8 and DLC:Ag-14 nanocomposites after laser irradiation by various energy densities. Presented in [B11].

It is reported that the plasmonic heating effect is capable of the manipulation of nanoparticles, e.g., embedding in a matrix, controlling of atomic switches [52, 199, 200], etc. In the present work, the applied energy density was much higher, and the particles were not only heated, but also manipulated into a different shape. Thus, the heating effect can partly explain agglomeration. Another possible reason for agglomeration is the Ostwald ripening mechanism: the process of dissolution of smaller particles and the growth of larger particles at the expense of the smaller particles [201]. This phenomenon was observed in plasma etching of DLC:Ag with selective removal of the matrix [77]. Thus, it is very likely that Ostwald ripening also occurs for laser irradiated samples.

4.2.4. *Ellipsometric mapping of laser irradiated areas*

As it was proven in the previous chapter, laser irradiation changes the size of nanoparticles. Furthermore, the optical properties of nanocomposites depend on the size of nanoparticles. The change in these properties can be investigated by spectroscopic ellipsometry. Instead of the usual ellipsometric measurement which was not possible due to the small size of the affected zones, the ellipsometric map was obtained for the laser irradiated areas and their vicinity. The mapping of the DLC:Ag-8 sample was performed in two orientations with the plane of incident light perpendicular or parallel to the orientation of lines in the periodic pattern (Fig. 4.52). This was done in order to test the diffraction effect on ellipsometric parameters.

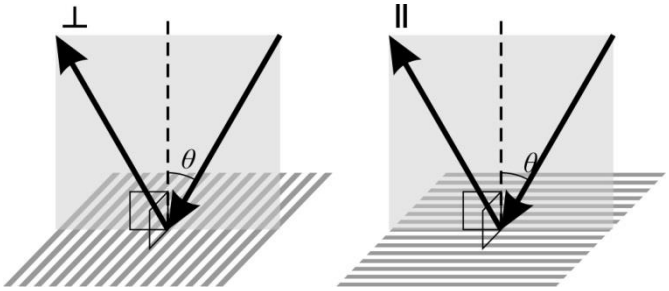

Fig. 4.52. Schematic illustration of the periodic lines orientation in respect to the plane of incident light for ellipsometry mapping: perpendicular to the lines of periodic pattern (⊥) and parallel (∥).

The ellipsometric parameters map of DLC:Ag-8 is depicted in Fig. 4.53. The different orientations of periodic lines with respect to the plane of incidence light do not show any significant differences when comparing Fig. 4.53 top (perpendicular ⊥) and bottom (parallel ∥) images. In the parallel direction, the tan(Ψ) map exhibits a slightly higher contrast of the irradiated areas, and the rows of 3–6 mJ/cm^2 are better visible. The other difference is the elongation of the squares in different directions. This is caused by this specific spectroscopic ellipsometry system because the microspot used for measurements is not symmetrical: it is approximately 1.3 times larger in one direction than in the other. Since the parallel and perpendicular directions did not show any significant differences, the DLC:Ag-14 sample was measured only in the perpendicular orientation. The corresponding DLC:Ag-14 SE map is depicted in Fig. 4.54.

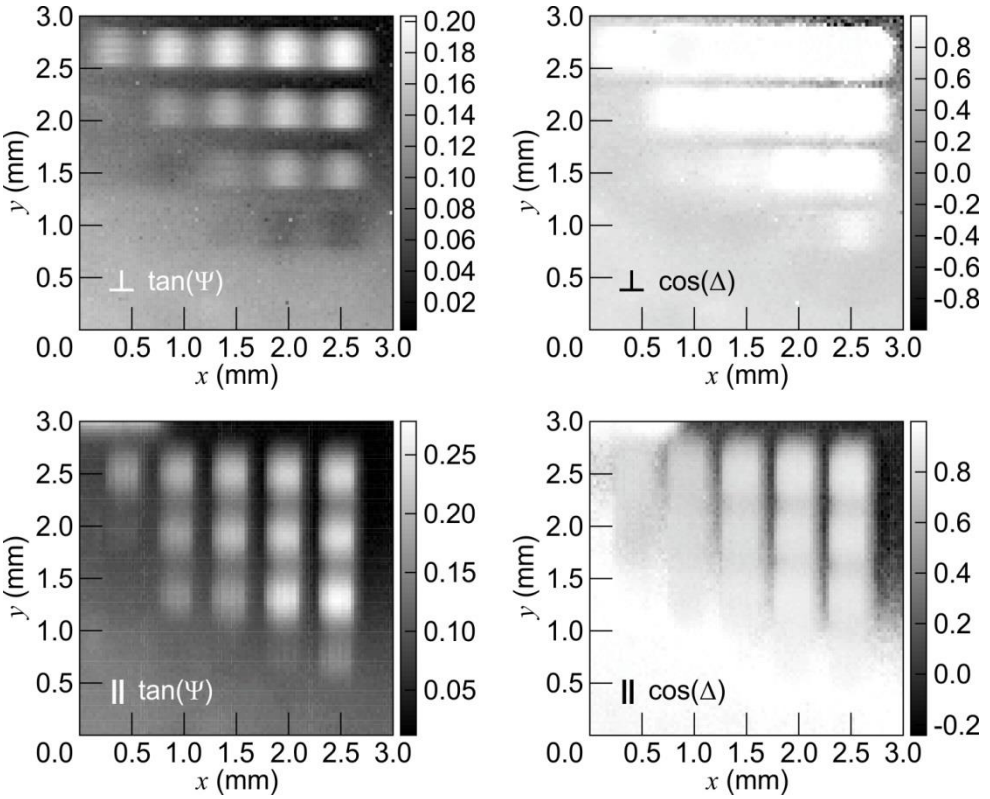

Fig. 4.53. Ellipsometric mapping of DLC:Ag-8 on quartz substrate. The maps were obtained at two different sample orientations: the plane of incidence perpendicular to the lines of periodic pattern (⊥) and parallel (‖) to them. The map of tan(Ψ) (⊥) was obtained at 813.7 nm wavelength, tan(Ψ) (‖) at 794.4 nm, while cos(Δ) (⊥) was obtained at 809.0 nm, cos(Δ) (‖) at 721.6 nm. The bright squares are laser affected areas with the laser fluence increasing from bottom (3 mJ/cm^2) to top (17 mJ/cm^2), and the number of pulses increasing from left (1 000) to right (125 000). The areas affected with 1 mJ/cm^2 are not visible. Presented in [B8, B10].

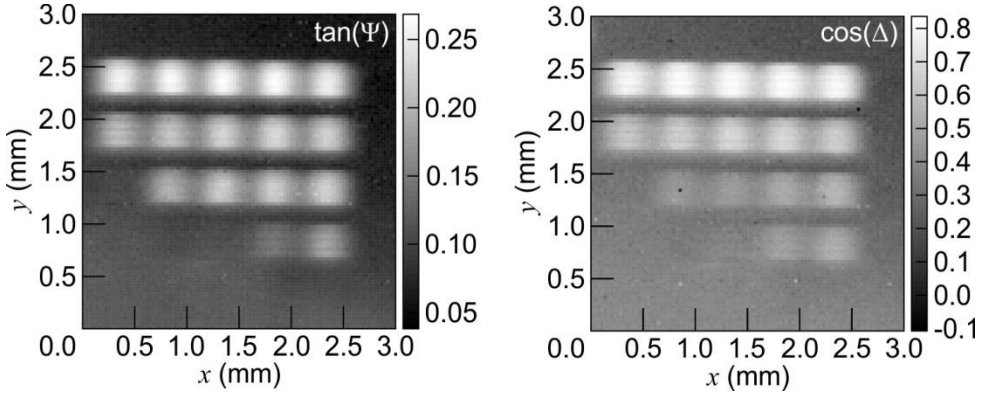

Fig. 4.54. Ellipsometric mapping of DLC:Ag-14 on quartz substrate. The map of tan(Ψ) was obtained at 679.1 nm wavelength, while cos(Δ) was obtained at 587.0 nm. The bright squares

are laser affected areas with the laser fluence increasing from bottom (3 mJ/cm^2) to top (17 mJ/cm^2), and the number of pulses increasing from left (1 000) to right (125 000). The areas affected with 1 mJ/cm^2 are not visible. Presented in [B8, B10].

In all ellipsometric maps of both DLC:Ag-8 and DLC:Ag-14, the laser affected areas are clearly visible, however, tan(Ψ) – related to the light intensity ratio – seems to be more sensitive because the affected areas have a higher contrast with the surrounding unaffected parts of the sample than in the cos(Δ) – related to phase difference – case. When increasing laser irradiation parameters (either the laser fluence or the number of the applied pulses), the contrast of the irradiated areas slightly increased when compared to the unaffected parts. The map of cos(Δ) of DLC:Ag-8 (the right part of Fig. 4.53) is not a good representation of laser effects because all the values are very similar, and it is impossible to distinguish between the squares affected by a different number of pulses. However, this cos(Δ) map perfectly shows the non-uniformity in the thin film: the optical properties gradually change from the lower left to the top right corner. If the film was more uniform, a better cos(Δ) contrast of the affected areas can be expected as in the case of DLC:Ag-14 (the right part of Fig. 4.54). This non-uniformity can be caused by different thickness of the film, which was already suspected from SE fitting (Table 4.7), or from changes in the silver concentration.

The spectroscopic ellipsometry map (Fig. 4.54) can be compared to the optical microscope image (Fig. 4.55). This image is a composite of 4 images and shows approximately the same area as the ellipsometry map. Visually, the SE map is very similar to what can be seen under optical microscope: with the increasing laser fluence, the contrast of the squares increases. The areas affected by the lowest laser fluence (1 mJ/cm^2) are not visible as well as 3 mJ/cm^2 fluence, 1 000–8 000 pulses. It appears that the areas affected by 3 mJ/cm^2 fluence, 27 000 pulses and 6 mJ/cm^2 fluence, 1 000 pulses are slightly visible in the optical microscope image, but not in the ellipsometry map. However, choosing a different wavelength for the mapping could yield a different result, and these areas could actually be resolved at the expense of the contrast of other areas.

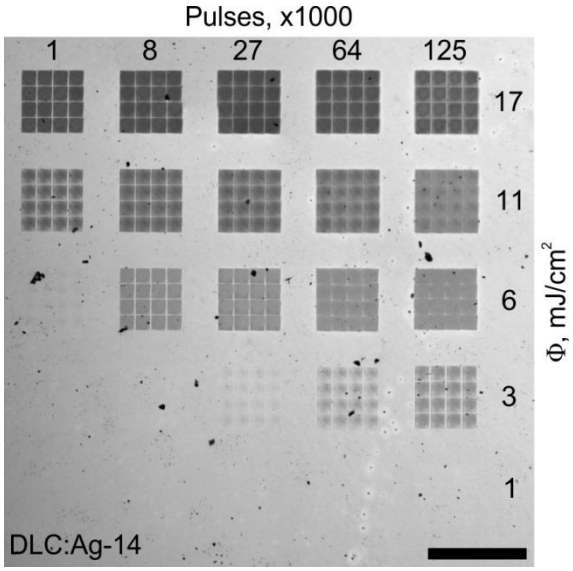

Fig. 4.55. Optical microscope composite image of DLC:Ag-14 sample on quartz substrate. The mark size is 500 μm. Presented in [B10].

Mapping by using a spectroscopic ellipsometer with an automatic sample stage and further filtering of the results takes a lot of time. In addition, the resolution of the final image is limited by the beam size. It would be more convenient to use an imaging ellipsometer specifically designed for the mapping of ellipsometric parameters. The imaging ellipsometer is a combination of a laser ellipsometer and a microscope, which gives a better resolution of the image with faster acquisition times. However, imaging ellipsometry is limited to a single wavelength. Thus, spectroscopic ellipsometry is advantageous over imaging ellipsometry due to the multiwavelength spectrum. It enables investigation of any material even when the highest sensitivity wavelength is unknown.

4.2.5. *Two-photon luminescence of laser irradiated area*

TPL (Fig. 4.56) was performed on two samples (DLC:Ag-14 and DLC:Ag-15) when using different systems as described in the Two-photon luminescence chapter. In both cases, the TPL signal was strong enough, and even the periodic lines in the patterns were clearly distinguished. More than a year passed between the deposition of the DLC:Ag-15 thin film and the TPL measurements, and, in that time, the sample was stored in ambient conditions. As it can be seen from the signal of the unaffected area (Fig. 4.56a, bottom), the TPL intensity is still sufficient. Thus, it can be concluded that the DLC matrix effectively protected silver nanoparticles from oxidation. When comparing TPL signal in Fig. 4.56b, it appears that the width of the bright lines (representing the unaffected parts of the sample) slightly decreases with the increasing number of pulses, as it was already detected from the analysis of SEM micrographs (Fig. 4.43).

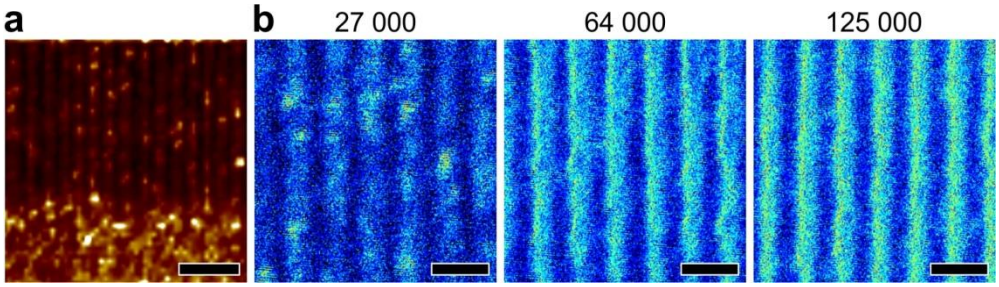

Fig. 4.56. Two-photon luminescence images: a) of DLC:Ag-15, unknown location on the sample, obtained with the system from [40]. Mark size is 5 μm; b) of DLC:Ag-14 affected with 17 mJ/cm^2 and specified pulses, 1306 nm pitch, obtained with the system from [165]. Mark size is 2 μm.

5. CONCLUSIONS

1) The nanocomposite thin film of diamond-like carbon with copper nanoparticles tends to grow as a multilayered structure with alternating carbon- and copper-rich layers. This structuring can effectively be resolved in X-ray reflectivity and spectroscopic ellipsometry by creating varying copper concentration multilayered models for the interpretation of experimental data. The models are in good agreement with transmission electron microscopy and energy dispersive X-ray spectroscopy results. Contrary to copper containing films, diamond-like carbon with silver nanoparticles nanocomposites tends to form nanoparticles more on top of the film. Silver is susceptible to oxidation and sulfurization, but the two-photon luminescence signal shows that the plasmonic properties are preserved for a long time.
2) In spectroscopic ellipsometry fitting, the optical model best fits the experimental data when diamond-like carbon is described by the Cody-Lorentz dispersion law, and the nanocomposite is described by Bruggeman effective medium approximation. The obtained dielectric functions of copper (from 27.4 at.%) and silver (all concentrations) containing nanocomposites show features in the dielectric functions at 600 nm and 330 nm wavelengths, respectively, related to the plasmonic properties of these metals.
3) Holographic lithography is a convenient technique for the patterning of photosensitive materials and is capable of imposing one-dimensional and two-dimensional periodic patterns with different symmetry and point lattice types. Unique structures can be predicted by modelling the interference field while taking into account the number of laser beams, their polarizations, the number of exposures, and the angle of incidence. The diffraction pattern of the fabricated structures can be visualised by taking a fast Fourier transformation of microscopy image of the corresponding structure.
4) It was proven that direct laser interference patterning is a versatile and efficient method to create sub-micrometre range periodic lines in the diamond-like carbon matrix doped with silver nanoparticles. By changing the applied energy density, the line widths of 150–420 nm (for 564 nm pitch) and 400–960 nm (for 1306 nm pitch) were obtained.
5) Femtosecond laser irradiation is also effective for changing the nanoparticle size distributions in already deposited nanocomposite thin films. The initial bimodal distribution with the central diameters of 17 nm and 46 nm of 14.1 at.% silver in diamond-like carbon was successfully changed into unimodal with central diameters ranging from 14 nm (11 mJ/cm^2 laser fluence, 64 000 pulses) to 69 nm (17 mJ/cm^2 laser fluence, 64 000 pulses). The initial nanoparticle diameter unimodal distribution of the thin film with 7.9 at.% silver in diamond-like carbon (the central diameter is equal to 24 nm) is maintained after laser irradiation, but with the change in the central diameter: it is tailored from 13 nm (11 mJ/cm^2 laser fluence, 8 000 pulses) to 44 nm (11 mJ/cm^2 laser fluence, 125 000 pulses).

6) The difference in absorption of diamond-like carbon and its nanocomposites with silver nanoparticles as well as the local field enhancement governed by localized surface plasmon resonance due to metallic nanoparticles are the main reasons for the reduction of the patterning threshold in nanocomposite. In order to pattern the nanocomposite, the required energy density is from 4 times (at 1 000 pulses) up to 24 times (at 125 000 pulses) lower than for nanocomposites components separately (diamond-like carbon and silver).
7) Nanocomposite patterning does not require the removal of material: the pattern is also obtained with slight modifications of the nanoparticle sizes. The process occurs at laser fluences at or above the patterning threshold. By further increasing the laser fluence above the ablation threshold, patterns with removed particles are obtained. Two-dimensional fast Fourier transformations of microscopy images are a fast and reliable way to test the quality of the patterned structures even when the pattern is not yet clearly expressed in the micrograph.
8) Spectroscopic ellipsometry mapping reveals the impact of laser irradiation: the higher applied fluence or the higher number of pulses result in a higher contrast of the ellipsometric parameters when comparing the affected and unaffected areas.

REFERENCES

1. WEST, Paul R., ISHII, Satoshi, NAIK, Gururaj V., EMANI, Naresh K., SHALAEV, Vladimir M. and BOLTASSEVA, Alexandra. Searching for better plasmonic materials. *Laser and Photonics Reviews*. 2010. Vol. 4, no. 6, p. 795–808. DOI 10.1002/lpor.200900055.
2. WADELL, Carl, NUGROHO, Ferry Anggoro Ardy, LIDSTRÖM, Emil, IANDOLO, Beniamino, WAGNER, Jakob B. and LANGHAMMER, Christoph. Hysteresis-free nanoplasmonic Pd-Au alloy hydrogen sensors. *Nano Letters*. 2015. Vol. 15, no. 5, p. 3563–3570. DOI 10.1021/acs.nanolett.5b01053.
3. RIFAT, Ahmmed A., MAHDIRAJI, G. Amouzad, CHOW, Desmond M., SHEE, Yu Gang, AHMED, Rajib and ADIKAN, Faisal Rafiq Mahamd. Photonic crystal fiber-based surface plasmon resonance sensor with selective analyte channels and graphene-silver deposited core. *Sensors*. 2015. Vol. 15, no. 5, p. 11499–11510. DOI 10.3390/s150511499.
4. SCHMIDL, G., DELLITH, J., SCHNEIDEWIND, H., ZOPF, D., STRANIK, O., GAWLIK, A., ANDERS, S., TYMPEL, V., KATZER, C., SCHMIDL, F. and FRITZSCHE, W. Formation and characterization of silver nanoparticles embedded in optical transparent materials for plasmonic sensor surfaces. *Materials Science and Engineering B: Solid-State Materials for Advanced Technology*. 2015. Vol. 193, no. C, p. 207–216. DOI 10.1016/j.mseb.2014.12.001.
5. SUGAWA, Kosuke, TAHARA, Hironobu, YAMASHITA, Ayane, OTSUKI, Joe, SAGARA, Takamasa, HARUMOTO, Takashi and YANAGIDA, Sayaka. Refractive index susceptibility of the plasmonic palladium nanoparticle: Potential as the third plasmonic sensing material. *ACS Nano*. 2015. Vol. 9, no. 2, p. 1895–1904. DOI 10.1021/nn506800a.
6. BAGHERI, Shahin, STROHFELDT, Nikolai, UBL, Monika, BERRIER, Audrey, MERKER, Michael, RICHTER, Gunther, SIEGEL, Michael and GIESSEN, Harald. Niobium as Alternative Material for Refractory and Active Plasmonics. *ACS Photonics*. 2018. Vol. 5, no. 8, p. 3298–3304. DOI 10.1021/acsphotonics.8b00530.
7. LALISSE, Adrien, TESSIER, Gilles, PLAIN, Jérome and BAFFOU, Guillaume. Quantifying the Efficiency of Plasmonic Materials for Near-Field Enhancement and Photothermal Conversion. *Journal of Physical Chemistry C*. 2015. Vol. 119, no. 45, p. 25518–25528. DOI 10.1021/acs.jpcc.5b09294.
8. WANG, Yu, CAPRETTI, Antonio and DAL NEGRO, Luca. Wide tuning of the optical and structural properties of alternative plasmonic materials. *Optical Materials Express*. 2015. Vol. 5, no. 11, p. 2415. DOI 10.1364/ome.5.002415.
9. STERL, Florian, STROHFELDT, Nikolai, WALTER, Ramon, GRIESSEN, Ronald, TITTL, Andreas and GIESSEN, Harald. Magnesium as novel material for active plasmonics in the visible wavelength range. *Nano Letters*. 2015. Vol. 15, no. 12, p. 7949–7955. DOI 10.1021/acs.nanolett.5b03029.

10. ZENG, Shuwen, SREEKANTH, Kandammathe Valiyaveedu, SHANG, Jingzhi, YU, Ting, CHEN, Chih Kuang, YIN, Feng, BAILLARGEAT, Dominique, COQUET, Philippe, HO, Ho Pui, KABASHIN, Andrei V. and YONG, Ken Tye. Graphene-Gold Metasurface Architectures for Ultrasensitive Plasmonic Biosensing. *Advanced Materials*. 2015. Vol. 27, no. 40, p. 6163–6169. DOI 10.1002/adma.201501754.
11. WADELL, Carl, SYRENOVA, Svetlana and LANGHAMMER, Christoph. Plasmonic hydrogen sensing with nanostructured metal hydrides. *ACS Nano*. 2014. Vol. 8, no. 12, p. 11925–11940. DOI 10.1021/nn505804f.
12. DAS, G., COLUCCIO, M. L., ALRASHEED, S., GIUGNI, A., ALLIONE, M., TORRE, B., PEROZZIELLO, G., CANDELORO, P. and DI FABRIZIO, E. Plasmonic nanostructures for the ultrasensitive detection of biomolecules. *Rivista del Nuovo Cimento*. 2016. Vol. 39, no. 11, p. 547–586. DOI 10.1393/ncr/i2016-10129-y.
13. THØGERSEN, Annett, BONSAK, Jack, FOSLI, Carl Huseby and MUNTINGH, Georg. Size distributions of chemically synthesized Ag nanocrystals. *Journal of Applied Physics*. 2011. Vol. 110, no. 4, p. 044306. DOI 10.1063/1.3609077.
14. PALERMO, Giovanna, RITACCO, Tiziana, ACETI, Dante, PEZZI, Luigia, GIOCONDO, Michele and DE LUCA, Antonio. Photo-Thermal Effects in 1D Gratings of Gold Nanoparticles. *Crystals*. 2017. Vol. 7, no. 12, p. 14. DOI 10.3390/cryst7010014.
15. MALASI, A., SACHAN, R., RAMOS, V., GARCIA, H., DUSCHER, G. and KALYANARAMAN, R. Localized surface plasmon sensing based investigation of nanoscale metal oxidation kinetics. *Nanotechnology*. 2015. Vol. 26, no. 20, p. 205701. DOI 10.1088/0957-4484/26/20/205701.
16. GWO, Shangjr, WANG, Chun Yuan, CHEN, Hung Ying, LIN, Meng Hsien, SUN, Liuyang, LI, Xiaoqin, CHEN, Wei Liang, CHANG, Yu Ming and AHN, Hyeyoung. Plasmonic Metasurfaces for Nonlinear Optics and Quantitative SERS. *ACS Photonics*. 2016. Vol. 3, no. 8, p. 1371–1384. DOI 10.1021/acsphotonics.6b00104.
17. OOMS, Matthew D., JEYARAM, Yogesh and SINTON, David. Disposable plasmonics: Rapid and inexpensive large area patterning of plasmonic structures with CO_2 laser annealing. *Langmuir*. 2015. Vol. 31, no. 18, p. 5252–5258. DOI 10.1021/acs.langmuir.5b01092.
18. MCPEAK, Kevin M., JAYANTI, Sriharsha V., KRESS, Stephan J.P., MEYER, Stefan, IOTTI, Stelio, ROSSINELLI, Aurelio and NORRIS, David J. Plasmonic films can easily be better: Rules and recipes. *ACS Photonics*. 2015. Vol. 2, no. 3, p. 326–333. DOI 10.1021/ph5004237.
19. KRAVETS, V. G., KABASHIN, A. V., BARNES, W. L. and GRIGORENKO, A. N. Plasmonic Surface Lattice Resonances: A Review of Properties and Applications. *Chemical Reviews*. 2018. Vol. 118, no. 12, p. 5912–5951. DOI 10.1021/acs.chemrev.8b00243.
20. ASMUSSEN, Silvana V., ARENAS, Gustavo F. and VALLO, Claudia I. Enhanced degree of polymerization of methacrylate and epoxy resins by

plasmonic heating of embedded silver nanoparticles. *Progress in Organic Coatings*. 2015. Vol. 88, p. 220–227. DOI 10.1016/j.porgcoat.2015.06.032.
21. SELLAPPAN, Raja, NIELSEN, Morten G., GONZÁLEZ-POSADA, Fernando, VESBORG, Peter C.K., CHORKENDORFF, Ib and CHAKAROV, Dinko. Effects of plasmon excitation on photocatalytic activity of Ag/TiO_2 and Au/TiO_2 nanocomposites. *Journal of Catalysis*. 2013. Vol. 307, p. 214–221. DOI 10.1016/j.jcat.2013.07.024.
22. VERBRUGGEN, Sammy W., KEULEMANS, Maarten, GORIS, Bart, BLOMMAERTS, Natan, BALS, Sara, MARTENS, Johan A. and LENAERTS, Silvia. Plasmonic 'rainbow' photocatalyst with broadband solar light response for environmental applications. *Applied Catalysis B: Environmental*. 2016. Vol. 188, no. 2016, p. 147–153. DOI 10.1016/j.apcatb.2016.02.002.
23. GAO, Minmin, CONNOR, Peh Kang Nuo and HO, Ghim Wei. Plasmonic photothermic directed broadband sunlight harnessing for seawater catalysis and desalination. *Energy and Environmental Science*. 2016. Vol. 9, no. 10, p. 3151–3160. DOI 10.1039/c6ee00971a.
24. BARBILLON, Grégory. Fabrication and SERS Performances of Metal/Si and Metal/ZnO Nanosensors: A Review. *Coatings*. 30 January 2019. Vol. 9, no. 2, p. 86. DOI 10.3390/coatings9020086.
25. PELÁEZ, R. J., FERRERO, A., SKEREN, M., BERNAD, B. and CAMPOS, J. Customizing plasmonic diffraction patterns by laser interference. *RSC Advances*. 2017. Vol. 7, no. 48, p. 30118–30127. DOI 10.1039/C7RA02878D.
26. LIU, Peisheng, WANG, Hao, LI, Xiaoming, RUI, Muchen and ZENG, Haibo. Localized surface plasmon resonance of Cu nanoparticles by laser ablation in liquid media. *RSC Advances*. 2015. Vol. 5, no. 97, p. 79738–79745. DOI 10.1039/c5ra14933a.
27. XUE, Yingxian, DING, Chengjie, RONG, Youying, MA, Qiang, PAN, Chengda, WU, E., WU, Botao and ZENG, Heping. Tuning Plasmonic Enhancement of Single Nanocrystal Upconversion Luminescence by Varying Gold Nanorod Diameter. *Small*. 2017. Vol. 13, no. 36, p. 1–11. DOI 10.1002/smll.201701155.
28. KRAVETS, V. G., JALIL, R., KIM, Y.-J., ANSELL, D., AZNAKAYEVA, D. E., THACKRAY, B., BRITNELL, L., BELLE, B. D., WITHERS, F., RADKO, I. P., HAN, Z., BOZHEVOLNYI, Sergey I., NOVOSELOV, K. S., GEIM, A. K. and GRIGORENKO, A. N. Graphene-protected copper and silver plasmonics. *Scientific Reports*. 2015. Vol. 4, no. 1, p. 5517. DOI 10.1038/srep05517.
29. CHAN, George H., ZHAO, Jing, HICKS, Erin M., SCHATZ, George C. and VAN DUYNE, Richard P. Plasmonic properties of copper nanoparticles fabricated by nanosphere lithography. *Nano Letters*. 2007. Vol. 7, no. 7, p. 1947–1952. DOI 10.1021/nl070648a.
30. GU, Kunming, ZHENG, Yi, LUO, Junxuan, QIN, Xiande, YANG, Xinge, ABBAS, Nadeem and TANG, Jiaoning. Microstructure, mechanical and

tribological properties of DLC/Cu-DLC/W-DLC composite films on SUS304 stainless steel substrates. *Materials Research Express*. 3 May 2019. Vol. 6, no. 8, p. 086406. [Accessed 8 July 2019]. DOI 10.1088/2053-1591/ab197b.

31. RUIZ, Facundo, JASSO, M.E. Compeán, GUAJARDO-PACHECO, Jesús, MARTÍNEZ-CASTAÑÓN, Gabriel-Alejandro, MORALES-SÁNCHEZ, Elpidio and ARAUJO-MARTÍNEZ, Rene. Antimicrobial Properties of Copper Nanoparticles and Amino Acid Chelated Copper Nanoparticles Produced by Using a Soya Extract. *Bioinorganic Chemistry and Applications*. 2017. Vol. 2017, p. 1064918. DOI 10.1155/2017/1064918.
32. MEŠKINIS, GUDAITIS, R., VASILIAUSKAS, A., ČIEGIS, A., ŠLAPIKAS, K., TAMULEVIČIUS, T., ANDRULEVIČIUS, M. and TAMULEVIČIUS, S. Piezoresistive properties of diamond like carbon films containing copper. *Diamond and Related Materials*. 2015. Vol. 60, p. 20–25. DOI 10.1016/j.diamond.2015.10.007.
33. SADEQ, Sinan Abdulhameed, AL-HAYALI, Sarah Kadhim, HARUN, Sulaiman Wadi and AL-JANABI, Abdulhadi. Copper oxide nanomaterial saturable absorber as a new passive Q-switcher in erbium-doped fiber laser ring cavity configuration. *Results in Physics*. 2018. Vol. 10, no. April, p. 264–269. DOI 10.1016/j.rinp.2018.06.006.
34. ZHANG, Yangxi, ZHANG, Qiang, OUYANG, Xia, LEI, Dang Yuan, ZHANG, A. Ping and TAM, Hwa Yaw. Ultrafast Light-Controlled Growth of Silver Nanoparticles for Direct Plasmonic Color Printing. *ACS Nano*. 2018. Vol. 12, no. 10, p. 9913–9921. DOI 10.1021/acsnano.8b02868.
35. VOGEL, Florian, HUBENTHAL, Frank and TRÄGER, Frank. Tailoring the shape of colloidal gold particles with nanosecond-pulsed laser light. *Proceedings SPIE 6324, Plasmonics: Nanoimaging, Nanofabrication, and their Applications II*. 2006. Vol. 6324, p. 63240G. DOI 10.1117/12.680339.
36. PECKUS, Domantas, RONG, Hongpan, STANKEVIČIUS, Lukas, JUODĖNAS, Mindaugas, TAMULEVIČIUS, Sigitas, TAMULEVIČIUS, Tomas and HENZIE, Joel. Hot Electron Emission Can Lead to Damping of Optomechanical Modes in Core − Shell Ag@TiO2 Nanocubes. *The Journal of Physical Chemistry C*. 2017. Vol. 121, p. 24159–24167. DOI 10.1021/acs.jpcc.7b06667.
37. BUTUN, Serkan, TONGAY, Sefaattin and AYDIN, Koray. Enhanced Light Emission from Large-Area Monolayer MoS2 Using Plasmonic Nanodisc Arrays. *Nano Letters*. 2015. Vol. 15, no. 4, p. 2700–2704. DOI 10.1021/acs.nanolett.5b00407.
38. JUODĖNAS, Mindaugas, TAMULEVIČIUS, Tomas, HENZIE, Joel, ERTS, Donats and TAMULEVIČIUS, Sigitas. Surface Lattice Resonances in Self-Assembled Arrays of Monodisperse Ag Cuboctahedra. *ACS Nano*. 2019. Vol. 13, no. 8, p. 9038–9047. DOI 10.1021/acsnano.9b03191.
39. RYCENGA, Matthew, COBLEY, Claire M., ZENG, Jie, LI, Weiyang, MORAN, Christine H., ZHANG, Qiang, QIN, Dong and XIA, Younan. Controlling the synthesis and assembly of silver nanostructures for plasmonic applications. *Chemical Reviews*. 2011. Vol. 111, no. 6, p. 3669–3712.

DOI 10.1021/cr100275d.
40. NOVIKOV, Sergey M., POPOK, Vladimir N., EVLYUKHIN, Andrey B., HANIF, Muhammad, MORGEN, Per, FIUTOWSKI, Jacek, BEERMANN, Jonas, RUBAHN, Horst Günter and BOZHEVOLNYI, Sergey I. Highly Stable Monocrystalline Silver Clusters for Plasmonic Applications. *Langmuir*. 2017. Vol. 33, no. 24, p. 6062–6070. DOI 10.1021/acs.langmuir.7b00772.
41. TUMKUR, T., BARNAKOV, Y., KEE, S. T., NOGINOV, M. A. and LIBERMAN, V. Permittivity evaluation of multilayered hyperbolic metamaterials: Ellipsometry vs. Reflectometry. *Journal of Applied Physics*. 2015. Vol. 117, no. 10. DOI 10.1063/1.4914524.
42. CHEN, Biqiong, EVANS, Julian R.G., GREENWELL, H. Christopher, BOULET, Pascal, COVENEY, Peter V., BOWDEN, Allen A. and WHITING, Andrew. A critical appraisal of polymer–clay nanocomposites. *Chemical Society Reviews*. 2008. Vol. 37, no. 3, p. 568–594. DOI 10.1039/b702653f.
43. MISHRA, Akhilesh K., MISHRA, Satyendra K. and GUPTA, Banshi D. SPR based fiber optic sensor for refractive index sensing with enhanced detection accuracy and figure of merit in visible region. *Optics Communications*. 2015. Vol. 344, p. 86–91. DOI 10.1016/j.optcom.2015.01.043.
44. CEMIN, F., BIM, L. T., LEIDENS, L. M., MORALES, M., BAUMVOL, I. J.R., ALVAREZ, F. and FIGUEROA, C. A. Identification of the Chemical Bonding Prompting Adhesion of a-C:H Thin Films on Ferrous Alloy Intermediated by a SiCx:H Buffer Layer. *ACS Applied Materials and Interfaces*. 2015. Vol. 7, no. 29, p. 15909–15917. DOI 10.1021/acsami.5b03554.
45. PARDO, A., BUIJNSTERS, J. G., ENDRINO, J. L., GÓMEZ-ALEIXANDRE, C., ABRASONIS, G., BONET, R. and CARO, J. Effect of the metal concentration on the structural, mechanical and tribological properties of self-organized a-C:Cu hard nanocomposite coatings. *Applied Surface Science*. 2013. Vol. 280, p. 791–798. DOI 10.1016/j.apsusc.2013.05.063.
46. JUKNIUS, Tadas, RUŽAUSKAS, Modestas, TAMULEVIČIUS, Tomas, ŠIUGŽDINIENĖ, Rita, JUKNIENĖ, Indrė, VASILIAUSKAS, Andrius, JURKEVIČIŪTĖ, Aušrinė and TAMULEVIČIUS, Sigitas. Antimicrobial properties of diamond-like carbon/silver nanocomposite thin films deposited on textiles: Towards smart bandages. *Materials*. 2016. Vol. 9, no. 5, p. 371. DOI 10.3390/ma9050371.
47. BOCIAGA, Dorota, JAKUBOWSKI, Witold, KOMOROWSKI, Piotr, SOBCZYK-GUZENDA, Anna, JĘDRZEJCZAK, Anna, BATORY, Damian and OLEJNIK, Anna. Surface characterization and biological evaluation of silver-incorporated DLC coatings fabricated by hybrid RF PACVD/MS method. *Materials Science and Engineering C*. 2016. Vol. 63, p. 462–474. DOI 10.1016/j.msec.2016.03.013.

48. VERMA, Roli and GUPTA, Banshi D. Detection of heavy metal ions in contaminated water by surface plasmon resonance based optical fibre sensor using conducting polymer and chitosan. *Food Chemistry*. 2015. Vol. 166, p. 568–575. DOI 10.1016/j.foodchem.2014.06.045.
49. HEDAYATI, Mehdi Keshavarz, ABDELAZIZ, Moheb, ETRICH, Christoph, HOMAEIGOHAR, Shahin, ROCKSTUHL, Carsten and ELBAHRI, Mady. Broadband anti-reflective coating based on plasmonic nanocomposite. *Materials*. 2016. Vol. 9, p. 636. DOI 10.3390/ma9080636.
50. MEŠKINIS, Šarūnas, PECKUS, Domantas, VASILIAUSKAS, Andrius, ČIEGIS, Arvydas, GUDAITIS, Rimantas, TAMULEVIČIUS, Tomas, YAREMCHUK, Iryna and TAMULEVIČIUS, Sigitas. Photovoltaic Properties and Ultrafast Plasmon Relaxation Dynamics of Diamond-Like Carbon Nanocomposite Films with Embedded Ag Nanoparticles. *Nanoscale Research Letters*. 2017. Vol. 12, no. 1, p. 288. DOI 10.1186/s11671-017-2065-1.
51. KAIRAITIS, Gediminas, GRIGALIŪNAS, Artūras, BAGINSKAS, Armuntas and GALDIKAS, Arvaidas. Kinetic modeling of phase separation and surface segregation in growing a-C:Ni thin films. *Surface and Coatings Technology*. 2018. Vol. 352, p. 120–127. DOI 10.1016/j.surfcoat.2018.08.012.
52. ZILLOHU, Ahnaf Usman, ABDELAZIZ, Ramzy, HEDAYATI, Mehdi Keshavarz, EMMLER, Thomas, HOMAEIGOHAR, Shahin and ELBAHRI, Mady. Plasmon-Mediated Embedding of Nanoparticles in a Polymer Matrix: Nanocomposites Patterning, Writing, and Defect Healing. *Journal of Physical Chemistry C*. 2012. Vol. 116, no. 32, p. 17204–17209. DOI 10.1021/jp3016358.
53. PARDO, A., GÓMEZ-ALEIXANDRE, C., CELIS, J. P. and BUIJNSTERS, J. G. Friction and wear behavior of plasma assisted chemical vapor deposited nanocomposites made of metal nanoparticles embedded in a hydrogenated amorphous carbon matrix. *Surface and Coatings Technology*. 2012. Vol. 206, no. 13, p. 3116–3124. DOI 10.1016/j.surfcoat.2011.12.041.
54. CLOUTIER, M., HARNAGEA, C., HALE, P., SEDDIKI, O., ROSEI, F. and MANTOVANI, D. Long-term stability of hydrogenated DLC coatings: Effects of aging on the structural, chemical and mechanical properties. *Diamond and Related Materials*. 2014. Vol. 48, p. 65–72. DOI 10.1016/j.diamond.2014.07.002.
55. CASIRAGHI, C., PIAZZA, F., FERRARI, A. C., GRAMBOLE, D. and ROBERTSON, J. Bonding in hydrogenated diamond-like carbon by Raman spectroscopy. *Diamond and Related Materials*. 2005. Vol. 14, no. 3–7, p. 1098–1102. DOI 10.1016/j.diamond.2004.10.030.
56. DING, Xing-zhao, MAO, Dong-sheng, TAY, B. K., LAU, S. P., SHI, J. R., LI, Y. J., SUN, Z., SHI, X., TAN, H. S., ZHANG, Fu-min and LIU, Xiang-huai. Annealing effect on electron field-emission properties of diamond-like nanocomposite films. *Journal of applied physics*. 2000. Vol. 88, no. 9, p. 5087–5092. DOI 10.1063/1.1319166.

57. BUTT, M. Z., KHALEEQ-UR-RAHMAN, M., ALI, Dilawar, AKMAL, Amna and NASEEM, S. Deposition and characterization of multilayer DLC:Mo thin films grown on silicon substrate by off-axis pulsed laser deposition technique. *Applied Surface Science*. 2015. Vol. 331, p. 407–414. DOI 10.1016/j.apsusc.2015.01.083.
58. JO, Yeong Ju, ZHANG, Teng Fei, SON, Myoung Jun and KIM, Kwang Ho. Synthesis and electrochemical properties of Ti-doped DLC films by a hybrid PVD/PECVD process. *Applied Surface Science*. 2018. Vol. 433, p. 1184–1191. DOI 10.1016/j.apsusc.2017.10.151.
59. FERRARI, A. C. and ROBERTSON, J. Interpretation of Raman spectra of disordered and amorphous carbon. *Physical Review B*. 2000. Vol. 61, no. 20, p. 14095–14107. DOI 10.1007/BF02543693.
60. SANTOS, Thaisa B., VIEIRA, Angela A., PAULA, Luciana O., SANTOS, Everton D., RADI, Polyana A., KHOURI, Sônia, MACIEL, Homero S., PESSOA, Rodrigo S. and VIEIRA, Lucia. Flexible camphor diamond-like carbon coating on polyurethane to prevent Candida albicans biofilm growth. *Journal of the Mechanical Behavior of Biomedical Materials*. 2017. Vol. 68, p. 239–246. DOI 10.1016/j.jmbbm.2017.02.013.
61. KANEKO, Satoru, HORIUCHI, Takahiro, YOSHIDA, Kentaro, TANAKA, Satomi, KATO, Chihiro, KANO, Makoto, KUMAGAI, Masao, TANOUE, Hideto, KAMIYA, Masao and TAKIKAWA, Hirofumi. Mass density as basis parameter on mechanical properties under diamond-like carbon prepared in wide range of conditions using variety of methods. *Japanese Journal of Applied Physics*. 2011. Vol. 50, p. 9–12. DOI 10.1143/JJAP.50.01AF11.
62. FIASCHI, Giulia, ROTA, Alberto, BALLESTRAZZI, Antonio, MARCHETTO, Diego, VEZZALINI, Enrico and VALERI, Sergio. A Chemical, Mechanical, and Tribological Analysis of DLC Coatings Deposited by Magnetron Sputtering. *Lubricants*. 2019. Vol. 7, no. 4, p. 38. DOI 10.3390/lubricants7040038.
63. ROCH, Teja, BEYER, Eckhard and LASAGNI, Andrés. Surface modification of thin tetrahedral amorphous carbon films by means of UV direct laser interference patterning. *Diamond and Related Materials*. 2010. Vol. 19, no. 12, p. 1472–1477. DOI 10.1016/j.diamond.2010.10.003.
64. YANG, Jianji, GIESSEN, Harald and LALANNE, Philippe. Simple analytical expression for the peak-frequency shifts of plasmonic resonances for sensing. *Nano Letters*. 2015. Vol. 15, no. 5, p. 3439–3444. DOI 10.1021/acs.nanolett.5b00771.
65. MAIER, Stefan Alexander. *Plasmonics: Fundamentals and Applications*. New York : Springer, 2007. ISBN 9780387378251.
66. FAUCHEAUX, Jacob A., STANTON, Alexandria L D and JAIN, Prashant K. Plasmon resonances of semiconductor nanocrystals: Physical principles and new opportunities. *Journal of Physical Chemistry Letters*. 2014. Vol. 5, no. 6, p. 976–985. DOI 10.1021/jz500037k.
67. YAREMCHUK, Iryna, TAMULEVIČIENĖ, Asta, TAMULEVIČIUS,

Tomas, ŠLAPIKAS, Kęstutis, BALEVIČIUS, Zigmas and TAMULEVIČIUS, Sigitas. Modeling of the plasmonic properties of DLC-Ag nanocomposite films. *Physica Status Solidi (A) Applications and Materials Science*. 2014. Vol. 211, no. 2, p. 329–335. DOI 10.1002/pssa.201330067.

68. CHEN, Kong Y., JANZ, Kathleen F., ZHU, Weimo and BRYCHTA, Robert J. Re-defining the Roles of Sensors in Objective Physical Activity Monitoring. *Medicine & Science in Sports & Exercise*. January 2012. Vol. 44, no. 1S, p. S13–S23. DOI 10.1249/MSS.0b013e3182399bc8.
69. LU, Xiaoyuan, WAN, Rengang, LIU, Feng and ZHANG, Tongyi. High-sensitivity plasmonic sensor based on perfect absorber with metallic nanoring structures. *Journal of Modern Optics*. 2015. Vol. 63, no. 2, p. 177–183. DOI 10.1080/09500340.2015.1066459.
70. CHUNG, Kyungwha, RANI, Adila, LEE, Ji Eun, KIM, Ji Eun, KIM, Yonghwi, YANG, Heejin, KIM, Sang Ouk, KIM, Donghyun and KIM, Dong Ha. Systematic study on the sensitivity enhancement in graphene plasmonic sensors based on layer-by-layer self-assembled graphene oxide multilayers and their reduced analogues. *ACS Applied Materials & Interfaces*. 2015. Vol. 7, no. 1, p. 144–151. DOI 10.1021/am508103z.
71. MACIAS, Gerard, SPERLING, Justin Ryan, PEVELER, William J., BURLEY, Glenn A, NEALE, Steven L. and CLARK, Alasdair W. Whisky tasting using a bimetallic nanoplasmonic tongue. *Nanoscale*. 2019. P. 27–31. DOI 10.1039/C9NR04583J.
72. PRASAD, Janak, ZINS, Inga, BRANSCHEID, Robert, BECKER, Jan, KOCH, Amelie H. R., FYTAS, George, KOLB, Ute and SÖNNICHSEN, Carsten. Plasmonic core-satellite assemblies as highly sensitive refractive index sensors. *Journal of Physical Chemistry C*. 2015. Vol. 119, no. 10, p. 5577–5582. DOI 10.1021/jp510985n.
73. WHITE, Ian M. and FAN, Xudong. On the performance quantification of resonant refractive index sensors. *Microfluidics and Nanofluidics*. 2008. Vol. 16, no. 2, p. 1020–1028. DOI 10.1364/OE.16.001020.
74. YAREMCHUK, Iryna, TAMULEVIČIENĖ, Asta, TAMULEVIČIUS, Tomas and TAMULEVIČIUS, Sigitas. Optical Properties of DLC-Ag Nanocomposite and Grating Structures on their Base. *Applied Mechanics and Materials*. 2014. Vol. 490–491, p. 53–57. DOI 10.4028/www.scientific.net/amm.490-491.53.
75. ZHAO, Wenyu, JU, Dongquan and JIANG, Yongyuan. Sharp Fano Resonance within Bi-periodic Silver Particle Array and Its Application as Plasmonic Sensor with Ultra-high Figure of Merit. *Plasmonics*. 2015. Vol. 10, no. 2, p. 469–474. DOI 10.1007/s11468-014-9829-6.
76. VIRGANAVIČIUS, D., CADARSO, V. J., KIRCHNER, R., STANKEVIČIUS, L., TAMULEVIČIUS, T., TAMULEVIČIUS, S. and SCHIFT, H. Patterning of diamond like carbon films for sensor applications using silicon containing thermoplastic resist (SiPol) as a hard mask. *Applied Surface Science*. 2016. Vol. 385, p. 145–152.

DOI 10.1016/j.apsusc.2016.05.100.
77. TAMULEVIČIUS, Tomas, TAMULEVIČIENE, Asta, VIRGANAVIČIUS, Dainius, VASILIAUSKAS, Andrius, KOPUSTINSKAS, Vitoldas, MEŠKINIS, Šarunas and TAMULEVIČIUS, Sigitas. Structuring of DLC:Ag nanocomposite thin films employing plasma chemical etching and ion sputtering. *Nuclear Instruments and Methods in Physics Research, Section B: Beam Interactions with Materials and Atoms*. 2014. Vol. 341, p. 1–6. DOI 10.1016/j.nimb.2013.09.052.
78. CHOI, W. K., LIEW, T. H., DAWOOD, M. K., SMITH, Henry I., THOMPSON, C. V. and HONG, M. H. Synthesis of silicon nanowires and nanofin arrays using interference lithography and catalytic etching. *Nano Letters*. 2008. Vol. 8, no. 11, p. 3799–3802. DOI 10.1021/nl802129f.
79. LANGNER, A., PÄIVÄNRANTA, B., TERHALLE, B. and EKINCI, Y. Fabrication of quasiperiodic nanostructures with EUV interference lithography. *Nanotechnology*. 2012. Vol. 23, no. 10, p. 105303. DOI 10.1088/0957-4484/23/10/105303.
80. GACHOT, Carsten, ROSENKRANZ, Andreas, BUCHHEIT, Roman, SOUZA, Nicolas and MÜCKLICH, Frank. Tailored frictional properties by Penrose inspired surfaces produced by direct laser interference patterning. *Applied Surface Science*. 2016. Vol. 367, p. 174–180. DOI 10.1016/j.apsusc.2016.01.169.
81. YEO, Jong-Bin, YUN, Sang-Don, KIM, Nam-Hoon and LEE, Hyun-Yong. Fabrication of Si-based two-dimensional photonic quasicrystals by using multiple-exposure holographic lithography. *Journal of Vacuum Science & Technology B: Microelectronics and Nanometer Structures*. 2009. Vol. 27, no. 4, p. 1886. DOI 10.1116/1.3159782.
82. LAI, Ngoc D., LIN, Jian H., HUANG, Yi Y. and HSU, Chia C. Fabrication of two- and three-dimensional quasi-periodic structures with 12-fold symmetry by interference technique. *Optics Express*. 2006. Vol. 14, no. 22, p. 10746. DOI 10.1364/oe.14.010746.
83. WANG, Lei, LU, Zhen Hua, LIN, Xiao Feng, CHEN, Qi Dai, XU, Bin Bin and SUN, Hong Bo. Rapid fabrication of large-area periodic structures by multiple exposure of two-beam interference. *Journal of Lightwave Technology*. 2013. Vol. 31, no. 2, p. 276–281. DOI 10.1109/JLT.2012.2228632.
84. VOISIAT, Bogdan, GEDVILAS, Mindaugas, INDRIŠIUNAS, Simonas and RACIUKAITIS, Gediminas. Flexible microstructuring of thin films using multi-beam interference: Ablation with ultrashort lasers. *Journal of Laser Micro Nanoengineering*. 2011. Vol. 6, no. 3, p. 185–190. DOI 10.2961/jlmn.2011.03.0002.
85. ALAMRI, Sabri, AGUILAR-MORALES, Alfredo I. and LASAGNI, Andrés F. Controlling the wettability of polycarbonate substrates by producing hierarchical structures using Direct Laser Interference Patterning. *European Polymer Journal*. 2018. Vol. 99, p. 27–37. DOI 10.1016/j.eurpolymj.2017.12.001.

86. LEE, Jeong Bong, CHOI, Kyung Hak and YOO, Koangki. Innovative SU-8 lithography techniques and their applications. *Micromachines*. 2015. Vol. 6, no. 1, p. 1–18. DOI 10.3390/mi6010001.
87. LASAGNI, Andrés Fabián. Laser interference patterning methods: Possibilities for high-throughput fabrication of periodic surface patterns. *Advanced Optical Technologies*. 27 January 2017. Vol. 6, no. 3–4. DOI 10.1515/aot-2017-0016.
88. STANKEVIČIUS, E., GEDVILAS, M., VOISIAT, B., MALINAUSKAS, M. and RAČIUKAITIS, G. Fabrication of periodic micro-structures by holographic lithography. *Lithuanian Journal of Physics*. 2013. Vol. 53, no. 4, p. 227–237. DOI 10.3952/physics.v53i4.2765.
89. LIU, Quan, WU, Jianhong and ZHOU, Yang. Fabrication of the metal wire-grid polarizer in visible light. *Selected Papers of the Chinese Society for Optical Engineering Conferences*. 2017. Vol. 10255, p. 102554K. DOI 10.1117/12.2268374.
90. BRUECK, S. R. J. Optical and interferometric lithography-nanotechnology enablers. *Proceedings of the IEEE*. 2005. Vol. 93, no. 10, p. 1704–1721. DOI 10.1109/JPROC.2005.853538.
91. SCHIEFER, Tom, JANSEN, Irene, BIEDA, Matthias, PAP, József-Sebastian and LASAGNI, Andrés-Fabián. Large Area Surface Structuring by Direct Laser Interference Patterning for Adhesive Bonding Applications. *Journal of The Adhesion Society of Japan*. 2015. Vol. 51, no. s1, p. 223–224. DOI 10.11618/adhesion.51.223.
92. KIESOW, A., STROHKARK, S., LÖSCHNER, K., HEILMANN, A., PODLIPENSKY, A., ABDOLVAND, A. and SEIFERT, G. Generation of wavelength-dependent, periodic line pattern in metal nanoparticle-containing polymer films by femtosecond laser irradiation. *Applied Physics Letters*. 2005. Vol. 86, no. 15, p. 153111. DOI 10.1063/1.1897052.
93. NAKATA, Yoshiki. Interference laser processing. *Advanced Optical Technologies*. 1 January 2016. Vol. 5, no. 1, p. 29–38. DOI 10.1515/aot-2015-0060.
94. PEDROTTI, Frank J. and PEDROTTI, Leno S. *Introduction to Optics*. 2nd editio. Englewood Cliffs : Prentice Hall, Inc., 1993. ISBN 9780135015452.
95. SHAHEEN, M. E., GAGNON, J. E. and FRYER, B. J. Femtosecond laser ablation behavior of gold, crystalline silicon, and fused silica: a comparative study. *Laser Physics*. 2014. Vol. 24, p. 106102. DOI 10.1088/1054-660X/24/10/106102.
96. AGUILAR-MORALES, Alfredo I., ALAMRI, Sabri and LASAGNI, Andrés Fabián. Micro-fabrication of high aspect ratio periodic structures on stainless steel by picosecond direct laser interference patterning. *Journal of Materials Processing Technology*. 2018. Vol. 252, p. 313–321. DOI 10.1016/j.jmatprotec.2017.09.039.
97. LOESCHNER, K., SEIFERT, G. and HEILMANN, A. Self-organized, gratinglike nanostructures in polymer films with embedded metal nanoparticles induced by femtosecond laser irradiation. *Journal of Applied*

Physics. 2010. Vol. 108, no. 7, p. 073114. DOI 10.1063/1.3490191.
98. LIU, Zeming, SIEGEL, Jan, GARCIA-LECHUGA, Mario, EPICIER, Thierry, LEFKIR, Yaya, REYNAUD, Stéphanie, BUGNET, Matthieu, VOCANSON, Francis, SOLIS, Javier, VITRANT, Guy and DESTOUCHES, Nathalie. Three-Dimensional Self-Organization in Nanocomposite Layered Systems by Ultrafast Laser Pulses. *ACS Nano*. 2017. Vol. 11, no. 5, p. 5031–5040. DOI 10.1021/acsnano.7b01748.
99. FAUPEL, Franz, ZAPOROJTCHENKO, Vladimir, STRUNSKUS, Thomas and ELBAHRI, Mady. Metal-polymer nanocomposites for functional applications. *Advanced Engineering Materials*. 2010. Vol. 12, no. 12, p. 1177–1190. DOI 10.1002/adem.201000231.
100. CORREA, Daniel, ALMEIDA, Juliana, ALMEIDA, Gustavo, CARDOSO, Marcos, DE BONI, Leonardo and MENDONÇA, Cleber. Ultrafast Laser Pulses for Structuring Materials at Micro/Nano Scale: From Waveguides to Superhydrophobic Surfaces. *Photonics*. 2017. Vol. 4, no. 1, p. 1–26. DOI 10.3390/photonics4010008.
101. DANILOV, P. A., ZAYARNY, D. A., IONIN, A. A., KUDRYASHOV, S. I., RUDENKO, A. A., KUCHMIZHAK, A. A., VITRIK, O. B., KULCHIN, Yu. N., ZHAKHOVSKY, V. V. and INOGAMOV, N. A. Redistribution of a material at femtosecond laser ablation of a thin silver film. *JETP Letters*. 2016. Vol. 104, no. 11, p. 759–765. DOI 10.1134/s0021364016230077.
102. KOMLENOK, M. S., ARUTYUNYAN, N. R., KONONENKO, V. V., ZAVEDEEV, E. V., FROLOV, V. D., CHOUPRIK, A. A., BATURIN, A. S., SCHEIBE, H. J. and PIMENOV, S. M. Structure and friction properties of laser-patterned amorphous carbon films. *Diamond and Related Materials*. 2016. Vol. 65, p. 69–74. DOI 10.1016/j.diamond.2016.02.006.
103. WILSON, O., WILSON, G. J. and MULVANEY, P. Laser writing in polarized silver nanorod films. *Advanced Materials*. 2002. Vol. 14, no. 13–14, p. 1000–1004. DOI 10.1002/1521-4095(20020704)14:13/14<1000::AID-ADMA1000>3.0.CO;2-H.
104. LANG, Valentin, ROCH, Teja and LASAGNI, Andrés Fabián. High-Speed Surface Structuring of Polycarbonate Using Direct Laser Interference Patterning: Toward 1 m2 min-1 Fabrication Speed Barrier. *Advanced Engineering Materials*. 2016. Vol. 18, no. 8, p. 1342–1348. DOI 10.1002/adem.201600173.
105. MOUSAVI, A., KUNZE, T., ROCH, T., LASAGNI, A. and BROSIUS, A. Deep drawing process without lubrication - an adapted tool for a stable, economic and environmentally friendly process. *Procedia Engineering*. 2017. Vol. 207, p. 48–53. DOI 10.1016/j.proeng.2017.10.736.
106. WOOD, Roger M. Laser-Induced Damage by Thermal Effects. In : RISTAU, Detlev (ed.), *Laser-Induced Damage in Optical Materials*. Boca Raton : CRC Press, Taylor & Francis Group, 2015. p. 9–24. ISBN 9781439872178.
107. KAFKA, K. R. P., TALISA, N., TEMPEA, G., AUSTIN, D. R., NEACSU, C. and CHOWDHURY, E. A. Few-cycle pulse laser induced damage threshold determination of ultra-broadband optics. *Optics Express*. 2016.

Vol. 24, no. 25, p. 28858–28868. DOI 10.1364/OE.24.028858.
108. SALAMA, A., LI, L., MATIVENGA, P. and SABLI, A. High-power picosecond laser drilling/machining of carbon fibre-reinforced polymer (CFRP) composites. *Applied Physics A: Materials Science and Processing*. 2016. Vol. 122, no. 2, p. 73. DOI 10.1007/s00339-016-9607-8.
109. NATHALA, Chandra S.R., AJAMI, Ali, HUSINSKY, Wolfgang, FAROOQ, Bilal, KUDRYASHOV, Sergey I., DASKALOVA, Albena, BLIZNAKOVA, Irina and ASSION, Andreas. Ultrashort laser pulse ablation of copper, silicon and gelatin: effect of the pulse duration on the ablation thresholds and the incubation coefficients. *Applied Physics A: Materials Science and Processing*. 2016. Vol. 122, p. 1–8. DOI 10.1007/s00339-016-9625-6.
110. TAMULEVIČIUS, Sigitas, MEŠKINIS, Šarūnas, TAMULEVIČIUS, Tomas and RUBAHN, Horst Günter. Diamond like carbon nanocomposites with embedded metallic nanoparticles. *Reports on Progress in Physics*. 2018. Vol. 81, no. 2, p. 024501. DOI 10.1088/1361-6633/aa966f.
111. SUTTMANN, Oliver, DUESING, Jan and OVERMEYER, Ludger. Phenomenological model for prediction of complex ablation geometries in metal films using ultrashort laser pulses. *Journal of Laser Applications*. 2016. Vol. 28, no. 2, p. 022208. DOI 10.2351/1.4944507.
112. GAUDIUSO, Caterina, GIANNUZZI, Giuseppe, VOLPE, Annalisa, LUGARÀ, Pietro Mario, CHOQUET, Isabelle and ANCONA, Antonio. Incubation during laser ablation with bursts of femtosecond pulses with picosecond delays. *Optics Express*. 2018. Vol. 26, no. 4, p. 3801. DOI 10.1364/OE.26.003801.
113. ROSENFELD, A., LORENZ, M., STOIAN, R. and ASHKENASI, D. Ultrashort-laser-pulse damage threshold of transparent materials and the role of incubation. *Applied Physics A: Materials Science and Processing*. 1999. Vol. 69, no. 7, p. 373–376. DOI 10.1007/s003399900237.
114. RUBLACK, Tino, MUCHOW, Markus, HARTNAUER, Stefan and SEIFERT, Gerhard. Laser ablation of silicon dioxide on silicon using femtosecond near infrared laser pulses. *Energy Procedia*. 2011. Vol. 8, p. 467–472. DOI 10.1016/j.egypro.2011.06.167.
115. JEE, Yong, BECKER, Michael F. and WALSER, Rodger M. Laser-induced damage on single-crystal metal surfaces. *Journal of the Optical Society of America B*. 1988. Vol. 5, no. 3, p. 648–659. DOI 10.1364/JOSAB.5.000648.
116. ASHKENASI, D., LORENZ, M., STOIAN, R. and ROSENFELD, A. Surface damage threshold and structuring of dielectrics using femtosecond laser pulses: the role of incubation. *Applied Surface Science*. 1999. Vol. 150, p. 101–106. DOI 10.1016/S0169-4332(99)00228-7.
117. SHI, Feng. Introductory Chapter: Basic Theory of Magnetron Sputtering. In : *Magnetron Sputtering*. IntechOpen, 2018.
118. ANDERS, André. Tutorial: Reactive high power impulse magnetron sputtering (R-HiPIMS). *Journal of Applied Physics*. 2017. Vol. 121, no. 17, p. 171101. DOI 10.1063/1.4978350.
119. MEŠKINIS, Šarūnas, TAMULEVIČIUS, Tomas, NIAURA, Gediminas,

ŠLAPIKAS, Kęstutis, VASILIAUSKAS, Andrius, ULČINAS, Orestas and TAMULEVIČIUS, Sigitas. Surface Enhanced Raman Scattering Effect in Diamond Like Carbon Films Containing Ag Nanoparticles. *Journal of Nanoscience and Nanotechnology*. 2016. Vol. 16, no. 9, p. 10143–10151. DOI 10.1166/jnn.2016.12848.

120. JILANI, Asim, ABDEL-WAHAB, Mohamed Shaaban and HAMMAD, Ahmed Hosny. Advance Deposition Techniques for Thin Film and Coating. In : NIKITENKOV, Nikolay N. (ed.), *Modern Technologies for Creating the Thin-film Systems and Coatings*. IntechOpen, 2017. p. 13.
121. GEDI, Sreedevi, REDDY, Vasudeva Reddy Minnam, KANG, Jeong-yoon and JEON, Chan-Wook. Impact of high temperature and short period annealing on SnS films deposited by E-beam evaporation. *Applied Surface Science*. 30 April 2017. Vol. 402, p. 463–468. [Accessed 4 June 2019]. DOI 10.1016/J.APSUSC.2017.01.113.
122. ADOMAVIČIŪTĖ, Erika, TAMULEVIČIUS, Tomas, ŠIMATONIS, Linas, FATARAITĖ-URBONIENĖ, Eglė, STANKEVIČIUS, Edgaras and TAMULEVIČIUS, Sigitas. Micro-structuring of electrospun mats employing femtosecond laser. *Medziagotyra*. 2015. Vol. 21, no. 1, p. 44–51. DOI 10.5755/j01.ms.21.1.10249.
123. TAMULEVIČIUS, Tomas, JUODĖNAS, Mindaugas, KLINAVIČIUS, Tomas, PAULAUSKAS, Andrius, JANKAUSKAS, Kęstutis, OSTREIKA, Armantas, ŽUTAUTAS, Andrius and TAMULEVIČIUS, Sigitas. Dot-Matrix Hologram Rendering Algorithm and its Validation through Direct Laser Interference Patterning. *Scientific Reports*. 2018. Vol. 8, no. 1, p. 1–11. DOI 10.1038/s41598-018-32294-5.
124. RÖSSLER, Florian, KUNZE, Tim and LASAGNI, Andrés Fabián. Fabrication of diffraction based security elements using direct laser interference patterning. *Optics Express*. 2017. Vol. 25, no. 19, p. 22959. DOI 10.1364/OE.25.022959.
125. ma-P 1200: Photoresist series for UV lithography. *Micro Resist Technology*. 2015. [Accessed 12 February 2020].
126. DI NISO, Francesca, GAUDIUSO, Caterina, SIBILLANO, Teresa, MEZZAPESA, Francesco Paolo, ANCONA, Antonio and LUGARÀ, Pietro Mario. Role of heat accumulation on the incubation effect in multi-shot laser ablation of stainless steel at high repetition rates. *Optics Express*. 2014. Vol. 22, no. 10, p. 12200. DOI 10.1364/OE.22.012200.
127. INKSON, B. J. Scanning electron microscopy (SEM) and transmission electron microscopy (TEM) for materials characterization. In : HÜBSCHEN, Gerhard, ALTPETER, Iris, TSCHUNCKY, Ralf and HERRMANN, Hans-Georg (eds.), *Materials Characterization Using Nondestructive Evaluation (NDE) Methods*. Elsevier, 2016. p. 17–43.
128. NOTTE, John A., WARD, Bill W., ECONOMOU, Nick, HILL, Ray, PERCIVAL, Randy, FARKAS, Lou and MCVEY, Shawn. An introduction to the helium ion microscope. *AIP Conference Proceedings*. 2007. Vol. 931, no. February, p. 489–496. DOI 10.1063/1.2799423.

129. ZHANG, Jack Y., HWANG, Jinwoo, ISAAC, Brandon J. and STEMMER, Susanne. Variable-angle high-angle annular dark-field imaging: Application to three-dimensional dopant atom profiling. *Scientific Reports*. 2015. Vol. 5, p. 12419. DOI 10.1038/srep12419.
130. BRANDLEY, Eileen, GREENHALGH, Emile S., SHAFFER, Milo S. P. and LI, Qianqian. Mapping carbon nanotube orientation by fast fourier transform of scanning electron micrographs. *Carbon*. 2018. Vol. 137, p. 78–87. DOI 10.1016/j.carbon.2018.04.063.
131. SCHNEIDER, Caroline A, RASBAND, Wayne S and ELICEIRI, Kevin W. NIH Image to ImageJ: 25 years of image analysis. *Nature Methods*. 28 July 2012. Vol. 9, no. 7, p. 671–675. DOI 10.1038/nmeth.2089.
132. Particle Analysis. *ImageJ*. 2017. [Accessed 17 August 2019].
133. ZIMNY, Kévin, MASCARO, Benoit, BRUNET, Thomas, PONCELET, Olivier, ARISTÉGUI, Christophe, LENG, Jacques, SANDRE, Olivier and MONDAIN-MONVAL, Olivier. Design of a fluorinated magneto-responsive material with tuneable ultrasound scattering properties. *Journal of Materials Chemistry B*. 2014. Vol. 2, no. 10, p. 1285–1297. DOI 10.1039/c3tb21585g.
134. LIMPERT, Ackhard, STAHEL, Werner A. and MARKUS, Abbt. Log-normal Distributions across the Sciences: Keys and Clues. *BioScience*. 2001. Vol. 51, no. 5, p. 341–352. DOI 10.1641/0006-3568(2001)051[0341:LNDATS]2.0.CO;2.
135. BUMBRAH, Gurvinder Singh and SHARMA, Rakesh Mohan. Raman spectroscopy – Basic principle, instrumentation and selected applications for the characterization of drugs of abuse. *Egyptian Journal of Forensic Sciences*. 2016. Vol. 6, no. 3, p. 209–215. DOI 10.1016/j.ejfs.2015.06.001.
136. SEIFTER, A., BOBORIDIS, K. and OBST, A. W. Emissivity measurements on metallic surfaces with various degrees of roughness: A comparison of laser polarimetry and integrating sphere reflectometry. *International Journal of Thermophysics*. 2004. Vol. 25, no. 2, p. 547–560. DOI 10.1023/B:IJOT.0000028489.81327.b7.
137. MARSILLAC, Sylvain, SESTAK, Michelle N., LI, Jian and COLLINS, Robert W. Spectroscopic Ellipsometry. In : ABOU-RAS, Daniel, KIRCHARTZ, Thomas and RAU, Uwe (eds.), *Advanced Characterization Techniques for Thin Film Solar Cells*. Weinheim : Wiley-VCH Verlag GmbH, 2011. p. 125–149. ISBN 9783527410033.
138. JUNG, Y. W., BYUN, J. S., WOO, D. H. and KIM, Y. D. Ellipsometric analysis of porous anodized aluminum oxide films. *Thin Solid Films*. 2009. Vol. 517, no. 13, p. 3726–3730. DOI 10.1016/j.tsf.2008.12.051.
139. DE LAET, J., TERRYN, Herman. A. and VEREECKEN, J. Development of an optical model for steady state porous anodic films on aluminium formed in phosphoric acid. *Thin Solid Films*. 1998. Vol. 320, no. 2, p. 241–252. DOI 10.1016/s0040-6090(97)00741-4.
140. ZHONG, Chuan, BALLANTINE, Kyle E., KERVICK, Christopher, SMITH, Christopher M., MULLARKEY, D., SHVETS, I. V., DONEGAN, John F. and MCCLOSKEY, David. Mapping of surface plasmon dispersion in thin

Ag–Au layered composite films. *Journal of the Optical Society of America B*. 2016. Vol. 33, no. 4, p. 566. DOI 10.1364/JOSAB.33.000566.
141. JELLISON, G. E., LEONARD, D. N., ANOVITZ, L. M., PARISH, C. M., SPECHT, E. D. and ROSSEEL, T. M. Crystallographic orientation of uniaxial calcite and dolomite determined using reflection generalized ellipsometry. *Journal of Applied Physics*. 2018. Vol. 124, p. 223102. DOI 10.1063/1.5048724.
142. SCHRAM, T., FRANQUET, A., TERRYN, Herman. A. and VEREECKEN, J. Spectroscopic Ellipsometry: a Non-destructive Technique for Surface Analysis. *Advanced Engineering Materials*. 1999. Vol. 1, no. 1, p. 63–66. DOI 10.1002/(SICI)1527-2648(199909)1:1<63::AID-ADEM63>3.0.CO;2-1.
143. GILLIOT, Mickaël, HADJADJ, Aomar and STCHAKOVSKY, Michel. Spectroscopic ellipsometry data inversion using constrained splines and application to characterization of ZnO with various morphologies. *Applied Surface Science*. 2017. Vol. 421, p. 453–459. DOI 10.1016/j.apsusc.2016.09.106.
144. YAREMCHUK, Iryna, MEŠKINIS, Šarūnas, FITIO, Volodymyr, BOBITSKI, Yaroslav, ŠLAPIKAS, Kęstutis, ČIEGIS, Arvydas, BALEVIČIUS, Zigmas, SELSKIS, Algirdas and TAMULEVIČIUS, Sigitas. Spectroellipsometric characterization and modeling of plasmonic diamond-like carbon nanocomposite films with embedded Ag nanoparticles. *Nanoscale research letters*. 2015. Vol. 10, p. 157. DOI 10.1186/s11671-015-0854-y.
145. ROTHFELDER, M., BLÄSI, B., PETERS, M., KÜNLE, M. and JANZ, S. Using Spectroscopic Ellipsometry for the Characterisation of Thin Films for. *24th EUPVSEC Hamburg Germany*. 2009. P. 21–25.
146. FUJIWARA, H., KOH, Joohyun, ROVIRA, P. and COLLINS, R. Assessment of effective-medium theories in the analysis of nucleation and microscopic surface roughness evolution for semiconductor thin films. *Physical Review B - Condensed Matter and Materials Physics*. 2000. Vol. 61, no. 16, p. 10832–10844. DOI 10.1103/PhysRevB.61.10832.
147. LUGOSI, Laszlo and BASA, Peter (eds.). *Spectroscopic Ellipsometry Analyzer User's Reference Manual*. Budapest : Semilab Co. Ltd, 2012.
148. OGWU, A. A., OKPALUGO, T. I. T. and MCLAUGHLIN, J. A. D. The effect of PECVD plasma decomposition on the wettability and dielectric constant changes in silicon modified DLC films for potential MEMS and low stiction applications. *AIP Advances*. 2012. Vol. 2, no. 3, p. 0–8. DOI 10.1063/1.4742852.
149. GUPTA, S., WEINER, B. R. and MORELL, G. Ex situ spectroscopic ellipsometry investigations of chemical vapor deposited nanocomposite carbon thin films. *Thin Solid Films*. 2004. Vol. 455–456, p. 422–428. DOI 10.1016/j.tsf.2003.11.238.
150. MONTIEL-GONZÁLEZ, Z., RODIL, S. E., MUHL, S., MENDOZA-GALVÁN, A. and RODRÍGUEZ-FERNÁNDEZ, L. Amorphous carbon gold nanocomposite thin films: Structural and spectro-ellipsometric analysis. *Thin*

Solid Films. 2011. Vol. 519, no. 18, p. 5924–5932. DOI 10.1016/j.tsf.2011.03.024.
151. SUN, Yao, HUANG, Xing Ye and WANG, Hong. Influence of Hydrogen Content on Optical and Mechanical Performances of Diamond-Like Carbon Films on Glass Substrate. *Journal of Materials Engineering and Performance*. 2016. Vol. 25, no. 4, p. 1570–1577. DOI 10.1007/s11665-016-1975-x.
152. ZKRIA, Abdelrahman, ABDEL-WAHAB, Fouad, KATAMUNE, Yuki and YOSHITAKE, Tsuyoshi. Optical and structural characterization of ultrananocrystalline diamond/hydrogenated amorphous carbon composite films deposited via coaxial arc plasma. *Current Applied Physics*. 2019. Vol. 19, no. 2, p. 143–148. DOI 10.1016/j.cap.2018.11.012.
153. ZHANG, X., WEBER, W. H., VASSELL, W. C., POTTER, T. J. and TAMOR, M. A. Optical study of silicon-containing amorphous hydrogenated carbon. *Journal of ap*. 1998. Vol. 83, no. 5, p. 2820–2825.
154. SENKEVICH, J. J., YANG, G. R., LU, T. M. and SHERRER, D. W. Compositional control of plasma enhanced chemical vapor deposited diamond-like carbon/SiO2 nanocomposite thin films. *Applied Physics A: Materials Science and Processing*. 2003. Vol. 77, no. 3–4, p. 581–584. DOI 10.1007/s00339-002-1501-x.
155. ABAD, M. D., SÁNCHEZ-LÓPEZ, J. C., CUSNIR, N. and SANJINES, R. WC/a-C nanocomposite thin films: Optical and electrical properties. *Journal of Applied Physics*. 2009. Vol. 105, no. 3, p. 033510. DOI 10.1063/1.3060717.
156. SAFAIE, Pouria, ESHAGHI, Akbar and BAKHSHI, Saeed Reza. Optical properties of oxygen doped diamond-like carbon thin films. *Journal of Alloys and Compounds*. 2016. Vol. 672, p. 426–432. DOI 10.1016/j.jallcom.2016.02.195.
157. DAVID, Denis and GODET, Christian. Derivation of dielectric function and inelastic mean free path from photoelectron energy-loss spectra of amorphous carbon surfaces. *Applied Surface Science*. 2016. Vol. 387, p. 1125–1139. DOI 10.1016/j.apsusc.2016.06.044.
158. HUBER, Christian, STEIN, Benedikt and KALT, Heinz. Plasma-enhanced chemical vapor deposition of amorphous silicon carbonitride: Deposition temperature dependence of bonding structure, refractive index, mechanical stress and their aging under ambient air. *Thin Solid Films*. 2017. Vol. 634, p. 66–72. DOI 10.1016/j.tsf.2017.05.004.
159. DJURIŠIĆ, Aleksandra B., RAKIĆ, Aleksandar D. and ELAZAR, Jovan M. Modeling the optical constants of solids using acceptance-probability-controlled simulated annealing with an adaptive move generation procedure. *Physical Review E*. 1997. Vol. 55, no. 4, p. 4797–4803. DOI 10.1103/PhysRevE.55.4797.
160. YANG, Zih-Ying, CHEN, Yi-Hsun, LIAO, Bo-Huei and CHEN, Kuo-Ping. Room temperature fabrication of titanium nitride thin films as plasmonic materials by high-power impulse magnetron sputtering. *Optical Materials*

Express. 1 February 2016. Vol. 6, no. 2, p. 540. [Accessed 8 July 2019]. DOI 10.1364/OME.6.000540.
161. OGAWA, Shigesaburo and TAKAHASHI, Isao. Glass Transition of Ultrathin Sugar Films Probed by X-Ray Reflectivity. In : CALISKAN, Mahmut (ed.), *Carbohydrate*. IntechOpen, 2017. p. 115–130.
162. GIANNINI, Vincenzo, FERNÁNDEZ-DOMÍNGUEZ, Antonio I., HECK, Susannah C. and MAIER, Stefan A. Plasmonic nanoantennas: Fundamentals and their use in controlling the radiative properties of nanoemitters. *Chemical Reviews*. 2011. Vol. 111, no. 6, p. 3888–3912. DOI 10.1021/cr1002672.
163. SVOBODA, Karel and YASUDA, Ryohei. Principles of Two-Photon Excitation Microscopy and Its Applications to Neuroscience. *Neuron*. 2006. Vol. 50, no. 6, p. 823–839. DOI 10.1016/j.neuron.2006.05.019.
164. SIMSEK, Burcin. *Applications of point process models to imaging and biology*. University of Pittsburgh, 2016.
165. CIELECKI, Paweł Piotr, SOBOLEWSKA, Elżbieta Karolina, KOSTIUOČENKO, Oksana, LEISSNER, Till, TAMULEVIČIUS, Tomas, TAMULEVIČIUS, Sigitas, RUBAHN, Horst Günter, ADAM, Jost and FIUTOWSKI, Jacek. Plasmon–organic fiber interactions in diamond-like carbon coated nanostructured gold films. *Optics Communications*. 2017. Vol. 402, p. 635–640. DOI 10.1016/j.optcom.2017.06.064.
166. FERRARI, Andrea Carlo. Diamond-like carbon for magnetic storage disks. *Surface and Coatings Technology*. 2004. Vol. 180–181, p. 190–206. DOI 10.1016/j.surfcoat.2003.10.146.
167. MEŠKINIS, Šarūnas, ČIEGIS, Arvydas, VASILIAUSKAS, Andrius, ŠLAPIKAS, Kęstutis, TAMULEVIČIUS, Tomas, TAMULEVIČIENĖ, Asta and TAMULEVIČIUS, Sigitas. Optical properties of diamond like carbon films containing copper, grown by high power pulsed magnetron sputtering and direct current magnetron sputtering: Structure and composition effects. *Thin Solid Films*. 2015. Vol. 581, p. 48–53. DOI 10.1016/j.tsf.2014.11.045.
168. GHODSELAHI, T., VESAGHI, M. A. and SHAFIEKHANI, A. Study of surface plasmon resonance of Cu@Cu2O core-shell nanoparticles by Mie theory. *Journal of Physics D: Applied Physics*. 2009. Vol. 42, no. 1, p. 015308. DOI 10.1088/0022-3727/42/1/015308.
169. ZIASHAHABI, A., GHODSELAHI, T. and HEIDARI SAANI, M. Localized Surface Plasmon Resonance properties of copper nano-clusters: A theoretical study of size dependence. *Journal of Physics and Chemistry of Solids*. 2013. Vol. 74, no. 7, p. 929–933. DOI 10.1016/j.jpcs.2013.02.009.
170. KWON, Yong Jung, NA, Han Gil, KANG, Sung Yong, CHOI, Sun Woo, KIM, Sang Sub and KIM, Hyoun Woo. Selective detection of low concentration toluene gas using Pt-decorated carbon nanotubes sensors. *Sensors and Actuators, B: Chemical*. 2016. Vol. 227, p. 157–168. DOI 10.1016/j.snb.2015.12.024.
171. MEŠKINIS, Š., ČIEGIS, A., VASILIAUSKAS, A., TAMULEVIČIENĖ, A., ŠLAPIKAS, K., JUŠKĖNAS, R., NIAURA, G. and TAMULEVIČIUS, S. Plasmonic properties of silver nanoparticles embedded in diamond like

carbon films: Influence of structure and composition. *Applied Surface Science*. October 2014. Vol. 317, p. 1041–1046. DOI 10.1016/j.apsusc.2014.09.032.
172. MEŠKINIS, Šarūnas, VASILIAUSKAS, Andrius, ANDRULEVIČIUS, Mindaugas, JURKEVIČIŪTĖ, Aušrinė, PECKUS, Domantas and TAMULEVIČIUS, Sigitas. Diamond like carbon films with embedded Cu nanoclusters deposited by reactive high power impulse magnetron sputtering: Pulse length effects. *Thin Solid Films*. 2019. Vol. 673, p. 1–6. DOI 10.1016/j.tsf.2019.01.011.
173. THIESSEN, Alyxandra N., HA, Michelle, HOOPER, Riley W., YU, Haoyang, OLIYNYK, Anton O., VEINOT, Jonathan G.C. and MICHAELIS, Vladimir K. Silicon Nanoparticles: Are They Crystalline from the Core to the Surface? *Chemistry of Materials*. 2019. Vol. 31, no. 3, p. 678–688. DOI 10.1021/acs.chemmater.8b03074.
174. BEYENE, Haue Takele, TICHELAAR, Frans D., PEETERS, Paul, KOLEV, Ivan, VAN DE SANDEN, Mauritius C. M. and CREATORE, Mariadriana. Hybrid sputtering-remote PECVD deposition of Au nanoparticles on SiO 2 layers for surface plasmon resonance-based colored coatings. *Plasma Processes and Polymers*. 2010. Vol. 7, no. 8, p. 657–664. DOI 10.1002/ppap.201000003.
175. MIYAZAKI, K., MAEKAWA, N., KOBAYASHI, W., KAKU, M., YASUMARU, N. and KIUCHI, J. Reflectivity in femtosecond-laser-induced structural changes of diamond-like carbon film. *Applied Physics A*. 1 January 2005. Vol. 80, no. 1, p. 17–21. DOI 10.1007/s00339-004-3008-0.
176. ARUTYUNYAN, Natalia R., KOMLENOK, Maxim S., ZAVEDEEV, Evgeny V. and PIMENOV, Sergei M. Raman Spectroscopy of Amorphous Carbon Films Modified by Single-Pulse Irradiation of Nanosecond and Femtosecond Lasers. *Physica Status Solidi B*. January 2018. Vol. 255, no. 1, p. 1700225. DOI 10.1002/pssb.201700225.
177. ZAVEDEEV, E. V., ZILOVA, O. S., BARINOV, A. D., SHUPEGIN, M. L., ARUTYUNYAN, N. R., JAEGGI, B., NEUENSCHWANDER, B. and PIMENOV, S. M. Femtosecond laser microstructuring of diamond-like nanocomposite films. *Diamond and Related Materials*. April 2017. Vol. 74, p. 45–52. DOI 10.1016/j.diamond.2017.02.003.
178. MEŠKINIS, Š., KOPUSTINSKAS, V., ŠLAPIKAS, K., TAMULEVIČIUS, S., GUOBIENĖ, A., GUDAITIS, R. and GRIGALIŪNAS, V. Ion beam synthesis of the diamond like carbon films for nanoimprint lithography applications. *Thin Solid Films*. October 2006. Vol. 515, no. 2, p. 636–639. DOI 10.1016/j.tsf.2005.12.223.
179. HENLEY, S. J., CAREY, J. D. and SILVA, S. R. P. Laser-nanostructured Ag films as substrates for surface-enhanced Raman spectroscopy. *Applied Physics Letters*. 2006. Vol. 88, no. 8, p. 2004–2007. DOI 10.1063/1.2178387.
180. SASINKOVÁ, Vlasta, ARBET, Juraj, BOHÁČEK, Pavol, HURAN, Jozef, KLEINOVÁ, Angela and SEKÁČOVA, Mária. Raman spectroscopy study

of SiC thin films prepared by PECVD for solar cell working in hard environment. *Reliability of Photovoltaic Cells, Modules, Components, and Systems VIII*. 2015. Vol. 9563, p. 95630V. DOI 10.1117/12.2186749.

181. FERRARI, A. C. and ROBERTSON, J. Origin of the 1150 − cm−1 Raman mode in nanocrystalline diamond. *Physical Review B - Condensed Matter and Materials Physics*. 13 March 2001. Vol. 63, no. 12, p. 121405. DOI 10.1103/PhysRevB.63.121405.
182. OSHIRO, Takehiko, YAMAZATO, Masaaki, HIGA, Akira and TOGUCHI, Minoru. Raman analysis of trans-polyacetylene chains in hydrogenated amorphous carbon films. *Japanese Journal of Applied Physics, Part 1: Regular Papers and Short Notes and Review Papers*. 2007. Vol. 46, no. 2, p. 756–760. DOI 10.1143/JJAP.46.756.
183. STRELETSKIY, O. A., ZAVIDOVSKIY, I. A., NISCHAK, O. Yu and PAVLIKOV, A. V. Multiphonon replicas in Raman spectra and conductivity properties of carbon films with different concentrations of sp1-bonds. *Thin Solid Films*. 2019. Vol. 671, p. 31–35. DOI 10.1016/j.tsf.2018.12.025.
184. LUCOTTI, A., CASARI, C. S., TOMMASINI, M., LI BASSI, A., FAZZI, D., RUSSO, V., DEL ZOPPO, M., CASTIGLIONI, C., CATALDO, F., BOTTANI, C. E. and ZERBI, G. sp Carbon chain interaction with silver nanoparticles probed by Surface Enhanced Raman Scattering. *Chemical Physics Letters*. 2009. Vol. 478, no. 1–3, p. 45–50. DOI 10.1016/j.cplett.2009.06.030.
185. KUISMA, M., SAKKO, A., ROSSI, T. P., LARSEN, A. H., ENKOVAARA, J., LEHTOVAARA, L. and RANTALA, T. T. Localized surface plasmon resonance in silver nanoparticles: Atomistic first-principles time-dependent density-functional theory calculations. *Physical Review B - Condensed Matter and Materials Physics*. 2015. Vol. 91, no. 11, p. 115431. DOI 10.1103/PhysRevB.91.115431.
186. KRAVETS, Vira, ALMEMAR, Zamavang, JIANG, Ke, CULHANE, Kyle, MACHADO, Rosa, HAGEN, Guy, KOTKO, Andriy, DMYTRUK, Igor, SPENDIER, Kathrin and PINCHUK, Anatoliy. Imaging of biological cells using luminescent silver nanoparticles. *Nanoscale Research Letters*. 2016. Vol. 11, p. 30. DOI 10.1186/s11671-016-1243-x.
187. HENLEY, S. J., CAREY, J. David and SILVA, S. R. P. Pulsed-laser-induced nanoscale island formation in thin metal-on-oxide films. *Physical Review B - Condensed Matter and Materials Physics*. 2005. Vol. 72, no. 19, p. 1–10. DOI 10.1103/PhysRevB.72.195408.
188. STALMASHONAK, A., PODLIPENSKY, A., SEIFERT, G. and GRAENER, H. Intensity-driven, laser induced transformation of Ag nanospheres to anisotropic shapes. *Applied Physics B: Lasers and Optics*. 2009. Vol. 94, no. 3, p. 459–465. DOI 10.1007/s00340-008-3309-7.
189. STALMASHONAK, Andrei, UNAL, A. Akin, GRAENER, Heinrich and SEIFERT, Gerhard. Effects of Temperature on Laser-Induced Shape Modification of Silver Nanoparticles Embedded in Glass. *Journal of Physical Chemistry C*. 2009. Vol. 113, p. 12028–12032.

190. SCHINKE, Carsten, CHRISTIAN PEEST, P., SCHMIDT, Jan, BRENDEL, Rolf, BOTHE, Karsten, VOGT, Malte R., KRÖGER, Ingo, WINTER, Stefan, SCHIRMACHER, Alfred, LIM, Siew, NGUYEN, Hieu T. and MACDONALD, Daniel. Uncertainty analysis for the coefficient of band-to-band absorption of crystalline silicon. *AIP Advances*. 2015. Vol. 5, no. 6, p. 067168. DOI 10.1063/1.4923379.
191. MALITSON, I. H. Interspecimen Comparison of the Refractive Index of Fused Silica. *Journal of the Optical Society of America*. 1 October 1965. Vol. 55, no. 10, p. 1205–1209. DOI 10.1364/JOSA.55.001205.
192. BYSKOV-NIELSEN, Jeppe, SAVOLAINEN, Juha-Matti, CHRISTENSEN, Martin Snogdahl and BALLING, Peter. Ultra-short pulse laser ablation of metals: threshold fluence, incubation coefficient and ablation rates. *Applied Physics A: Materials Science and Processing*. 2010. Vol. 101, no. 1, p. 97–101. DOI 10.1007/s00339-010-5766-1.
193. LORUSSO, A., NASSISI, V., BUCCOLIERI, A., BUCCOLIERI, G., CASTELLANO, A., LEO, L. S., DI GIULIO, M., TORRISI, L., CARIDI, F. and BORRIELLI, A. Laser ablation threshold of cultural heritage metals. *Radiation Effects and Defects in Solids*. 2008. Vol. 163, no. 4–6, p. 325–329. DOI 10.1080/10420150701777611.
194. DANILOV, P. A., DROZDOVA, E. A., IONIN, A. A., KUDRYASHOV, S. I., ODINOKOV, S. B., RUDENKO, A. A., YUROVSKIKH, V. I. and ZAYARNY, D. A. Single-shot front-side nanoscale femtosecond laser ablation of a thin silver film. *Applied Physics A*. 26 November 2014. Vol. 117, no. 3, p. 981–985. DOI 10.1007/s00339-014-8741-4.
195. DUMITRU, Gabriel, ROMANO, Valerio, WEBER, Heinz P., PIMENOV, Sergei, KONONENKO, Taras, SENTIS, Marc, HERMANN, Jörg and BRUNEAU, Sébastien. Femtosecond laser ablation of diamond-like carbon films. *Applied Surface Science*. January 2004. Vol. 222, no. 1–4, p. 226–233. DOI 10.1016/j.apsusc.2003.08.031.
196. DONG, Y., SAKATA, H. and MOLIAN, P. Femtosecond pulsed laser ablation of diamond-like carbon films on silicon. *Applied Surface Science*. October 2005. Vol. 252, no. 2, p. 352–357. DOI 10.1016/j.apsusc.2005.01.008.
197. GALLAIS, L., BERGERET, E., WANG, B., GUERIN, M. and BÈNEVENT, E. Ultrafast laser ablation of metal films on flexible substrates. *Applied Physics A: Materials Science and Processing*. 2014. Vol. 115, no. 1, p. 177–188. DOI 10.1007/s00339-013-7901-2.
198. STIETZ, F. Laser manipulation of the size and shape of supported nanoparticles. *Applied Physics A: Materials Science and Processing*. 2001. Vol. 72, no. 4, p. 381–394. DOI 10.1007/s003390100757.
199. ZHANG, Weiqiang, LIU, Hongshuang, LU, Jinsheng, NI, Lifa, LIU, Haitao, LI, Qiang, QIU, Min, XU, Bingqian, LEE, Takhee, ZHAO, Zhikai, WANG, Xianghui, WANG, Maoning, WANG, Tao, OFFENHÄUSSER, Andreas, MAYER, Dirk, HWANG, Wang-Taek and XIANG, Dong. Atomic switches of metallic point contacts by plasmonic heating. *Light: Science &*

Applications. 2019. Vol. 8, no. 1, p. 34. DOI 10.1038/s41377-019-0144-z.
200. CHANG, Chao, YANG, Chao, LIU, Yanming, TAO, Peng, SONG, Chengyi, SHANG, Wen, WU, Jianbo and DENG, Tao. Efficient Solar-Thermal Energy Harvest Driven by Interfacial Plasmonic Heating-Assisted Evaporation. *ACS Applied Materials & Interfaces*. 2016. Vol. 8, no. 35, p. 23412–23418. DOI 10.1021/acsami.6b08077.
201. KABALNOV, Alexey. Ostwald ripening and related phenomena. *Journal of Dispersion Science and Technology*. 2001. Vol. 22, no. 1, p. 1–12. DOI 10.1081/DIS-100102675.

ACKNOWLEDGEMENTS

My sincere ‘thank you’ goes to my supervisor Tomas Tamulevičius who was very patient in reading everything I have ever written: from conference abstracts to papers, and, finally, the doctoral dissertation. I wish to express sincere gratitude to Sigitas Tamulevičius who cares a lot about all the students at the Institute of Materials Science of Kaunas University of Technology (KTU MMI) and always presents them with the best opportunities.

I am grateful to Asta Tamulevičienė, Mindaugas Juodėnas, Andrius Vasiliauskas, Šarūnas Meškinis from KTU MMI and Jacek Fiutowski, Vadzim Adashkevich, Arkadiusz Jarosław Goszczak, Horst-Günter Rubahn from Mads Clausen Institute, University of Southern Denmark (SDU MCI) as well as other staff of these institutes for the equipment training, assistance with the experiments and valuable insights.

I am highly thankful to BSc students Gerda Klimaitė, Alvita Žabaitė, and Justas Deveikis for the help with nanoparticle size evaluation and spectroscopic ellipsometry modelling.

I would also like to thank Paweł Piotr Cielecki, Elżbieta Karolina Sobolewska, Michela Diluvio Prete and other students at SDU MCI for making my stay in Denmark during the internship not only entertaining but also super enjoyable.

Lastly, I would like to thank my boyfriend Artur Plotnikov and my whole family for support during all the study years.

CURRICULUM VITAE

First name: AUŠRINĖ
Surname: JURKEVIČIŪTĖ
Date of birth: November 10, 1990
E-mail: ausrine.jurkeviciute@ktu.lt

Education:

- In 2009, completed Secondary Education at Kazlų Rūda Kazys Grinius Gymnasium (diploma with honours).
- 2009-2013, studied Applied Physics at Kaunas University of Technology and in 2013 obtained Bachelor's degree in Physics (diploma with honours).
- 2013-2015, studied Materials Science at Kaunas University of Technology, and in 2015 obtained Master's degree in Materials Technology (diploma with honours).
  - 27/01/2014 – 30/06/2014, ERASMUS studies at University of Southern Denmark, Odense, Denmark.
- 2015-2019, studied Materials Engineering at the Institute of Materials Science of Kaunas University of Technology and was part of the European doctorate programme "Physics and Chemistry of Advanced Materials" (PCAM).
  - 01/03/2017 – 18/06/2017, ERAMUS+ internship at Mads Clausen Institute, University of Southern Denmark, Sønderborg, Denmark.
  - 15/10/2017 – 22/01/2018, ERAMUS+ internship at Mads Clausen Institute, University of Southern Denmark, Sønderborg, Denmark.

Participation in research projects at the Institute of Materials Science of Kaunas University of Technology:

- 30/08/2011 – 31/10/2011, a junior technician, "Micro- and Nanostructures for Solid Oxide Fuel Microcells" (MIKROKOKE-1), No. ATE-05/2010, funded by the Research Council of Lithuania.
- 21/01/2013 – 31/12/2013, a junior laboratory assistant, "Technological Processes of Membranes Production for Micro- Solid Oxide Fuel Cells" (MIKROKOKE-2), No. ATE-09/2012, funded by the Research Council of Lithuania.
- 01/10/2013 – 31/12/2014, a specialist, "Fundamental Investigation of Surface Relief and Molecular Forces Influence on the Self-organization of Nanoparticles and Nanofibers" (PARMO), No. VP1-3.1-ŠMM-10-V-02-028, funded by the European Social Fund Agency.
- 01/07/2013 – 30/04/2015, an engineer, "Regular 3D Structures for Optical Sensors" (3DSens), No. MIP-13147, funded by the Research Council of Lithuania.
- 04/05/2015 – 31/12/2015, a laboratory assistant, "Development of Smart Antibacterial Plaster Employing Nanostructures of Silver and Biopolymers" (NANOSMARTPLASTER), No. PP38/152, funded by Kaunas University of Technology and Lithuanian University of Health Sciences.

- 05/10/2015 – 31/12/2015, a laboratory assistant, “Ultrafast Processes in Organic Semiconductors with Hole-Transporting and Bipolar Properties” (UPOS), No. MTERI-P-15023, funded by Kaunas University of Technology.
- 21/03/2016 – 31/12/2016, a junior researcher, “Investigation of Charge and Energy Transfer Processes in Films of Organic Materials and Their Systems” (KEPOS), No. MTEPI-P-16025, funded by Kaunas University of Technology.
- 11/07/2016 – 31/12/2016, an engineer, “Calibration of 3D Acoustic Microscope Visualization Employing Buried Lithographic Microstructures” (3DSonic), No. PP35/161, funded by Kaunas University of Technology.
- 17/07/2017 – 05/10/2017, a junior researcher, “Creation of Algorithm for Rendering of the Hologram Image and Its Realization in Mobile Devices” (HoloAPP), No. PP29/172, funded by Kaunas University of Technology.
- 01/09/2017 – 13/10/2017, a junior researcher, “Low Secondary Electron Emission Coatings for CERN Super Proton Synchrotron”, No. CERN1/17, funded by the Lithuanian Academy of Sciences.
- 02/10/2017 – 31/12/2019, a junior researcher, “Plasmonic Carbon Nanocomposite Based Self Saturable Absorber Mirrors for Fiber Lasers” (NASAM), No. P-MIP-17-243, funded by the Research Council of Lithuania.
- 01/02/2018 – 31/05/2018, a junior researcher, “The Tests and Development of Smart Collar to Protect Human from the Drowning”, No. 31V-93; 31V-11, funded by the Agency for Science, Innovation and Technology.
- 22/01/2018 – 31/08/2018, a junior researcher, “Heterostructures and Superlattices of the Graphene and Related Carbon 2D Nanomaterials for Photovoltaics” (3D FOTOGRAF), No. 09.3.3-LMT-K-712-01-0183, funded by European Union structural funds.
- 03/09/2018 – 21/12/2018, a junior researcher, “Evaluation of Functional Properties of Coatings used in CERN Accelerators” (DAFUS), No. CERN-KTU-2018-1, funded by the Lithuanian Academy of Sciences.
- 02/09/2019 – 23/12/2019, a junior researcher, “Experimental Characterization of Thin Films and Structures Used in Vacuum Chamber for Particle Accelerators” (DAFU-2), No. CERN-KTU-2019-1, funded by the Lithuanian Academy of Sciences.
- Since 22/01/2018, a junior researcher, “2D Nanostructures of Noble Metal Nanoparticles for Biosensor Applications”, No. P-LLT-18-11, funded by the Research Council of Lithuania.
- Since 11/06/2018, a junior researcher, “Creation and Development of Innovative Optical Security Devices and Next Generation Micro/Nano Devices and Structures for Optical Applications”, No. 01.2.2-CPVA-K-703-02-0014, funded by European Union structural funds.
- Since 01/02/2019, a junior researcher, “Multifunctional Coatings based on ZnO Nanowires for Selective Sensing and Efficient Solar Harvesting” (MultiFun), No. 01.2.2-LMT-K-718-02-0011, funded by European Union structural funds.
- Since 01/02/2019, a junior researcher at KTU MMI.

Participation in the organizing committee of an international scientific event:

The secretary of the organizing committee (2016, 2017, 2018, 2020) and a member of the organizing committee (2012, 2013, 2014, 2015, 2019) of the International Conference-School "Advanced Materials and Technologies" held in Palanga, Lithuanian, end of August.

Internships, trainings, and summer schools abroad:

- 22/11/2014 – 19/12/2014, project internship at Mads Clausen Institute, University of Southern Denmark, Sønderborg, Denmark;
- 05/07/2015 – 11/07/2015, European Summer School at Université de Strasbourg, Strasbourg, France;
- 07/09/2015 – 17/09/2015, the first part of the Intensive Course on Application of Ionizing Radiation in Materials Processing at the Institute of Nuclear Chemistry and Technology, Warsaw, Poland;
- 28/09/2015 – 02/10/2015, the second part of the Intensive Course on Application of Ionizing Radiation in Materials Processing at Università degli studi di Palermo, Palermo, Italy;
- 04/07/2016 – 08/07/2016, PCAM Summer School on Organic Electronics at Université Pierre et Marie Curie, Paris, France;
- 26/06/2017 – 07/07/2017, Lithuanian-French programme "Gilibert" internship at Institut des Matériaux Jean Rouxel, Nantes, France.

Working with scientific equipment experience:

Fabrication of structures by employing holographic and contact lithographies, reactive ion etching technology, optical, scanning electron, helium ion and atomic force microscopies, investigation of hydrophobicity and hydrophilicity of the surface, investigation of optical properties of materials by employing the fibre optic spectrometer and integrating sphere, spectroscopic ellipsometry, Raman spectroscopy.

Awards and scholarships:

- Vydūnas Youth Fund Maecenas Ignas Končius scholarship, 2012;
- KTU rector's scholarship for good results in studies and scientific research: 2011, 2012, 2014, 2015;
- Best poster presentation at the conference "Advanced Materials and Technologies": 2012, 2013, 2016;
- KTU contest of most active PhD students, 2017;
- Best oral presentation at the conference "Mathematics and Natural Sciences: Theory and Applications," 2018;
- Research Council of Lithuania PhD student scholarship for academic achievements: 2017, 2019.

LIST OF PUBLICATIONS AND CONFERENCES RELATED TO THE DISSERTATION

Publications

A1. **JURKEVIČIŪTĖ, Aušrinė**, LAZAUSKAS, Algirdas, TAMULEVIČIUS, Tomas, VASILIAUSKAS, Andrius, PECKUS, Domantas, MEŠKINIS, Šarūnas, TAMULEVIČIUS, Sigitas. Structure and density profile of diamond-like carbon films containing copper: study by X-ray reflectivity, transmission electron microscopy, and spectroscopic ellipsometry. *Thin Solid Films*. 2017. Vol. 630, p. 48-58. DOI: 10.1016/j.tsf.2016.10.015. [IF: 1.939; AIF: 4.131; IF/AIF: 0.469; Q2 (2017)].

A2. **JURKEVIČIŪTĖ, Aušrinė**, ARMAKAVIČIUS, Nerijus, VIRGANAVIČIUS, Dainius, ŠIMATONIS, Linas, TAMULEVIČIUS, Tomas, TAMULEVIČIUS, Sigitas. Fabrication and characterization of one- and two-dimensional regular patterns produced employing multiple exposure holographic lithography. *Journal of optoelectronics and advanced materials*. 2017. Vol. 19, no. 3-4, p. 119-126. [IF: 0.390; AIF: 3.702; IF/AIF: 0.105; Q4 (2017)].

A3. MEŠKINIS, Šarūnas, VASILIAUSKAS, Andrius, ANDRULEVIČIUS, Mindaugas, **JURKEVIČIŪTĖ, Aušrinė**, PECKUS, Domantas, KOPUSTINSKAS, Vitoldas, VISKONTAS, Karolis, TAMULEVIČIUS, Sigitas. Self-saturable absorption and reverse-saturable absorption effects in diamond-like carbon films with embedded copper nanoparticles. *Coatings*. 2019. Vol. 9, no. 2, p. 100. DOI: 10.3390/coatings9020100. [IF: 2.330; AIF: 3.479; IF/AIF: 0.669; Q2 (2018)].

A4. **JURKEVIČIŪTĖ, Aušrinė**, KLIMAITĖ, Gerda, TAMULEVIČIUS, Tomas, FIUTOWSKI, Jacek, RUBAHN, Horst-Günter, TAMULEVIČIUS, Sigitas. Tailoring of silver nanoparticle size distributions in diamond-like carbon nanocomposite thin films by direct femtosecond laser interference patterning. *Advanced Engineering Materials*. 2019. DOI: 10.1002/adem.201900951. [IF: 2.906; AIF: 4.951; IF/AIF: 0.586; Q2 (2018)].

Conference abstracts

Conferences attended by dissertation author

B1. **JURKEVIČIŪTĖ, Aušrinė**, ŽABAITĖ, Alvita, TAMULEVIČIUS, Tomas, TAMULEVIČIUS, Sigitas. Investigation of optical properties of diamond like carbon thin films with embedded silver nanoparticles employing spectroscopic ellipsometry. *8th School on Organic Electronics: Nano-organics and Devices*, 4-8 July 2016, Paris, France. p. 56-57. Poster presentation.

B2. **JURKEVIČIŪTĖ, Aušrinė**, ŽABAITĖ, Alvita, TAMULEVIČIUS, Tomas, TAMULEVIČIUS, Sigitas. Spectroscopic ellipsometry studies of diamond like carbon thin films containing silver nanoparticles. *18th*

international conference-school "Advanced materials and technologies", 27-31 August 2016, Palanga, Lithuania. ISSN 1822-7759, p. 112. Poster presentation, awarded "Young scientist award for the best poster presented".

B3. **JURKEVIČIŪTĖ, Aušrinė**, ŠIMATONIS, Linas, VASILIAUSKAS, Andrius, TAMULEVIČIUS, Tomas, FIUTOWSKI, Jacek, RUBAHN, Horst-Günter. Ablation of amorphous diamond-like carbon nanocomposite films with embedded silver nanoparticles by femtosecond laser interference field = Nanokompozitinių deimanto tipo amorfinės anglies dangų su sidabro nanodalelėmis abliacija femtosekundinio lazerio interferenciniu lauku. *42-oji Lietuvos nacionalinė fizikos konferencija = Lithuanian national physics conference*, 4-6 October 2017, Vilnius, Lithuania. ISBN 9786094598807, p. 187. Poster presentation.

B4. **JURKEVIČIŪTĖ, Aušrinė**, JUODĖNAS, Mindaugas, ADASHKEVICH, Vadzim, VASILIAUSKAS, Andrius, TAMULEVIČIUS, Tomas, FIUTOWSKI, Jacek, TAMULEVIČIUS, Sigitas, RUBAHN, Horst-Günter. Helium ion microscopy of 1D structures ablated employing femtosecond laser interference field. *61st international conference for students of physics and natural sciences "Open readings"*, 20-23 March 2018, Vilnius, Lithuania. p. 233. Poster presentation.

B5. **JURKEVIČIŪTĖ, Aušrinė**, JUODĖNAS, Mindaugas, ADASHKEVICH, Vadzim, VASILIAUSKAS, Andrius, TAMULEVIČIUS, Tomas, FIUTOWSKI, Jacek, TAMULEVIČIUS, Sigitas, RUBAHN, Horst-Günter. Vienmačių periodinių struktūrų nanokompozituose formavimas lazerine interferencine abliacija bei jų vaizdinimas skenuojančiu elektronų ir helio jonų mikroskopais. *XVI studentų konferencija "Matematika ir gamtos mokslai: teorija ir taikymai" = "Mathematics and natural sciences: theory and applications"*, 19 April 2018, Kaunas, Lithuania. ISBN 9786090214534, p. 28-29. Oral presentation, awarded "Best presentation".

B6. KLIMAITĖ, Gerda, **JURKEVIČIŪTĖ, Aušrinė**, FIUTOWSKI, Jacek, RUBAHN, Horst-Günter, TAMULEVIČIUS, Tomas. Analysis of the silver nanoparticle size distribution in nanocomposite thin films upon femtosecond laser irradiation. *20th international conference-school "Advanced materials and technologies"*, 27-31 August 2018, Palanga, Lithuania. ISSN 1822-7759, p. 44. Poster presentation.

B7. **JURKEVICIUTE, Ausrine**, JUODENAS, Mindaugas, ADASHKEVICH, Vadzim, TAMULEVICIUS, Tomas, FIUTOWSKI, Jacek, RUBAHN, Horst-Gunter, TAMULEVICIUS, Sigitas. Direct laser interference patterning of diamond-like carbon silver nanocomposite thin films. *E-MRS Fall Meeting*, 17-20 September 2018, Warsaw, Poland. K.P.6, p. 1. Poster presentation.

B8. DEVEIKIS, Justas, **JURKEVIČIŪTĖ, Aušrinė**, TAMULEVIČIUS, Tomas, TAMULEVIČIUS, Sigitas. Visualisation of femtosecond laser ablated microstructures in DLC:Ag nanocomposite thin films via mapping with spectroscopic ellipsometry. *62nd international conference for students*

of physics and natural sciences "Open readings", 19-22 March 2019, Vilnius, Lithuania. ISBN 9786090701379, p. 207. Poster presentation.

B9. KLIMAITĖ, Gerda, **JURKEVIČIŪTĖ, Aušrinė**, TAMULEVIČIUS, Tomas, TAMULEVIČIUS, Sigitas. Analysis of the changes in average area of silver nanoparticles embedded in diamond-like carbon thin films upon femtosecond laser irradiation. *62nd international conference for students of physics and natural sciences "Open readings"*, 19-22 March 2019, Vilnius, Lithuania. ISBN 9786090701379, p. 300. Poster presentation.

B10. **JURKEVIČIŪTĖ, Aušrinė**, DEVEIKIS, Justas, TAMULEVIČIUS, Tomas, TAMULEVIČIUS, Sigitas. Spectroscopic ellipsometry mapping of femtosecond laser irradiated diamond-like carbon:metal nanocomposite thin films. *8th international conference on spectroscopic ellipsometry*, 26-31 May 2019, Barcelona, Spain, p. 215. Poster presentation.

B11. **JURKEVIČIŪTĖ, Aušrinė**, TAMULEVIČIUS, Tomas, TAMULEVIČIUS, Sigitas. Determination of laser patterning threshold of diamond-like carbon nanocomposite films with embedded silver nanoparticles = Deimanto tipo anglies nanokompozitinių dangų su sidabro nanodalelėmis lazerinio struktūrizavimo slenksčio nustatymas. *43-oji Lietuvos nacionalinė fizikos konferencija = Lithuanian national physics conference*, 3-5 October 2019, Kaunas, Lithuania. ISBN 9786090216385, p. 41. Oral presentation.

Conferences attended by a co-author of the conference presentation

B12. ŽABAITĖ, Alvita, **JURKEVIČIŪTĖ, Aušrinė**, TAMULEVIČIUS, Tomas. Dangų tyrimas spektroskopiniu elipsometru. *XIV studentų konferencija "Matematika ir gamtos mokslai: teorija ir taikymai" = "Mathematics and natural sciences: theory and applications"*, 29 April 2016, Kaunas, Lithuania. ISBN 9786090212257, p. 7-8. Oral presentation by Alvita Žabaitė.

B13. **JURKEVIČIŪTĖ, Aušrinė**, JUODĖNAS, Mindaugas, ADASHKEVICH, Vadzim, TAMULEVIČIUS, Tomas, FIUTOWSKI, Jacek, RUBAHN, Horst-Günter, TAMULEVIČIUS, Sigitas. The effect of silver nanoparticles on the direct laser interference patterning of DLC:Ag nanocomposites. *International conference "Nanotechnology and Innovation in the Baltic Sea region"*, 30 May – 1 June 2018, Sønderborg, Denmark. ISBN 9786090213452, p. 28. Poster presentation by Sigitas Tamulevičius.

B14. KLIMAITĖ, G., **JURKEVIČIŪTĖ, A.**, TAMULEVIČIUS, T., TAMULEVIČIUS, S. Sidabro nanodalelių ant deimantiškosios anglies nanokompozitų analizė naudojant femtosekundinio lazerio spinduliuotę. *XVII studentų konferencija "Matematika ir gamtos mokslai: teorija ir taikymai" = "Mathematics and Natural Sciences: Theory and Applications"*, 4 April, 2019, Kaunas, Lithuania. eISSN 2669-056X, p. 33-34. Oral presentation by Gerda Klimaitė, awarded "Best presentation".

B15. KLIMAITĖ, G., **JURKEVIČIŪTĖ, A.**, TAMULEVIČIUS, T., TAMULEVIČIUS, S. Deimantiškosios anglies nanokompozitų su sidabro

nanodalelėmis lazerinė abliacija femtosekundiniu lazeriu. *Studentų moksliniai tyrimai 2018/2019*, 12 June, 2019, Vilnius, Lithuania. ISBN 9786094820274, p. 24-25. Oral presentation by Gerda Klimaitė.

B16. KLIMAITĖ, Gerda, **JURKEVIČIŪTĖ, Aušrinė**, TAMULEVIČIUS, Tomas, TAMULEVIČIUS, Sigitas. Analysis of the silver nanoparticle size distribution in DLC matrix before and after fs-laser irradiation. *21st international conference-school "Advanced materials and technologies"*, 19-23 August 2019, Palanga, Lithuania. ISSN 1822-7759, p. 51. Poster presentation by Gerda Klimaitė.

LIST OF OTHER PUBLICATIONS AND CONFERENCES NOT RELATED TO THE DISSERTATION

Other publications

1) JUKNIUS, Tadas, RUŽAUSKAS, Modestas, TAMULEVIČIUS, Tomas, ŠIUGŽDINIENĖ, Rita, JUKNIENĖ, Indrė, VASILIAUSKAS, Andrius, **JURKEVIČIŪTĖ, Aušrinė**, TAMULEVIČIUS, Sigitas. Antimicrobial properties of diamond-like carbon/silver nanocomposite thin films deposited on textiles: towards smart bandages. *Materials*. 2016. Vol. 9, no. 5, p. 371. DOI: 10.3390/ma9050371. [IF: 2.654; AIF: 4.328; IF/AIF: 0.613; Q2 (2016)].
2) MEŠKINIS, Š., VASILIAUSKAS, A., ANDRULEVIČIUS, M., **JURKEVIČIŪTĖ, A.**, PECKUS, D., TAMULEVIČIUS, S. Diamond like carbon films with embedded Cu nanoclusters deposited by reactive high power impulse magnetron sputtering: pulse length effects. *Thin solid films*. 2019. Vol. 673, p. 1-6. DOI: 10.1016/j.tsf.2019.01.011. [IF: 1.888; AIF: 4.459; IF/AIF: 0.423; Q2 (2018)].

Other conference abstracts

Other conferences attended by dissertation author

1) **JURKEVIČIŪTĖ, Aušrinė**, ŠIMATONIS, Linas, PRISCHEPA, Sergej L., TAMULEVIČIUS, Tomas. Characterization of femtosecond laser ablated graphene employing Raman spectroscopy and spectroscopic ellipsometry. *19th international conference-school "Advanced Materials and Technologies"*, 27-31 August 2017, Palanga, Lithuania. ISSN 1822-7759, p. 27. Poster presentation.
2) **JURKEVIČIŪTĖ, Aušrinė**, RAJACKAITĖ, Erika, ABAKEVIČIENĖ, Brigita, TAMULEVIČIENĖ, Asta, VASILIAUSKAS, Andrius, MEŠKINIS, Šarūnas, TAMULEVIČIUS, Sigitas. The evaluation of functional properties of amorphous carbon films used in CERN accelerators = CERN greitintuvuose naudojamų amorfinės anglies dangų funkcinių savybių įvertinimas. *43-oji Lietuvos nacionalinė fizikos konferencija = Lithuanian national physics conference*, 3-5 October 2019, Kaunas, Lithuania. ISBN 9786090216385, p. 225. Poster presentation.

Other conferences attended by a co-author of the conference presentation

1) PECKUS, Domantas, TAMULEVIČIUS, Tomas, STANKEVIČIUS, Lukas, **JURKEVIČIŪTĖ, Aušrinė**, RONG, H., HENZIE, J., TAMULEVIČIUS, Sigitas. Ultrafast plasmon relaxation dynamics in Ag and Ag@TiO_2 nanocubes of various dimensions. *18th international conference-school "Advanced Materials and Technologies"*, 27-31 August 2016, Palanga, Lithuania. ISSN 1822-7759, p. 86. Poster presentation by Domantas Peckus.
2) STANKEVIČIUS, Lukas, **JURKEVIČIŪTĖ, Aušrinė**, MEŠKINIS, Šarūnas, TAMULEVIČIUS, Sigitas. Simulation of antireflection multilayered structure based on diamond-like carbon and titanium nitride films for infrared spectrum on metal substrate. *18th international conference-school "Advanced Materials and Technologies"*, 27-31 August 2016, Palanga, Lithuania. ISSN 1822-7759, p. 94. Poster presentation by Lukas Stankevičius.
3) **JURKEVIČIŪTĖ, Aušrinė**, ŠIMATONIS, Linas, PRISCHEPA, Serghej L., TAMULEVIČIUS, Tomas. Investigation of graphene laser ablation parameters employing Raman spectroscopy. *60th international conference for students of physics and natural sciences "Open Readings"*, 14-17 March 2017, Vilnius, Lithuania. ISSN 2029-4425, p. 224. Poster presentation by Linas Šimatonis.
4) PECKUS, Domantas, TAMULEVIČIUS, Tomas, STANKEVIČIUS, Lukas, JUODĖNAS, Mindaugas, **JURKEVIČIŪTĖ, Aušrinė**, RAJACKAITĖ, Erika, GUDAITIS, Rimantas, MEŠKINIS, Šarūnas, ABAKEVIČIENĖ, Brigita, RONG, Hongpan, TAMULEVIČIUS, Sigitas, HENZIE, Joel. Ultrafast dynamics of coherent oscillations of highly monodispersed plasmonic Ag nanocubes and their assemblies. *E-MRS Spring Meeting*, 22-26 May 2017, Strasbourg, France. V.14.57, p. 1. Poster presentation by Domantas Peckus.
5) KLINAVIČIUS, Tomas, ŠIMATONIS, Linas, JUODĖNAS, Mindaugas, **JURKEVIČIŪTĖ, Aušrinė**, PAULAUSKAS, Andrius, JANKAUSKAS, Kęstutis, MASKELIŪNAS, Rytis, OSTREIKA, Armantas, TAMULEVIČIUS, Tomas. Human perception-based rendering algorithm for modelling of dot-matrix hologram images. *International conference "Nanotechnology and innovation in the Baltic Sea region"*, 14-16 June 2017, Kaunas, Lithuania. ISBN 9786090213452, p. 68. Poster presentation by Tomas Klinavičius.
6) KLINAVIČIUS, Tomas, ŠIMATONIS, Linas, JUODĖNAS, Mindaugas, **JURKEVIČIŪTĖ, Aušrinė**, PULAUSKAS, Andrius, JANKAUSKAS, Kęstutis, MASKELIŪNAS, Rytis, OSTREIKA, Armantas, TAMULEVIČIUS, Tomas. Human perception-based rendering of dot-matrix hologram images. *19th international conference-school "Advanced Materials and Technologies"*, 27-31 August 2017, Palanga, Lithuania. ISSN 1822-7759, p. 66. Poster presentation by Tomas Klinavičius.
7) MEŠKINIS, Š., VASILIAUSKAS, A., ŠLAPIKAS, K., TAMULEVIČIUS, T., **JURKEVIČIŪTĖ, A.**, TAMULEVIČIUS, S., VISKONTAS, K.

Diamond like carbon nanocomposite films with embedded copper nanoparticles deposited by magnetron sputtering for saturable absorber. *E-MRS Spring Meeting*, 18-22 June 2018, Strasbourg, France. L.5.6, p. 1. Oral presentation by Šarūnas Meškinis.

8) MEŠKINIS, Šarūnas, ABAKEVIČIENĖ, Brigita, TAMULEVIČIENĖ, Asta, **JURKEVIČIŪTĖ, Aušrinė**, VASILIAUSKAS, Andrius, RAJACKAITĖ, Erika, TAMULEVIČIUS, Sigitas, ZANIN, Danilo Andrea, TABORELLI, Mauro. Low secondary electron yield carbon films for the CERN super proton synchrotron (SPS). *20th international conference-school "Advanced materials and technologies"*, 27-31 August 2018, Palanga, Lithuania. ISSN 1822-7759, p. 143. Poster presentation by Erika Rajackaitė.
9) TAMULEVIČIUS, Sigitas, JUODĖNAS, Mindaugas, **JURKEVIČIŪTĖ, Aušrinė**, TAMULEVIČIUS, Tomas. Technologies for 2-D nanostructures. *International Workshop on Advanced Magnetic Oxides*, 15-17 April 2019, Aveiro, Portugal. p. 30. Oral presentation by Sigitas Tamulevičius.
10) MEŠKINIS, Š., VASILIAUSKAS, A., **JURKEVIČIŪTĖ, A.**, ANDRULEVIČIUS, M., PECKUS, D., TAMULEVIČIUS, S., VISKONTAS, K. Diamond like carbon and diamond like carbon nanocomposite based saturable absorbers. *E-MRS Spring Meeting*, 27-31 May 2019, Nice, France. N.4.6, p. 1. Oral presentation by Šarūnas Meškinis.
11) TAMULEVIČIUS, Tomas, JUODĖNAS, Mindaugas, **JURKEVIČIŪTĖ, Aušrinė**, HENZIE, Joel, FIUTOWSKI, Jacek, TAMULEVIČIUS, Sigitas. Optical properties of silver nanoparticles: tailored self-assembly and nanocomposite thin films. *NanoTech Poland 2019 & Nanotechnology and Innovation in the Baltic Sea Region*, 5-9 June 2019, Poznań, Poland, p. 45. Oral presentation by Tomas Tamulevičius.
12) TAMULEVIČIUS, Tomas, JUODĖNAS, Mindaugas, KLINAVIČIUS, Tomas, TAMULEVIČIENĖ, Asta, **JURKEVIČIŪTĖ, Aušrinė**, TAMULEVIČIUS, Sigitas. Laser imposed micro and nano patterns: from nanoparticles and hydrophobic surfaces to anti-counterfeiting applications. *International conference "Nanomaterials for Biosensor and Biomedical Applications"*, 2-4 July 2019, Jurmala, Latvia, p. 42. Oral presentation by Tomas Tamulevičius.
13) MALINOVSKIS, Uldis, POPLAUSKS, Raimonds, **JURKEVIČIŪTĖ, Aušrinė**, PRIKULIS, Juris, ERTS, Donats. Production of high-density Au nanoparticle arrays on nanoporous anodic alumina from colloidal solutions. *21st international conference-school "Advanced Materials and Technologies"*, 19-23 August 2019, Palanga, Lithuania. ISSN 1822-7759, p. 56. Poster presentation by Uldis Malinovskis.

SL344. 2020-03-19, 17,25 leidyb. apsk. l. Tiražas 12 egz.
Išleido Kauno technologijos universitetas, K. Donelaičio g. 73, 44249 Kaunas
Spausdino leidyklos „Technologija“ spaustuvė, Studentų g. 54, 51424 Kaunas